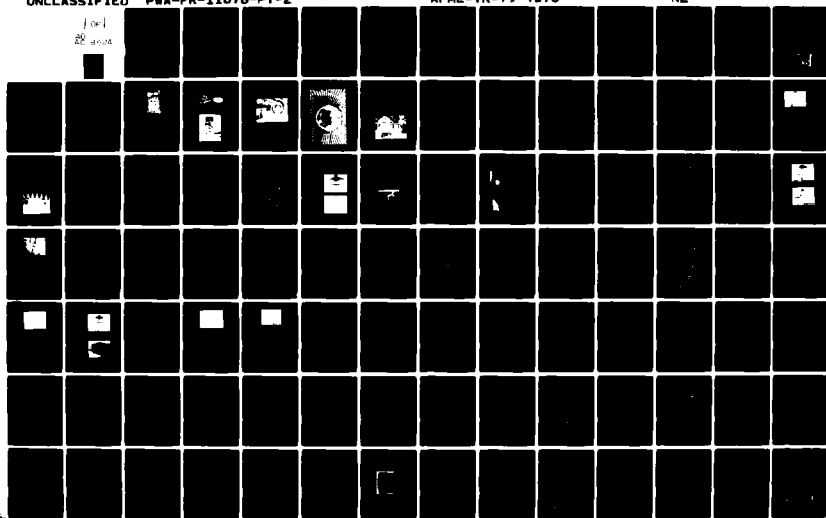


AD-A089 524

PRATT AND WHITNEY AIRCRAFT GROUP WEST PALM BEACH FL 6--ETC F/G 21/5
DISK RESIDUAL LIFE STUDIES. PART 2. TF30 10TH-STAGE COMPRESSOR --ETC(U)
DEC 79 J S CARGILL, J K MALPANI, Y W CHENG F33615-76-C-5172
UNCLASSIFIED PWA-FR-11878-PT-2 AFML-TR-79-4173 NL

1 of 1
28 pages



AFML-TR-79-4173

LEVEL II

(2)
3.5

DISK RESIDUAL LIFE STUDIES

AD A089524

PART 2: TF30 10TH-STAGE COMPRESSOR DISK (INCOLOY 901)

J. S. Cargill, J. K. Malpani, Y. W. Cheng

Pratt & Whitney Aircraft Group
Government Products Division
West Palm Beach, Florida 33402

December 1979

Technical Report AFML-TR-79-4173, Part 2
Final Report for Period 1 April 1976 through 30 June 1979

DTIC
ELECTE
S SEP 25 1980
A

Approved for public release; distribution unlimited

Prepared for
AIR FORCE MATERIALS LABORATORY
AIR FORCE WRIGHT AERONAUTICAL LABORATORIES
AIR FORCE SYSTEMS COMMAND
WRIGHT-PATTERSON AIR FORCE BASE, OHIO

DDC FILE COPY

80 9 25 027

NOTICE

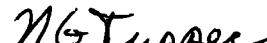
When Government drawings, specifications, or other data are used for any purpose other than in connection with a definitely related Government procurement operation, the United States Government thereby incurs no responsibility nor any obligation whatsoever; and the fact that the government may have formulated, furnished, or in any way supplied the said drawings, specifications, or other data, is not to be regarded by implication or otherwise as in any manner licensing the holder or any other person or corporation, or conveying any rights or permission to manufacture, use, or sell any patented invention that may in any way be related thereto.

This report has been reviewed by the Information Office (OI) and is releasable to the National Technical Information Service (NTIS). At NTIS, it will be available to the general public, including foreign nations.

This technical report has been reviewed and is approved for publication.



DR. W. REIMANN
Metals Behavior Branch
Metals and Ceramics Division



NATHAN G. TUPPER, Chief
Metals Behavior Branch
Metals and Ceramics Division

If your address has changed, if you wish to be removed from our mailing list, or if the addressee is no longer employed by your organization please notify AFWAL/MLLN, W-PAFB, OH 45433 to help us maintain a current mailing list.

Copies of this report should not be returned unless return is required by security considerations, contractual obligations, or notice on a specific document.

UNCLASSIFIED

SECURITY CLASSIFICATION OF THIS PAGE (When Data Entered)

19 REPORT DOCUMENTATION PAGE		READ INSTRUCTIONS BEFORE COMPLETING FORM	
1. REPORT NUMBER AFMLTR-79-4173 ✓	2. GOVT ACCESSION NO. AD-A089524	3. RECIPIENT'S CATALOG NUMBER	
4. TITLE (and Subtitle) <u>DISK RESIDUAL LIFE STUDIES</u> <u>Part 2: TF30 10th Stage Compressor Disk (INCOLOY 901)</u>		5. TYPE OF REPORT & PERIOD COVERED Final Report 1 Apr 1976-30 June 1979	
7. AUTHOR(s) J. S. Cargill, J. K. Malpani, Y. W. Cheng		6. PERFORMING ORG. REPORT NUMBER PW A-FR-11878 - PT-2	
9. PERFORMING ORGANIZATION NAME AND ADDRESS Pratt & Whitney Aircraft Group Government Products Division West Palm Beach, FL. 33402		10. PROGRAM ELEMENT, PROJECT, TASK AREA & WORK UNIT NUMBERS 7351 06 C1 11 L-19	
11. CONTROLLING OFFICE NAME AND ADDRESS Air Force Materials Laboratory (LLN) Air Force Wright Aeronautical Laboratories, AFSC Wright-Patterson AFB, OH		12. REPORT DATE December 1979	
14. MONITORING AGENCY NAME & ADDRESS (if different from Controlling Office)		13. NUMBER OF PAGES 90	
		15. SECURITY CLASS. (of this report) Unclassified	
		15a. DECLASSIFICATION/DOWNGRADING SCHEDULE	
16. DISTRIBUTION STATEMENT (of this Report) Approved for public release; distribution unlimited.			
17. DISTRIBUTION STATEMENT (of the abstract entered in Block 20, if different from Report)			
18. SUPPLEMENTARY NOTES			
19. KEY WORDS (Continue on reverse side if necessary and identify by block number) Turbine engine disks Eddy current Nondestructive evaluation Fluorescent penetrant Fracture mechanics Acoustic emission			
20. ABSTRACT (Continue on reverse side if necessary and identify by block number) A residual fatigue life prediction method, suitable for Retirement-for-Cause application, has been developed for two P&WA turbine disks: the F100 1st-stage high pressure turbine disk and the TF30 10th-stage compressor disk. The method is based upon interaction of fracture mechanics crack propagation modeling concepts with laboratory nondestructive evaluation (NDE) techniques. Fracture mechanics life models were developed using the GPD hyperbolic sine (SINH) model refined during an earlier Air Force Materials Laboratory (AFML) program. Stress intensity (K) solutions for the engine components were based upon experimental effective K determinations made during full-scale component fatigue tests. The NDE techniques developed for disk inspections included acoustic emission (AE), eddy current (EC), and fluorescent penetrants (FP). Stress-enhanced penetrant and semi-automated rotating probe EC techniques were developed as periodic inspections, while the AE time-domain technique was developed as a real-time inspection tool.			

DD FORM 1 JAN 73 1473

EDITION OF 1 NOV 65 IS OBSOLETE

UNCLASSIFIED

SECURITY CLASSIFICATION OF THIS PAGE (When Data Entered)

FOREWORD

This is the final report for Contract F33615-76-C-5172, Disk Residual Life Studies, covering the period 1 April 1976 to 30 June 1979. It is divided into two parts relating to specific engine disk applications. Part 1 deals with F100 1st-stage turbine disk, while the subject of Part 2 is the TF30 10th-stage compressor disk. A third part is scheduled to be published in 1980 as the final report for an additional study entitled, "Concept Definition: Retirement-for-Cause of F100 Rotor Disks." The first two parts are being submitted in December 1979.

The Air Force Project Engineer is Dr. W. H. Reimann, AFML/LLN, Wright-Patterson AFB, Ohio. The Responsible Engineer/Program Manager is J. S. Cargill, reporting through J. A. Harris, Jr. to M. C. VanWanderham, General Supervisor, Mechanics of Materials and Structures, Pratt & Whitney Aircraft Group/Government Products Division, (P&WA/GPD) West Palm Beach, Florida 33402.

The authors wish to acknowledge the contributions to this program made by R. M. Wallace, former Program Manager, prior to his reassignment to his present position at the P&WA Dayton field office.

Accession For	
NTIS GRA&I	<input checked="checked" type="checkbox"/>
DDC TAB	<input type="checkbox"/>
Unannounced	<input type="checkbox"/>
Justification	
By	
Distribution/	
Availability Codes	
111	Available/or special

CONTENTS

<i>Section</i>	<i>Page</i>
I INTRODUCTION	1
II EXPERIMENTAL METHODS	3
A. Laboratory Apparatus	3
B. Test Procedures	11
C. Acoustic Emission Inspection Procedures	15
D. Eddy Current Inspection Procedures	18
E. Fluorescent Penetrant Inspection Procedures	19
III TEST RESULTS	23
A. Strain-Controlled LCF	23
B. Bolthole Simulation LCF	27
C. Fracture Mechanics (Fatigue Crack Propagation)	34
D. Compressor Disk Testing	36
E. Compressor Disk Life Analysis	58
IV DISCUSSION	65
A. Strain-Controlled LCF	66
B. Bolthole Simulation LCF	66
C. Fracture Mechanics Testing	67
D. Compressor Disk Testing	67
V CONCLUSIONS	71
APPENDIX A — Acoustic Emission Analysis	73
APPENDIX B — Statistical Treatment of Inspection Reliability	86
REFERENCES	90

ILLUSTRATIONS

<i>Figure</i>		<i>Page</i>
1	Constant Strain LCF Specimen	3
2	Bolthole LCF Specimen FML 96308A	4
3	Servohydraulic Closed-Loop, Low-Cycle Fatigue Test Machine Controlled by Command Typically from a Digital-to-Analog Functional Generator	4
4	Surface Flaw Fatigue Propagation Specimen	5
5	AE System Configuration for LCF Characterization of Incoloy 901 (PWA 1003)	6
6	Time Domain Acoustic Emission Analysis and Linear Source Location Performed by the Dunegan/Endevco Model 920 Distribution Analyzer	7
7	Gulton FD100, Semiautomatic Eddy Current Bolthole Inspection System	8
8	Circograph 6.230 Eddy Current Inspection Equipment	8
9	GDP "Ferris Wheel" Fatigue Test Facility	9
10	TF30 10th-Stage Compressor Disk (Bore-Modified) Installed in the "Ferris Wheel"	10
11	GPD Computerized Acoustic Emission Real Time Inspection System	11
12	Dunegan/Endevco Model 1032 System Schematic	12
13	Dunegan/Endevco Model 1032 Computerized AE System Transducer Arrays	13
14	Incoloy 901 Bolthole LCF Specimen Room Temperature Strain Survey	14
15	Hyperbolic Sine on Cartesian Coordinates	14
16	Crack Propagation Influenced by Frequency (a), Stress (b), and Temperature (c)	16
17	Classical Representation of an AE Event	17
18	Distribution Analyzer Histogram, Normal Output	18
19	TF30 10th-Stage Compressor Disk S/N G82568: Fluorescent Penetrant Indications at Boltholes. Fatigue Cracks Produced by Ferris Wheel Cycling at 400°F, 3 cpm, R = 0.07, $\Delta\epsilon_{max} = 0.85\%$	19
20	TF30-P-412 Strain Control Simulation of 10th-Stage Compressor Disk LCF Test Duty Cycle Definition, Temperature 400°F	23
21	Acoustic Emission Rate Analysis: Strain Controlled LCF Testing of Incoloy 901	24
22	Acoustic Emission Multiparameter Distribution Analysis: Strain Controlled LCF Testing of Incoloy 901	25
23	Acoustic Emission Time Domain Analysis: Applied to Fatigue Initiation Classification of Incoloy 901	26
24	Fatigue Crack Documentation (Replicas) from Bolthole LCF Specimen	28
25	Frequency Response of Microminiature Acoustic Emission Transducer (D/E Model S9222)	29
26a	Acoustic Emission Rate Comparison: Bolthole LCF Test, D750 Sensor (Standard) vs S9222 Sensor (Micro) (Sheet 1 of 3)	30
26b	Acoustic Emission Rate Comparison: Bolthole LCF Test, D750 Sensor (Standard) vs S9222 Sensor (Micro) (Sheet 2 of 3)	31
26c	Acoustic Emission Rate Comparison: Bolthole LCF Test, D750 Sensor (Standard) vs S9222 Sensor (Micro) (Sheet 3 of 3)	32
27	Evaluation of Microminiature AE Sensor Peak Amplitude Distribution Histograms Before Crack Indications and During Crack Indications	33
28	Fatigue Crack (0.014 in. length) Indicated by Microminiature Acoustic Emission Sensor	34
29	Overload Test Profile for Crack Growth Specimen S/N 1572	35
30	Crack Growth Relationship (da/dN vs ΔK) for Incoloy 901 S/N 1189	37
31	Crack Growth Relationship (da/dN vs ΔK) for Incoloy 901 S/N 1408	38

ILLUSTRATIONS (Continued)

Figure		Page
32	Crack Growth Relationship (da/dN vs ΔK) for Incoloy 901 S/N 1413	39
33	Crack Growth Relationship (da/dN vs ΔK) for Incoloy 901 S/N 1188	40
34	Crack Growth Relationship (da/dN vs ΔK) for Incoloy 901 S/N 1434	41
35	Crack Growth Relationship (da/dN vs ΔK) for Incoloy 901 S/N 1572	42
36	TF30 10th-Stage Compressor Disk Ferris Wheel Duty Cycle Simulation	43
37	Stress Distribution of TF30 10th-Stage Compressor Disk Bolthole (Inboard, rear) at Maximum Load (4250 lb)	45
38	Crack Length vs Fatigue Cycles: Ferris Wheel Simple Sawtooth Cycle Testing	46
39	Crack Depth vs Fatigue Cycles: Ferris Wheel Mission Cycle Testing	46
40	10th-Stage Compressor Disk Replica Measurements vs Heat Tint	47
41	Compressor Disk Calibration for Computerized Acoustic Emission Inspection ...	48
42	Ferris Wheel Test of TF30 10th-Stage Compressor Disk: Cyclic Load and Acoustic Emission Signal Level	49
43	AE Source Location Record for Compressor Disk S/N G82568, Test Cycles 1923-2123	51
44	Post-Test Analysis of AE Events vs Cyclic Load	52
45	Schematic — Lower Bound Probability of Detection vs Crack Length (Plotted by Equal-Flaw-Size-Interval Method)	56
46	Schematic of POD Curve Based on an Analytical Expression of the Form $y = a(x)^b$	57
47	K_{max} vs a for Compressor Disk Boltholes	59
48	Bolthole Crack Depth vs Cycles: Life Analysis of Simple Sawtooth Cycle, Effective K Approach	60
49	Bolthole Crack Depth vs Cycles: Life Analysis of Simple Sawtooth Cycle, Bowie Analysis	61
50	Bolthole Crack Depth vs Cycles: Life Analysis of Simple Sawtooth Cycle, Deep Through-Thickness Crack Approach	61
51	Bolthole Crack Depth vs Missions: Life Analysis of Duty Cycle, Experimental Effective K Approach with Non-Synergistic Effects	62
52	Bolthole Crack Depth vs Missions: Life Analysis of Duty Cycle, Experimental Effective K Approach Accounting for Synergistic Effects ...	63
53	Bolthole Crack Depth vs Missions: Life Analysis of Duty Cycle, Bowie Solution Accounting for Synergistic Effects	63
54	Bolthole Crack Depth vs Missions: Life Analysis of Duty Cycle, Deep Through-Thickness Crack Approach Accounting for Synergistic Effects	64
55	Estimation of Average Disk Bolthole Propagation Life, as Determined from Simple Cycle Ferris Wheel Testing	65
56	Initiation Life Comparison: Compressor Disks vs Incoloy 901 Strain Controlled LCF	67
A1	A Simple Picture of an Acoustic Emission Event	73
A2	Test No. 00265: Cumulative Emissions and Emission Rate vs Cycles	75
A3	Schematic Representation of Components in Energy Measuring Device	77
A4	Log Amplification Characteristics of Dunegan/Endevco 920/921 Amplitude Distribution Analyzer	79
A5	Burst Time Pulse Width Composed of Signal Pulse Width Plus Envelope Time (Manually Selected as 50 μ sec, 100 μ sec, 1 msec, or 10 msec)	80

ILLUSTRATIONS (Continued)

<i>Figure</i>		<i>Page</i>
A6	Acoustic Emission Configuration to Monitor Strain Control Tests. Phase I: Acoustic Emission Characterization of Fatigue Damage	81
A7	Typical Frequency Response of a Dunegan/Endevco Model D750 Transducer	83
A8	Distribution Analyzer Output Example	84
B1	Typical Effect of Crack Length on the Probability of Detection by Nondestructive Inspection	87

TABLES

<i>Table</i>	<i>Page</i>
1 Static FPI Procedure for TF30 10th Compressor Boltholes	20
2 Wink Fluorescent Penetrant Inspection Procedure (TF30 10th Compressor Disk Boltholes)	21
3 Strain-Controlled LCF Testing of Incoloy 901 at 400°F for Compressor Disk Simulation	23
4 Incoloy 901 LCF Bolthole Testing	27
5 Incoloy 901 Fracture Mechanics Testing	34
6 Summary of Disk LCF Lives	47
7 Compressor Disk S/N G82568 Replication Results after 1923-Cycle Inspection ...	51
8 Reliability of Stress-Enhanced FPI for Inspection of TF30 10th-Stage Compressor Disk Boltholes	53
9 Reliability of Eddy Current for Inspection of TF30 10th-Stage Compressor Disk Boltholes	53
10 Reliability of Laboratory Static FPI for Inspection of TF30 10th-Stage Compressor Disk Boltholes	54
11 Reliability of Production-Type FPI for Inspection of TF30 10th-Stage Compressor Disk Boltholes	54
12 Summary of NDT Reliability for TF30 10th-Stage Compressor Disk Bolthole Inspection	55

SECTION I INTRODUCTION

Application of the disk residual life prediction methodology to the TF30 10th-stage compressor disk was performed in conjunction with the Navy's M-32 component life verification program. The objective of this task was to extend the residual life prediction philosophy developed for the F100 1st-stage turbine disk to another application involving a different disk critical location and a non-powder metallurgy disk alloy. While extension of the fracture mechanics/nondestructive evaluation (NDE) modeling concept to the compressor disk is not meant to prove universal applicability of the concept, it has shown (1) the versatility of the GPD hyperbolic sine data modeling capability, (2) the utility of a relatively simple experimental method of determining stress intensity, and (3) the sensitivity and reliability capabilities of properly applied laboratory NDE.

The Navy M-32 program provided funding for the compressor disk mechanical testing effort. Six disks were subjected to engine-simulated fatigue damage in the Materials and Mechanics Technology (MMT) ferris wheel fixture, and residual life models were developed by MMT as periodic inspections were performed. GPD-Design is developing detailed fatigue models for this disk (under M-32 funding), but results are not yet available for comparison with MMT models.

The TF30 10th-stage compressor disk study is being discussed as Part 2 of this final report to avoid confusion between this study and the F100 1st-stage turbine disk program. Basic materials studies, studies with complex geometry specimens, and fracture mechanics residual life models were developed for the compressor disk, as were developed for the F100 disks. The primary differences in conduction of the TF30 compressor disk program from the F100 turbine disk program are: (1) NDE reliability of periodic inspections was quantified for compressor disk laboratory inspections, and (2) fracture mechanics models were developed based upon simple cyclic testing of three compressor disks and fracture mechanics specimens, and projected to predict behavior of three additional disks tested to a duty-cycle simulation.

SECTION II TF30 10th-STAGE COMPRESSOR DISK EXPERIMENTAL METHODS

LABORATORY APPARATUS

A short materials characterization task was conducted for Incoloy 901 nickel alloy, which is used to fabricate the TF30 10th-stage compressor disk. Material characterization was necessary to delineate acoustic emission (AE) output during fatigue and to produce bolthole fatigue crack reference masters for EC and fluorescent penetrant (FP) inspections. Strain-controlled low cycle fatigue (LCF) testing was conducted using the specimen configuration shown in Figure 1. The calibrated hourglass-shaped gage section made metallurgical examinations of fatigue mechanisms relatively simple. Figure 2 illustrates the configuration of the bolthole-simulation LCF specimens. The bolthole LCF specimen design was used during complex geometry specimen tests to determine material fatigue and associated AE characteristics, as well as to provide a test bed and control sample for assessment of periodic inspection techniques (EC and FP).

Specimen fatigue testing was conducted using servo-controlled hydraulic test machines. The machine, illustrated in Figure 3, was designed and built by GPD to provide efficient stress, strain and temperature simulations of typical engine LCF environments.

Crack propagation testing of Incoloy 901 was performed on the center notch specimen configuration shown in Figure 4. Simple cyclic and overload tests were conducted in support of fracture mechanics disk life predictions and to determine the da/dN vs AE rate characteristics of the material. A 6-in. waveguide was fixed to the specimens (tapped hole) and used to transfer AE signals to a room-temperature piezoelectric transducer.

The AE apparatus used in the development of material characterizations was developed by Dunegan/Endevco of San Juan Capistrano, Ca. Figure 5 schematically presents the AE system monitoring configuration. Performance of three simultaneous time-domain distribution analyses (amplitude, pulse width and ringdown counts) was performed through the combination of two external memory modules with a single distribution analyzer. This approach proves more desirable than the use of three separate distribution analyzers (the configuration used for the F100 turbine disk study) because the external memories are less expensive and require less bin space in the Dunegan power supply. Figure 6 shows the Dunegan/Endevco Model 920 Distribution Analyzer. Appendix A explains the operation of the analyzer and other system components.

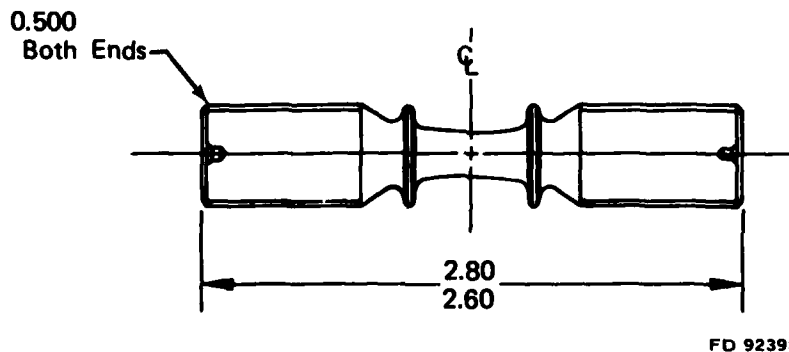
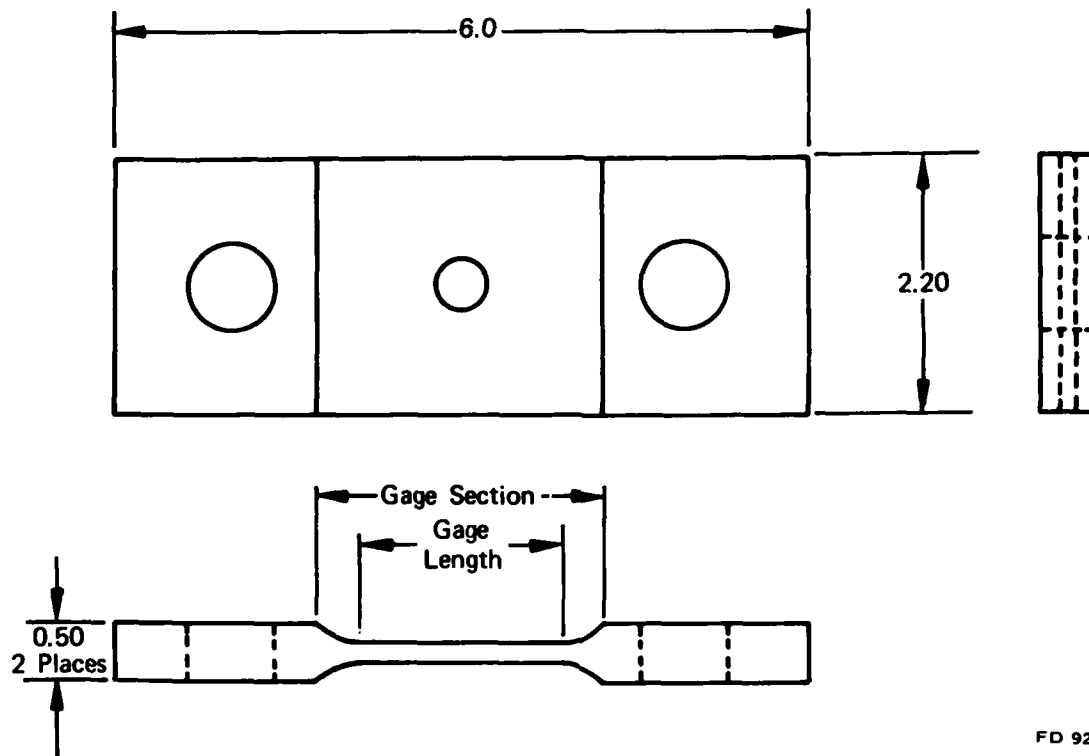
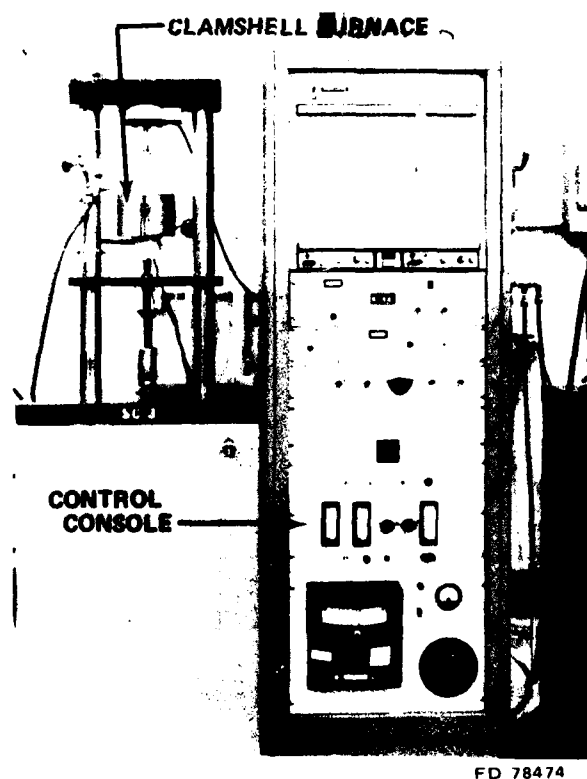


Figure 1. Constant Strain LCF Specimen



FD 92414

Figure 2. Bolthole LCF Specimen FML 96308A



FD 78474

Figure 3. Servohydraulic Closed-Loop, Low-Cycle Fatigue Test Machine Controlled by Command Typically from a Digital-to-Analog Functional Generator

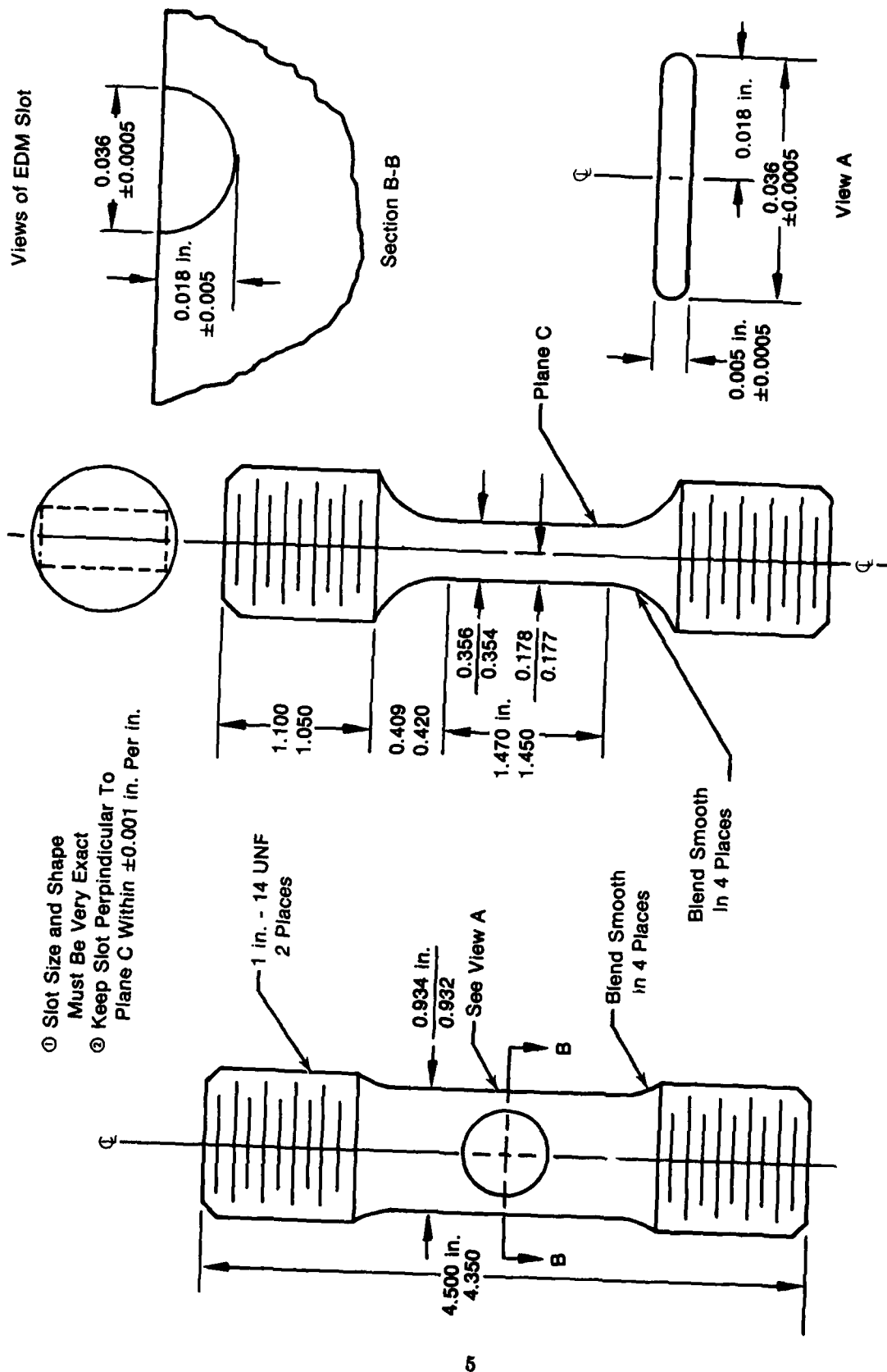
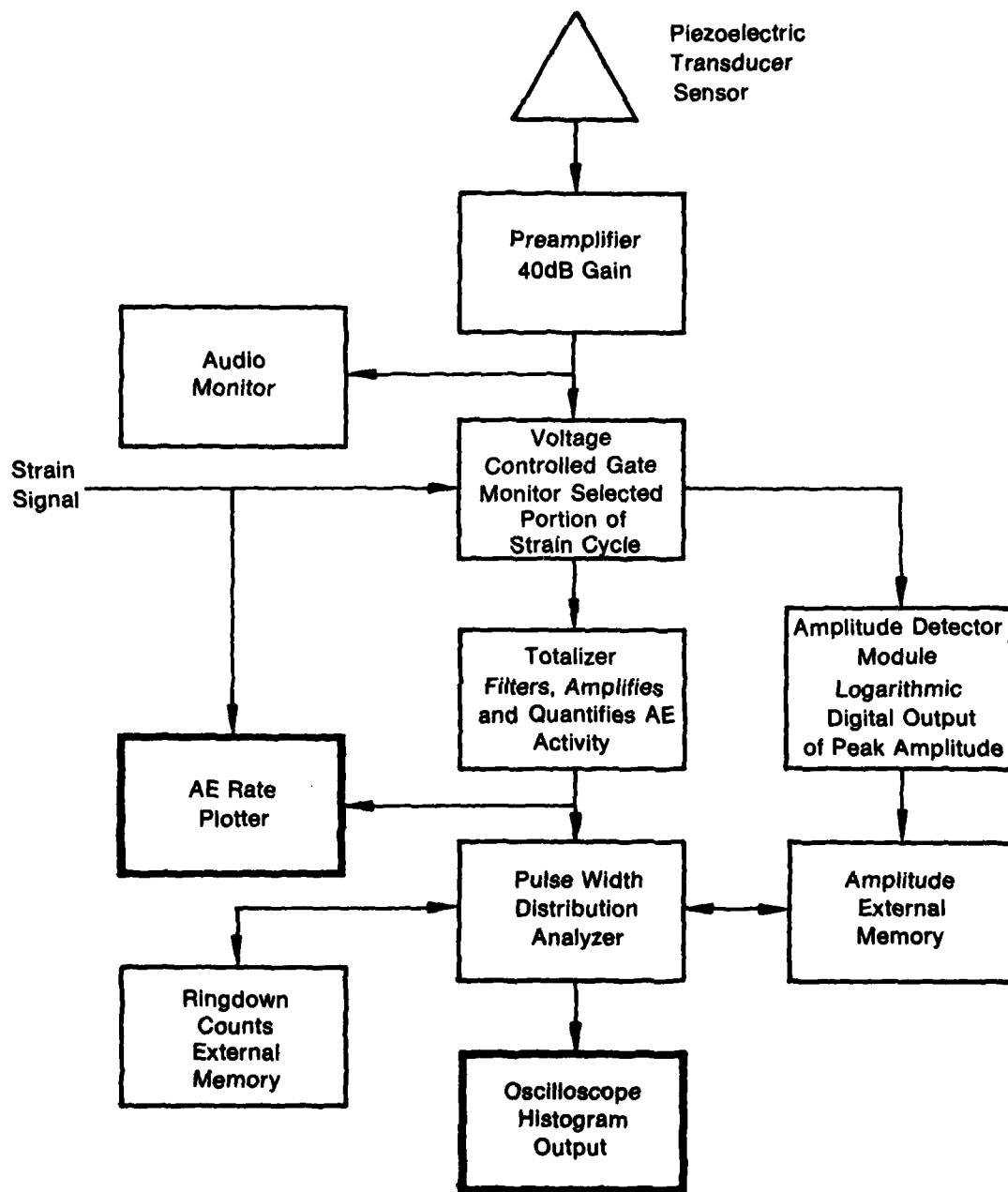
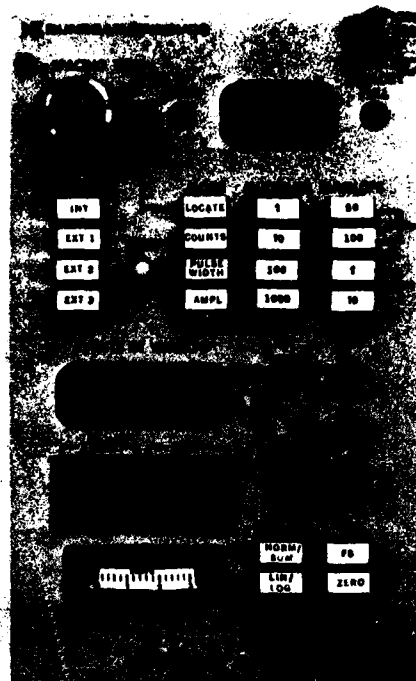


Figure 4. Surface Flow Fatigue Propagation Specimen



FD 175106

Figure 5. AE System Configuration for LCF Characterization of Incoloy 901 (PWA 1003)



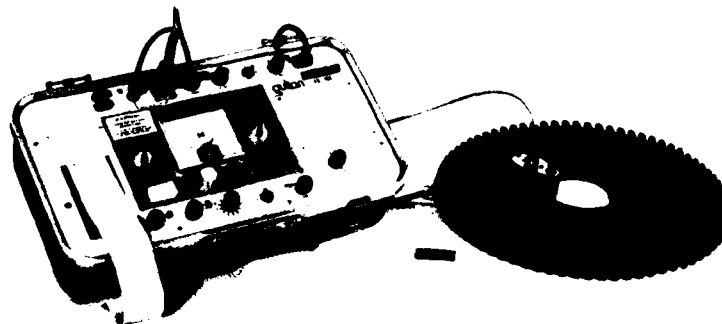
FAE 158641

Figure 6. Time Domain Acoustic Emission Analysis and Linear Source Location Performed by the Dunegan/Endevco Model 920 Distribution Analyzer

The AE sensors used during this program were Dunegan/Endevco Model D750. The piezoelectric transducers were of differential design, resonant near 700 kHz. Peak sensitivity is approximately -75 dB (referenced to 1 volt/microbar). Figure A7 in Appendix A shows a typical frequency response curve.

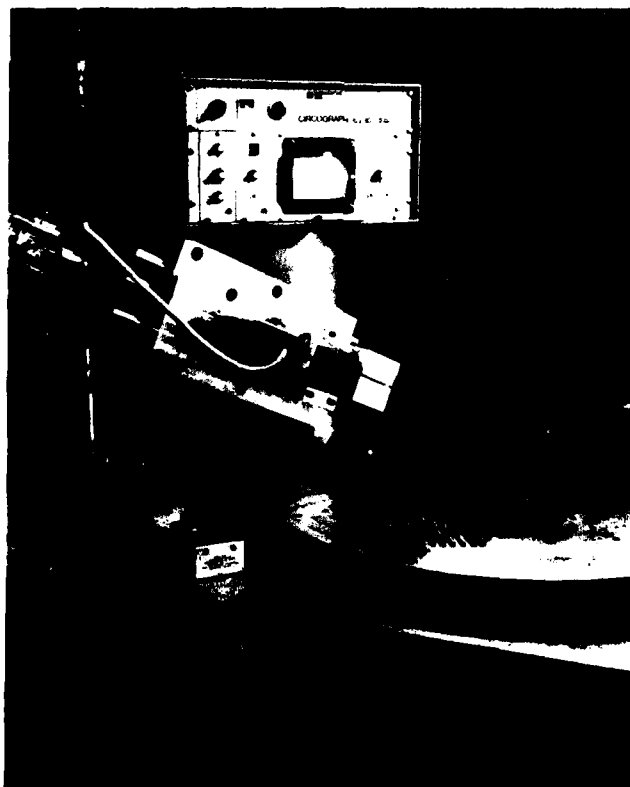
The EC inspections of LCF bolthole specimens were performed using a Gulton FD100 semi-automatic rotating probe instrument, as shown in Figure 7. This system has been used by the Air Force for field inspections for several years and has been proven to be a sensitive, reliable tool for detection of surface fatigue damage. However, inspections of the TF30 10th-stage compressor disks, which were used to determine NDE reliability figures, were conducted using a Dr. Forster Circograph Model 6.230, as shown in Figure 8. These inspections were performed by GPD-Nondestructive Test Engineering using a tight-fitting, oversized probe to obtain maximum sensitivity from the bolthole inspections.

Engine-simulated Type I LCF cycles were applied to each of the six compressor disks by the GPD ferris wheel fixture shown in Figure 9. Radial loads applied by means of pressurized hydraulic cylinders operating from a manifold and connected to drawbars simulate the blade/disk attachment configuration. Loads may be applied in a steady-state condition, cyclic loading, cyclic load plus dwell, or engine mission simulation. Each compressor disk was bore-modified, as shown in Figure 10, to produce a proper engine-simulating strain distribution in the vicinity of the boltholes (primary critical location). The elevated test temperatures (400°F) was achieved in the ferris wheel using resistance-heating ovens which sandwiched the test disk faces.



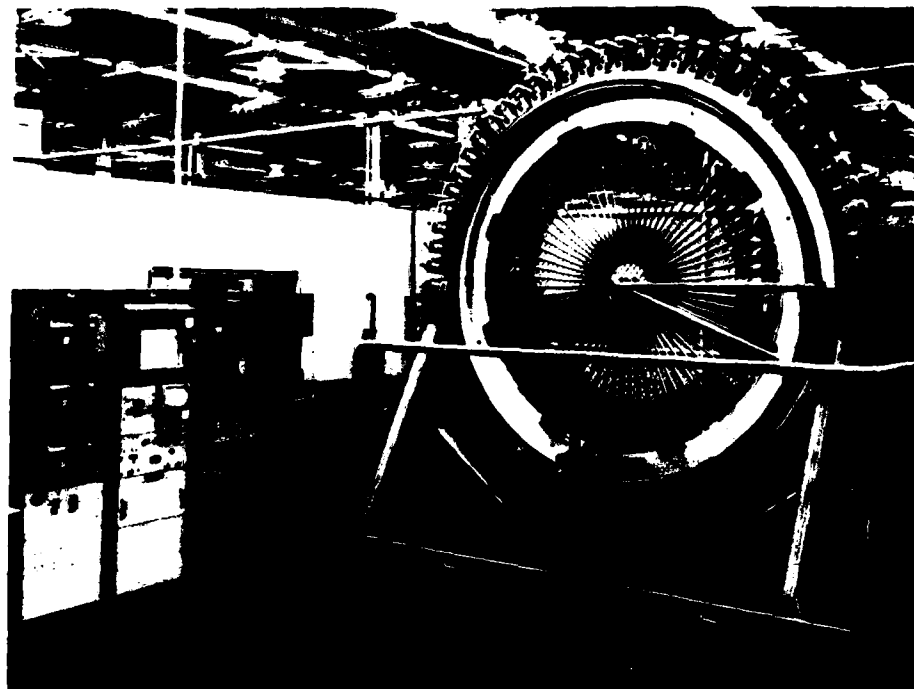
FAE 175754

Figure 7. Gulton FD100, Semiautomatic Eddy Current Bolthole Inspection System



FAE 36016

Figure 8. Circograph 6.230 Eddy Current Inspection Equipment



FD 112843

Figure 9. GDP "Ferris Wheel" Fatigue Test Facility

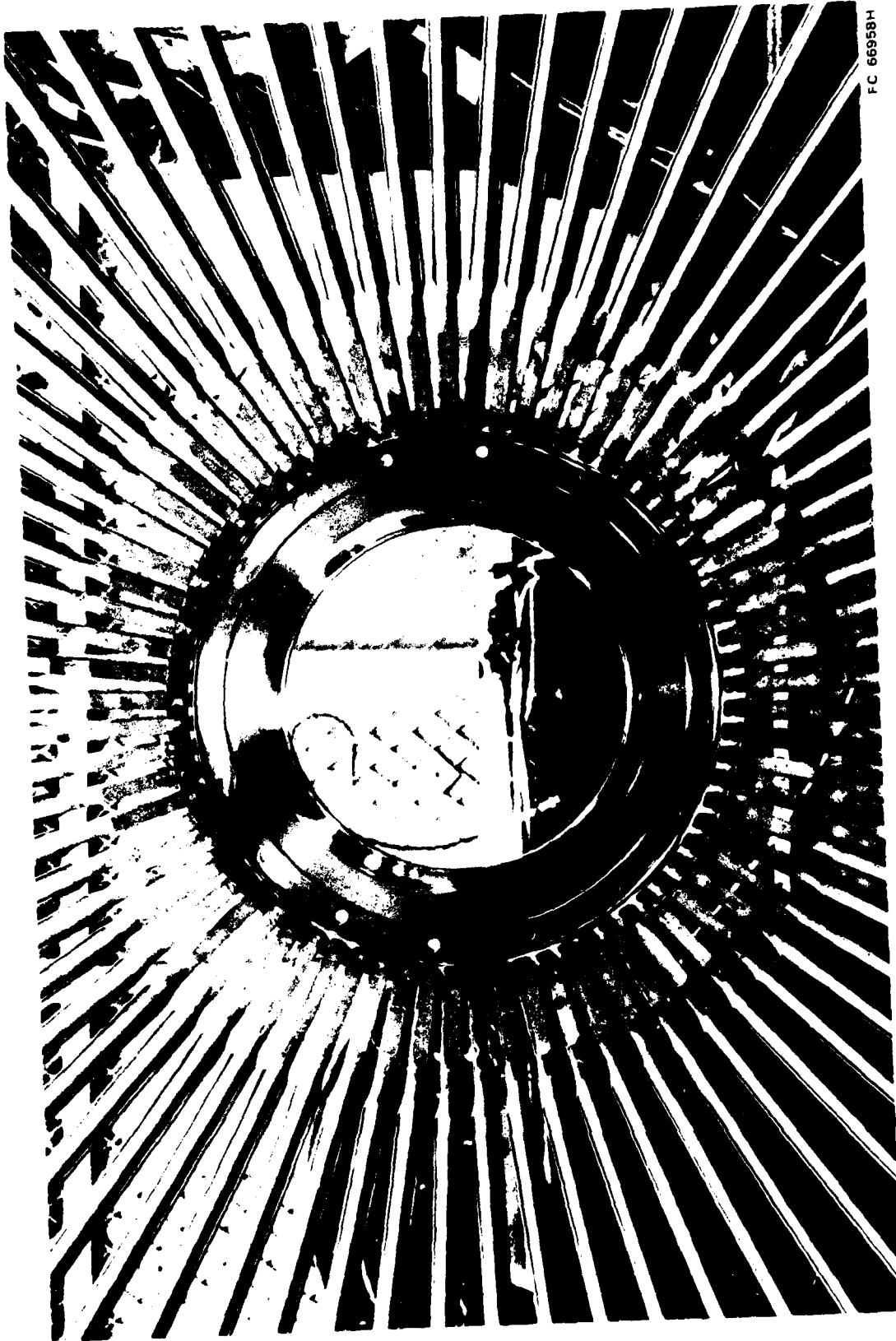


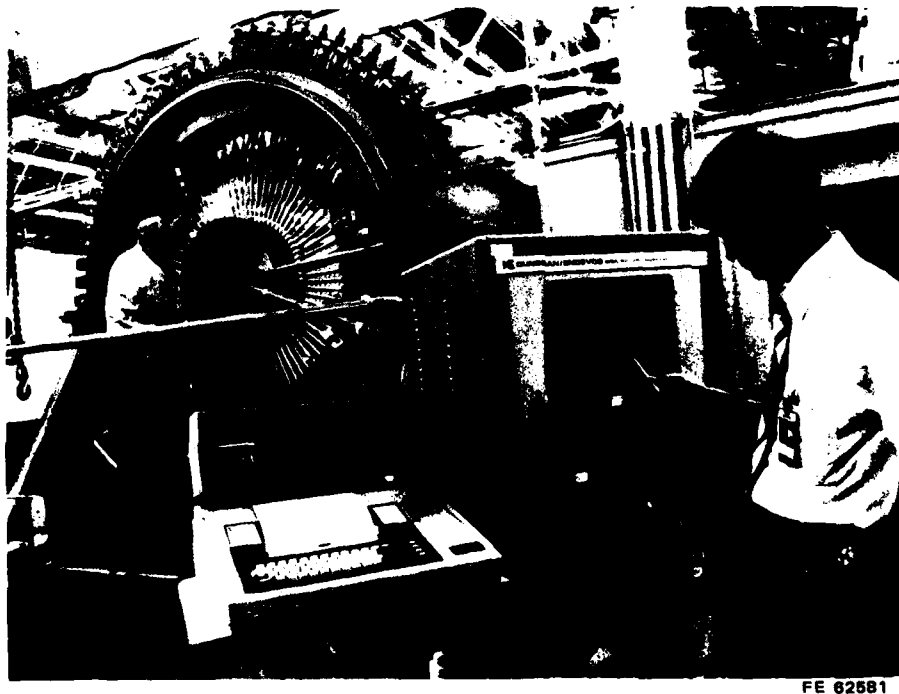
Figure 10. TF30 10th-Stage Compressor Disk (Bore-Modified) Installed in the "Ferris Wheel"

Real time AE inspection was performed during disk fatigue testing using the Dunegan/Endevco (D/E) high temperature sensors (Model D9205M2) and the GPD computerized AE system shown in Figure 11. Figure 12 shows the system schematic. Two programs, using four-sensor arrays, were available for linear or two-dimensional source location AE inspection, as illustrated in Figure 13a. A modification to the array, shown as Figure 13b, consisting of sensors mounted 90 deg apart on the disk surface at a constant radius was used for real time compressor disk inspection

Three variations of FP inspection were used during the compressor disk program. Laboratory static and stress-enhanced procedures were developed at the onset of the program, and standard production-type FP was used as a reliability reference.

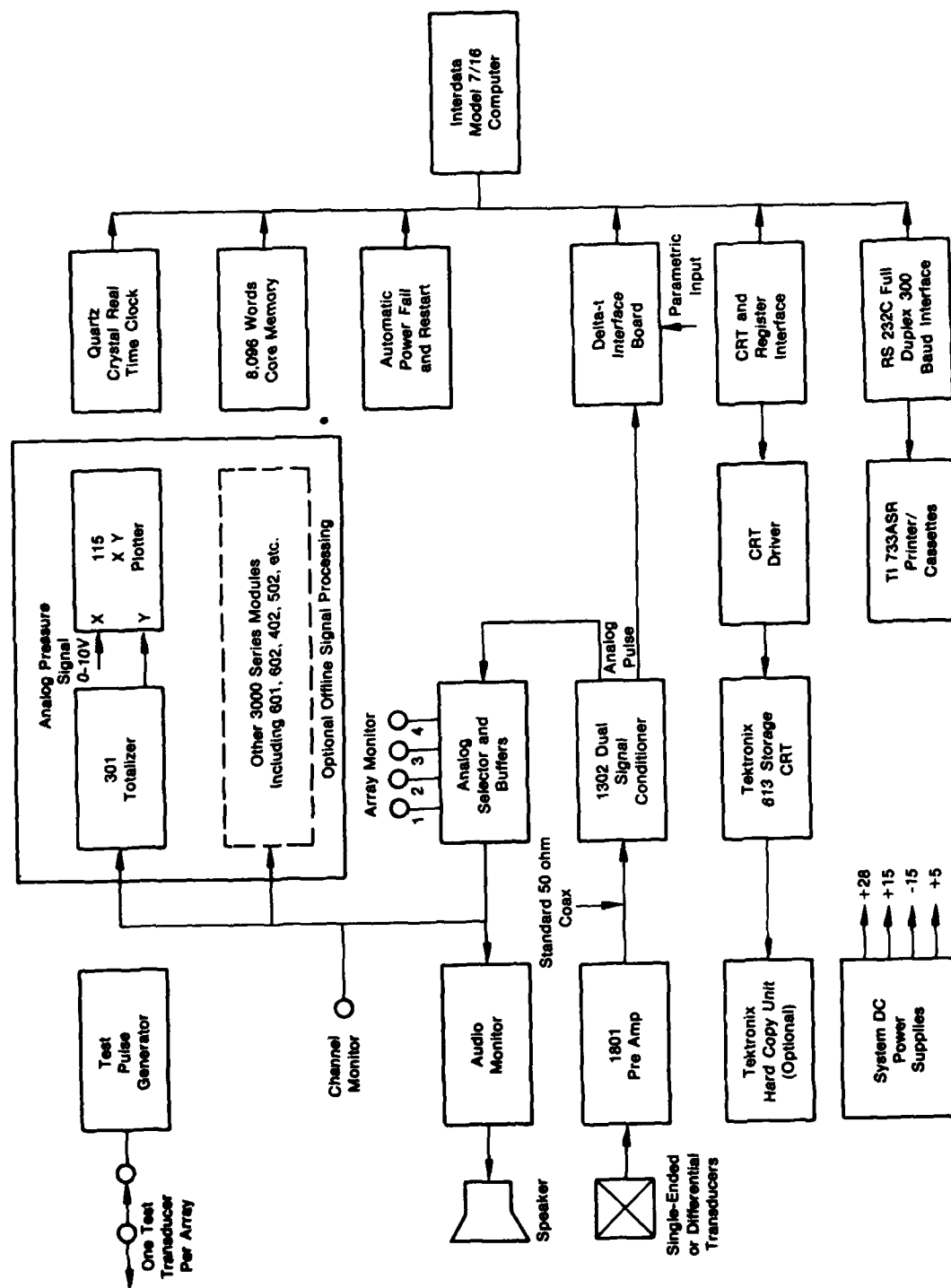
TEST PROCEDURES

During the material characterization task, strain-controlled LCF testing of Incoloy 901 was conducted at temperature and strain conditions simulating the ferris wheel disk test conditions. Strain level was determined from a strain gage survey performed on the disk bolt-holes (primary critical location). This simple geometry testing was performed to determine the AE response during the total fatigue life of this disk material and to confirm the correlation between strain-control specimen initiation lives and initiation lives of disk critical locations. As detailed in Section III: Test Results, the premise appears to be valid that the fatigue mechanism in a disk critical location is strain controlled during engine-simulating LCF and may be simulated by a strain-controlled test on a simple specimen.



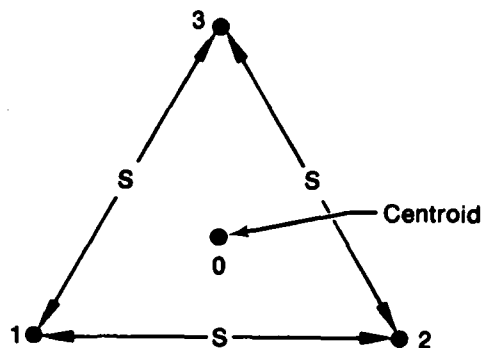
FE 62581

Figure 11. GPD Computerized Acoustic Emission Real Time Inspection System

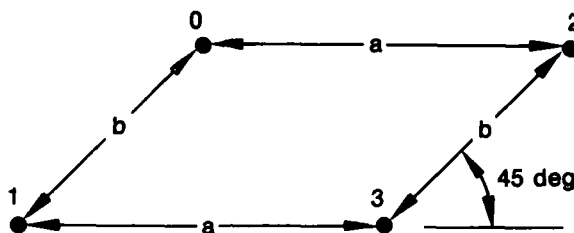


FD 173107

Figure 12. Dunegan/Endevco Model 1032 System Schematic



a. Standard "Quad" Array (Transducer "O" May Be Replaced by Three Parallel Transducers for Disk Inspections)



b. Alternate Array

FD 148909

Figure 13. Dunegan/Endevco Model 1032 Computerized AE System Transducer Arrays

Bolthole simulation LCF testing of Incoloy 901 was also conducted as part of the material study to demonstrate the correlation between a complex geometry specimen test and a fatigue test of a full scale disk. The tests were used to establish AE response levels during fatigue of Incoloy 901 and to provide a test bed and control sample for assessment of periodic inspection techniques. Testing was conducted at strain and temperature conditions simulating the simple cycle disk test conditions. Results of a strain-gage survey, Figure 14, revealed elastic stress vs strain after the first room-temperature cycle (stress vs strain was similar for the disks). A room-temperature maximum strain range (measured at the center of the bolthole) of 0.80% was selected as the representative test condition.

Crack propagation testing was conducted at 400°F, $\nu = 10$ cpm, $R = 0.05$, to model propagation during simple-cycle compressor disk testing. Two tests were also conducted at $R = 0.5$ to develop a base for disk duty cycle modeling.

Fracture mechanics data regression at GPD has been fully computerized using a model based upon the hyperbolic sine (sinh). The sinh model shown in Figure 15 was developed as a flexible alternative to the familiar Paris equation and is represented as:

$$\log (da/dN) = C_1 \sinh (C_2 (\log \Delta K + C_3)) + C_4 \quad (1)$$

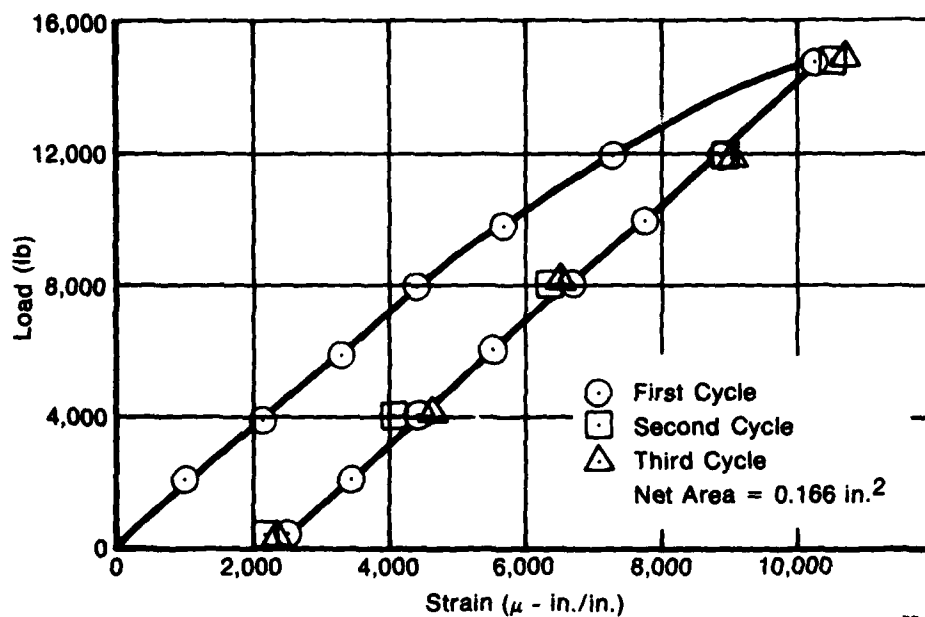


Figure 14. Incoloy 901 Bolthole LCF Specimen Room Temperature Strain Survey

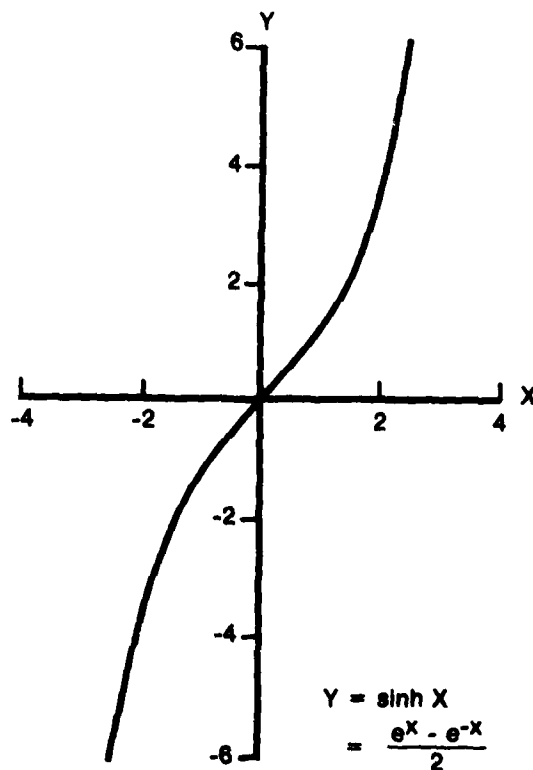


Figure 15. Hyperbolic Sine on Cartesian Coordinates

The coefficients discussed in References 1, 2 and 3 are simple functions to test frequency, stress ratio, and temperature, as shown in Figure 16. These are three of the fundamental influencing factors on crack propagation. Retardation effects are not considered by this model, but an overload test was conducted and used to improve the accuracy of the disk duty cycle life calculation (see Section III: Test Results).

The resulting model provides the vehicle for applying linear elastic fracture mechanics (LEFM) to LCF residual life predictions of disk components subjected to missions of varying cyclic frequency, stress ratio, and temperature. This assumes the limits of applicability of LEFM at elevated temperature have been defined.

ACOUSTIC EMISSION INSPECTION PROCEDURES

AE Rate Analysis

Typically, an AE event from the receiving transducer may be represented as a damped sinusoid, as shown in Figure 17. The AE "counts" are measured as the system threshold is exceeded in the positive direction. An AE rate analysis indicates the number of times the preset threshold has been crossed during one test cycle, regardless of the absolute number of AE events or wave packets that may have been received.

AE rate is the most commonly used form of AE inspection to determine variations in mechanical stress wave activity from a specimen or component which is experiencing cyclic loading.

Amplitude Distribution

Amplitude distribution analysis is an important mode of AE signal processing and probably the most widely accepted form of distribution analysis. The Dunegan/Endevco analyzer displays transduced signal peak amplitude. A linear AE signal is converted to logarithmic form thereby creating a wide dynamic range. The log amplified signal is peak detected and an analog-to-digital converter then outputs a series of 0 to 100 pulses that represent peak amplitude in decibels, with 1 dB resolution.

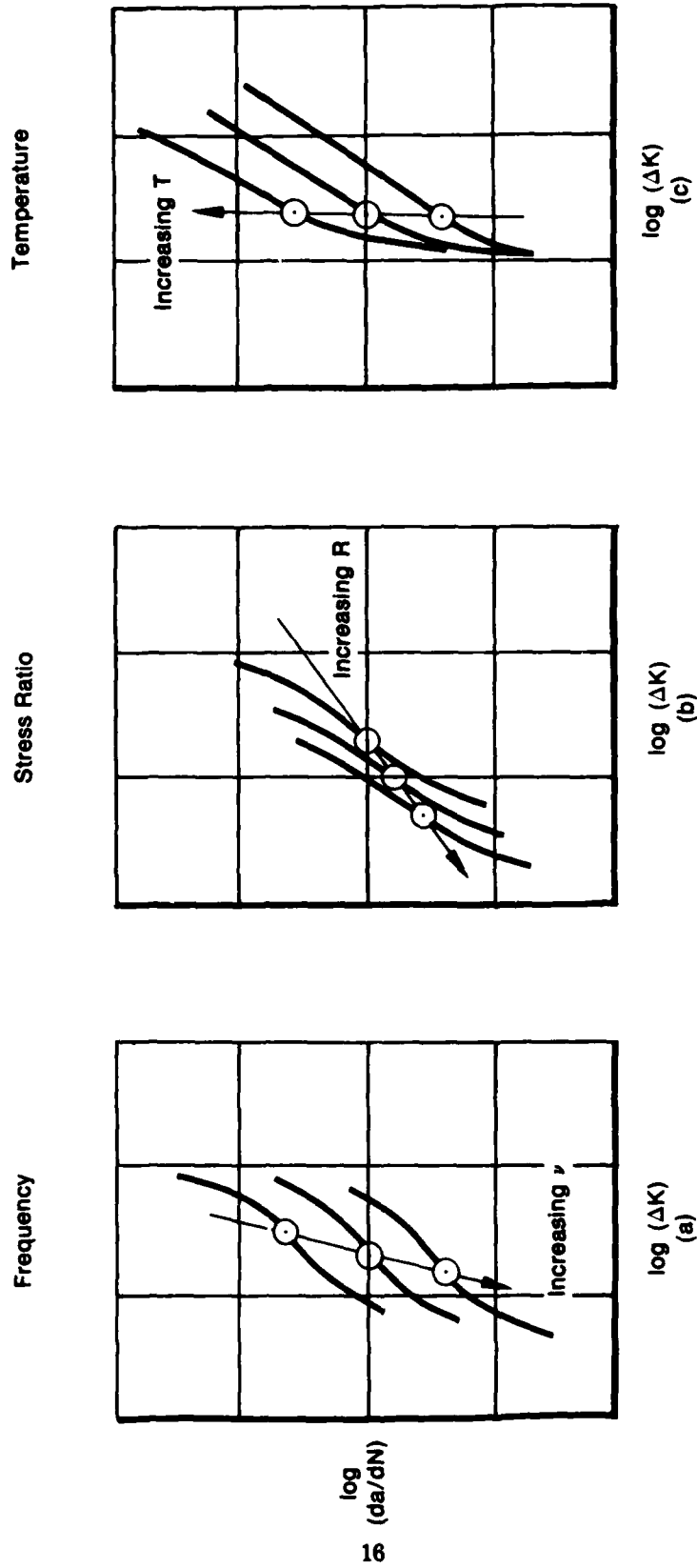
The summed peak amplitude distribution function, $E(V_o)$, is the number of events with amplitudes exceeding a given voltage value, V_o . It is of the form:

$$E(V_o) = KV_o^{-b} \quad (2)$$

where K and b are constants for a given increment of loading on a structure. The exponent, b, is sensitive to changing distribution patterns and has therefore been used as an indicator of general structural integrity in monotonic loading situations.

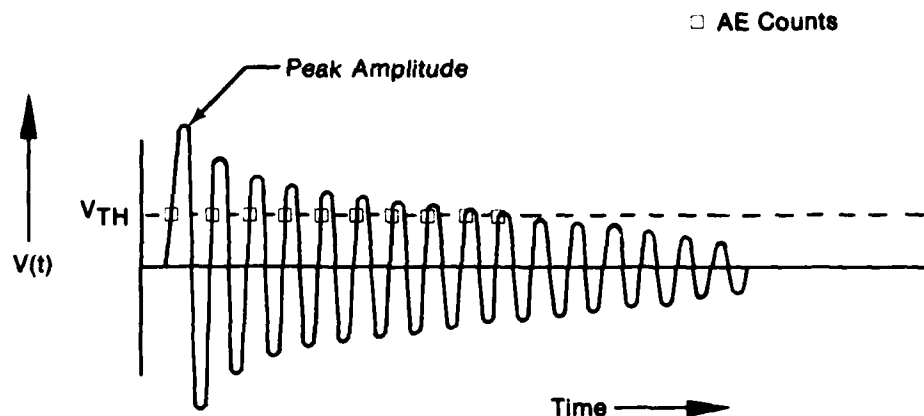
In the logic of the distribution analyzer, each pulse represents the ratio of the input signal to $100\mu V$ (in decibels) through the relation:

$$\text{Pulse} = 20 \log \left(\frac{V_{in}}{100\mu V} \right) \quad (3)$$



FD 111944

Figure 16. Crack Propagation Influenced by Frequency (a), Stress (b), and Temperature (c)



FD 148902

Figure 17. Classical Representation of an AE Event

Pulse Width Distribution

The pulse width distribution analyzer counts the time (10μ sec resolution) than an envelope processor is energized, i.e., pulse width per event. An event is defined when the processor is energized at the first pulse of a burst. It remains energized during the burst and stays energized for a fixed envelope time after the last pulse of the burst above threshold. The end of the envelope time is defined as the end of an event. Total time the processor is energized is the burst pulse width.

Ringdown Counts Per Event

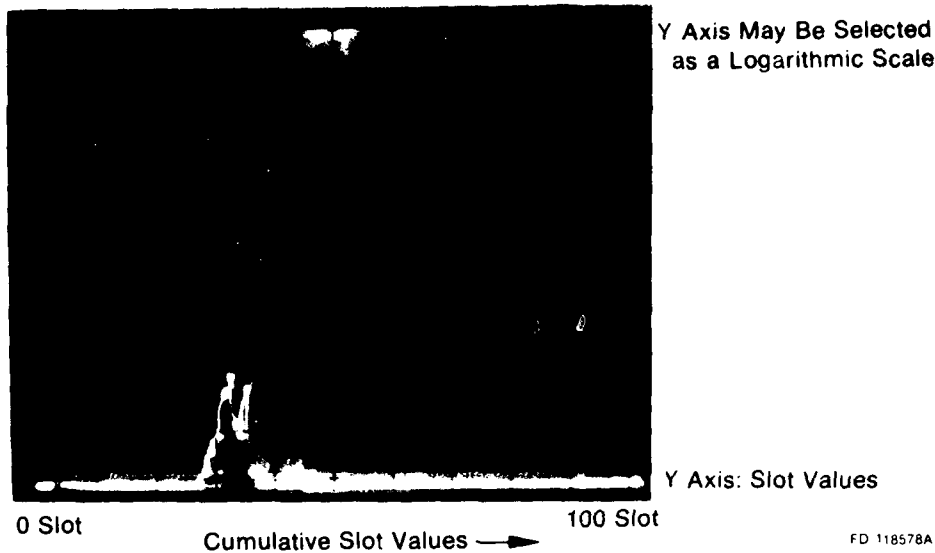
The ringdown counts distribution analyzer monitors the number of threshold crossings in each AE event. For a perfectly resonant transducer with a narrow frequency band, ringdown counts per event, pulse width, and peak amplitude would all be directly related when monitoring rapidly decaying burst-type AE. The transducers used during this program were uniformly sensitive (within 5 dB) over a 300 kHz bandwidth, having a resonant frequency near 650 kHz. Though the burst-type AE monitored during LCF testing displayed exponential decay in many cases, the three distributions functioned somewhat independently with amplitude being the most autonomous.

Source Location and Analyzer Operation

The Dunegan/Endevco Model 920 Distribution Analyzer sorts AE events (bursts) according to time domain signal characteristics (pulse width, peak amplitude, ringdown counts, or one-dimensional source location). Each processed event is assigned a "slot" value from 0 to 100 according to the selected time-domain analysis, full-scale selection, and signal value. Analyzer output is then displayed in histogram form with slot values displayed along the X-axis and number of events assigned to each slot displayed along the Y-axis.

Figure 18 shows an oscilloscope display of a typical analyzer output. As an example, if the analyzer had been operating in a one-dimensional source locate mode, the X-axis would represent the distance (divided into 100 increments) between a transducer located at "0" and a second transducer located at "100." the Y-axis output would display the number of AE events whose source locations correspond to each of the 100 distance increments. Events whose sources are outside the boundaries determined by the two transducers are automatically assigned to either slot value 0 or 100.

Y Axis:
Number of Events at
Each Slot Value



FD 118578A

Figure 18. Distribution Analyzer Histogram, Normal Output

As an example of one-dimensional source location, suppose transducers 0 and 100 were located 100 in. apart on a length of pipe which is being proof tested. Each slot value (X-axis) would correspond to a 1-in. increment of pipe. If, as the test progressed, the distribution analyzer output appeared as in Figure 18, the test engineer would suspect structural damage in a region located roughly one-third of the distance between the transducers. The bulk of acoustic activity occurs between slot locations 28 and 44, with highest registry occurring at slot 32. AE analysis is explained in further detail in Appendix A.

To conduct two-dimensional source location on a disk configuration, one more transducer and an additional distribution analyzer are required. Transducers are placed 120 deg apart near the disk outside diameter, different pairs of transducers are assigned to each of the two analyzers, and the surface is mapped using a transmitting transducer. Response from each analyzer is recorded as the transmitter (simulated AE) is placed at various locations on the disk. Finally, curved lines of constant analyzer readings are mapped along the disk for each distribution analyzer and the two-dimensional source location of an event is determined by the intersection of two of these lines. Two-dimensional source location analysis may be performed on many other surface configurations using similar methods, while the introduction of a third distribution analyzer permits three-dimensional analysis in specialized cases.

EDDY CURRENT INSPECTION PROCEDURES

GPD-Nondestructive Test Engineering performed disk EC inspections using a Circograph Model 6.230 semi-automatic inspection system from which reliability figures were calculated. For each periodic inspection, the disk was removed from the ferris wheel and set on a special fixture, illustrated in Figure 8, for a rotating-probe bolthole inspection. To produce maximum sensitivity, a very tight probe was developed to allow only a few thousandths of an inch clearance between probe and bolthole walls. Circograph inspection of a disk bolthole or bolthole-simulation specimen is performed while a rotating probe (differentially wound) is

lowered into the bolthole, never actually making contact with the specimen. Any defect inside the bolthole will disturb the passing EC field and a processed signal from the defect will appear on the Circograph storage oscilloscope. This is made possible by synchronous action of the rotating shaft and the scope, producing a 360-deg sweep of the bolthole with each sweep of the scope.

Later in the program, a different EC instrument was used for specimen and disk bolt-hole inspection. the Gulton FD100 instrument shown in Figure 7 provided the advantage of being able to perform inspections with the subject disk installed in the ferris wheel. Using the small, hand-held, semi-automatic fixture, static and stress-enhanced inspections could be performed with minimal effort. Sensitivity of the Gulton instrument probably is not as good as sensitivity of the Circograph due to the relatively low operating frequency of the Gulton instrument, but introduction of the Model FD100 into the program came too late to produce a direct sensitivity comparison for small flaws (less than 1/32-in. length).

FLUORESCENT PENETRANT INSPECTION PROCEDURES

In addition to production-type FP performed by the manufacturing department at GPD, two laboratory-grade FP procedures were developed for inspection of compressor disk bolt-holes, as illustrated in Figure 19. A static laboratory FP method, using Group VI penetrant and wet developer, was established to determine the maximum fatigue crack detection capability which could be expected with standard FP evaluation. This procedure is outlined in Table 1. A stress-enhanced (wink) procedure was also developed to produce the maximum flaw detecting capability using an enhancement method. The procedure was proven to be as effective as the laboratory EC procedures. However, it must be noted here that the compressor disks were virgin, and many of the difficulties encountered in field FP inspection of used components did not exist during this program. The stress-enhanced procedure is listed in Table 2.



FD 149001

Figure 19. TF30 10th-Stage Compressor Disk S/N G82568: Fluorescent Penetrant Indications at Boltholes. Fatigue Cracks Produced by Ferris Wheel Cycling at 400°F, 3 cpm, $R = 0.07$, $\Delta\epsilon_{max} = 0.85\%$

TABLE 1
STATIC FPI PROCEDURE FOR TF30 10th COMPRESSOR BOLTHOLES

-
1. With disk at room temperature, thoroughly clean bolthole area with Magnaflux ZC-7 cleaner or acetone. Use cotton swab to clean inside and edges of the holes.
 2. Allow the disk to dry for 5 minutes before applying penetrant.
 3. Apply Magnaflux ZL-35 inside and at the edges of the holes using cotton swabs. Dwell for 30 minutes.
 4. Wipe excess penetrant with clean cloths and swabs.
 5. Apply Magnaflux ZR-10 emulsifier (diluted with 64 to 70% water) in and around bolt-holes using swabs. Dwell for a maximum of 3 minutes.
 6. Thoroughly clean boltholes and surrounding area with water and swabs. Check progress of cleaning with black light. If additional cleaning is required, repeat steps 5 and 6.
 7. Apply a thin coating of wet-developer Magnaflux ZP-9 (preferably water soluble type, formula C).
 8. 10 minutes after the application of developer use black-light to inspect the bolthole areas inside and at the edges.
 9. Record locations and sizes of all indications sheet.
 10. Clean the bolthole areas with water and then cleaner or acetone.
-

TABLE 2
WINK FLUORESCENT PENETRANT INSPECTION PROCEDURE
(TF30 10th Compressor Disk Boltholes)

1. Thoroughly clean the boltholes with cleaner or acetone — using swab to clean inside of the holes.
2. Load the disk at 50 to 75% of maximum load.
3. Apply ZL-30 inside and at the edges of the holes using swabs.
4. Cycle load five to seven times between P_{min} and 50 to 75% load. Dwell for one minute, each time 50 to 75% load is reached.
5. Unload the disk and wipe excess ZL-30 from boltholes with clean cloth and swabs.
6. Apply emulsifier in and around boltholes (maximum emulsification time 2 to 3 minutes).
7. Thoroughly clean boltholes and surrounding area with water and swabs. Check progress of cleaning with black light. If additional cleaning is required, repeat steps 6 and 7.
8. Apply a thin coating of wet-developer ZP-9 (preferably water-soluable type).
9. Cycle load five to seven times between P_{min} and 50 to 75% load. Dwell for 30s each time 50 to 75% load is reached.
10. Unload the disk and inspect with black light. Record locations and sizes of all indications.
11. Clean the bolthole area with water and then cleaner or acetone.

NOTE:

The above procedure is wirtten for maximum sensitivity required during crack initiation studies. Load for wink procedure should be reduced as the cracks are inspected beyond initiation stage. Loading may be completely eliminated once the cracks are beyond initiation stage.

SECTION III TF30 10th-STAGE COMPRESSOR DISK TEST RESULTS

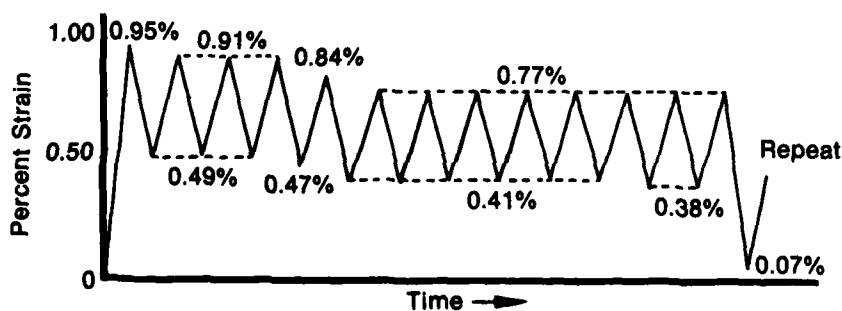
STRAIN-CONTROLLED LCF

Seven strain-controlled low cycle fatigue (LCF) specimens were tested at conditions simulating the disk LCF tests. Test temperature was 400°F, and strain conditions duplicated the maximum calculated strain condition for the disk boltholes. The maximum strain measured in a disk bolthole (at a location nearest the disk bore) during room temperature strain surveys was 0.90%, with a strain range of 0.84%. Using a Young's Modulus adjustment to 400°F, the calculated maximum strain for the same maximum bolthole stress was 0.95%. Strain range was calculated to be 0.88%. Four LCF specimens were tested at these strain conditions. Table 3 details the results.

TABLE 3
STRAIN CONTROLLED LCF TESTING OF
INCOLOY 901 AT 400°F FOR
COMPRESSOR DISK SIMULATION

S/N	Cyclic Frequency	Strain Range	Failure
901-3	5 cpm	$\Delta\epsilon = 0.88\%$, $\epsilon_{\max} = 0.95\%$	1763 cycles
901-4	5 cpm	$\Delta\epsilon = 0.88\%$, $\epsilon_{\max} = 0.95\%$	997 cycles
901-5	Mission	See Figure 79	973 missions
901-6	5 cpm	$\Delta\epsilon = 0.88\%$, $\epsilon_{\max} = 0.95\%$	1262 cycles
901-7	5 cpm	$\Delta\epsilon = 0.88\%$, $\epsilon_{\max} = 0.95\%$	Shutdown at 1082 cycles
901-8	Mission	See Figure 79	724 missions
901-9	Mission	See Figure 79	650 missions

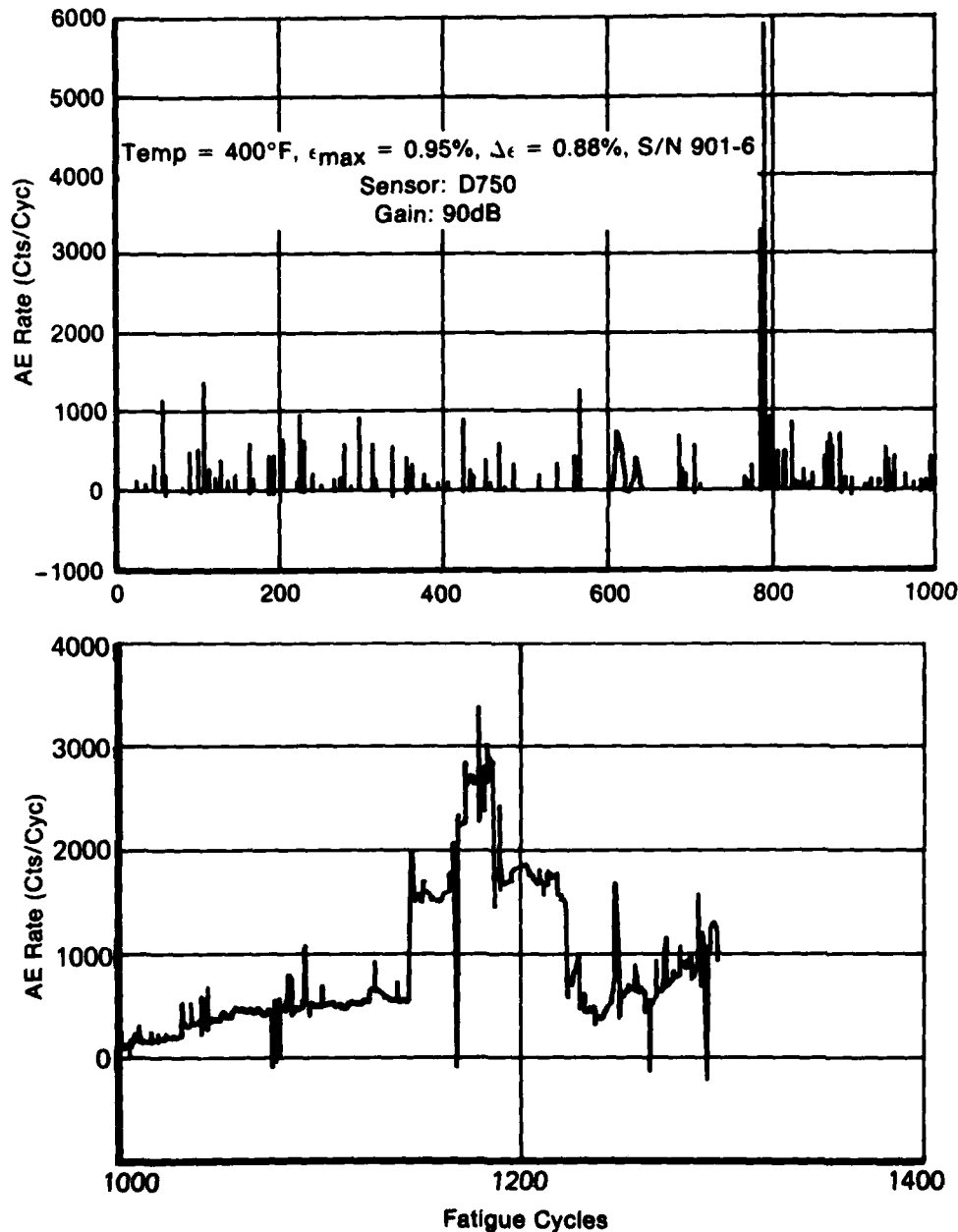
Three additional strain-controlled LCF specimens were tested to a disk duty cycle approximation. This mission is illustrated in Figure 20. Again, room temperature strain was modulus-adjusted to produce elevated temperature strain calculations. Maximum and minimum strain for each subcycle was ratioed from maximum and minimum loads for the ferris wheel test.



FD 175109

Figure 20. TF30-P-412 Strain Control Simulation of 10th-Stage Compressor Disk LCF Test Duty Cycle Definition, Temperature 400°F

A typical acoustic emission (AE) rate (vs fatigue cycles) plot is shown in Figure 21. Spatial discrimination techniques used in similar programs have shown that extraneous noise is minimal during strain-controlled LCF testing in the test fixture used during this program. It is therefore apparent from Figure 21 that the specimen was acoustically active during most of the test, with several large bursts of emission near cycle 800 and more concentrated activity occurring thereafter. Rate records from some of the other strain-controlled LCF tests did not exhibit the activity observed near cycle 800 of test S/N 901-6, but each AE rate record did display a marked increase in activity during the final part of the test.



FD 175110

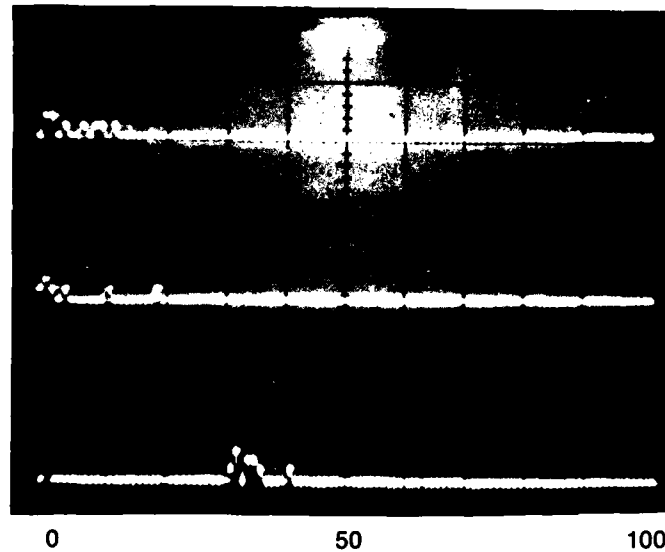
Figure 21. Acoustic Emission Rate Analysis: Strain Controlled LCF Testing of Incoloy 901

Time-domain distribution analyses (peak amplitude, pulse width, and counts per event) were performed as a real time inspection method. Periodic photographic records were made of the distribution analyzer histogram outputs periodically during each test, with the analyzer being reset (to clear storage) after each photograph was taken. Histograms from two cyclic periods of test S/N 901-6 are shown in Figure 22. Note that Figure 22a includes records for all three distribution analyses, while Figure 22b just shows the record for the "counts per event" distribution. Scaling is the same for both photographs. While pulse width and amplitude records appeared to change little during the course of each strain-controlled LCF test (and are not shown in Figure 22b, the counts per event record did display a relatively large change in maximum counts per event as each test progressed. This phenomenon would con-
note a change in the signal frequency content during the course of each test.

Pulse Width
(10 millisecc F/S)

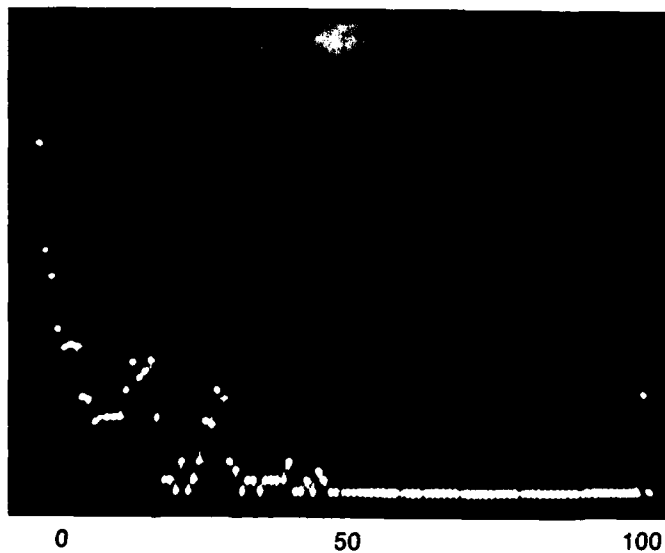
Counts Per Event
(10^3 Counts F/S)

Peak Amplitude
(100 dB F/S)



(a) Cumulative Record for Cycle 1 to Cycle 160

Counts Per Event
(10^3 Counts F/S)



(b) Cumulative Record for Cycle 971 to 1262 (Failure)

FD 175111

Figure 22. Acoustic Emission Multiparameter Distribution Analysis: Strain Controlled LCF Testing of Incoloy 901

The Dunegan/Endevco transducer used during this program was a Model D750 differential sensor. It is resonant near 700 kHz (see Appendix A), but maintains fair sensitivity over a frequency range of less than 300 kHz to over 1.0 MHz. Bandpass filtering was performed over this same range. Using the following expression to calculate an "average" frequency content of an AE burst,

$$\nu_{avg} = \text{counts per event} / (\text{signal pulse width-envelope time})$$

it is apparent that the events registered during early stages of the test record shown in Figure 22 were of average frequency toward the lower end of the bandpass range. As testing progressed and "counts per event" registries increased to 500 and greater, with little increase in maximum pulse widths, a frequency content toward the upper end of the bandpass range may be calculated for some signals. Unfortunately, the GPD laboratory capability did not include apparatus for frequency-domain AE analyses.

In order to determine the fatigue mechanism associated with the observed AE frequency changes, test S/N 901-7 was discontinued early for metallographic analysis of the specimen. The arbitrary criteria established for test discontinuation was registration of more than twenty events during a one-hundred cycle period with "counts per event" greater than 100. During the cyclic period of test S/N 901-7 from cycles 982 to 1082, 23 events occurred with "counts per event" greater than 100. The specimen was then sectioned axially and subjected to metallographic analysis. In addition to microcracking, Figure 23 shows a twinning mechanism observed in the most highly stressed region of the gage section. This fatigue mechanism was substantially different than that observed in the GATORIZED® IN100 study.

Monotonically Increasing Counts Per Event



Mag: 1000X

Microcracking and Twinning

FD 175112

Figure 23. Acoustic Emission Time Domain Analysis: Applied to Fatigue Initiation Classification of Incoloy 901

BOLTHOLE SIMULATION LCF

Three bolthole LCF specimens, fabricated from Incoloy 901, were tested at 400°F for comparison with ferris wheel initiation testing of compressor disks. The tests were also used for development of the nondestructive evaluation (NDE) tools used during the disk program. Pertinent test data are listed in Table 4.

TABLE 4
INCOLOY 901 LCF BOLTHOLE TESTING

Test No.	Heat Code	Net Stress (ksi)	Temp (°F)	*N _I	N _F	
1081	AFZD	92.0	400	0.05	1500	2950
1082	AFZD	92.0	400	0.05	3200	**
1233	AFZD	92.0	400	0.05	1900	**

*Determined by real time AE inspection.

**Used as eddy current standard.

Bolthole specimens were tested at a cyclic rate of 10 cpm, with real time AE time-domain inspection. Sensors used were Dunegan/Endevco Model D750 differential transducers operating at a gain of 90 dB. AE rate analyses were performed, as well as pulse-width and amplitude-distribution analyses. Pulse-width distribution analyses were over a range of 0 to 10 milliseconds, with a 100-microsecond envelope (dead time). Amplitude distributions were taken above a threshold of 30 dB (referenced to 100 microvolts) with a 10-millisecond envelope. All of the above parameters were selectable using the Dunegan/Endevco Model 920 Distribution Analyzer and Model 921 Amplitude Processor.

Cycles-to-flaw detection (1500 to 3200) in the bolthole specimens tested at 400°F compared favorably with cycles-to-flaw detection at individual disk boltholes (800 to 2500, see Section III: Test Results, Compressor Disk Testing). However, the NDE method which first detected flaws differed from specimens to disk (real time AE vs periodic fluorescent penetrant (FP) and eddy current (EC), respectively).

Specimen S/N 1082 contained a fatigue crack with 0.070-in. surface length when the test was discontinued at 5000 cycles. Replication technique was used to document this flaw before the specimen was removed and saved as an inspection standard. Figure 24a shows a photograph of the replica taken with no load applied to the specimen (edge of the bolthole is shown on the upper end). The irregular shape of the crack is typical for Incoloy 901. Figure 24b illustrates the same crack under 50% of the maximum test load. It is apparent that application of relatively low stress can increase crack opening displacement enough to significantly enhance NDE. (See Section IV: Discussion, Compressor Disks Testing).

Late in this program, GPD received a microminiature AE transducer. The sensor measured only 1/8-in. in diameter by approximately 1/16-in. thick. While Figure 25 shows peak sensitivity to be more than 10 dB poorer than sensitivity of the Dunegan/Endevco Model D750, the relative proximity of a microsensor to an inspection "area of interest" could be controlled relatively well. All of the Incoloy 901 bolthole LCF specimens had been tested by the time the microsensor was received, but two GATORIZED IN100 (P/M nickel alloy) specimens were still available to rate the new probe (Dunegan/Endevco Model S9222) against the D750.



Mag: 50X

b) 50% Applied Load

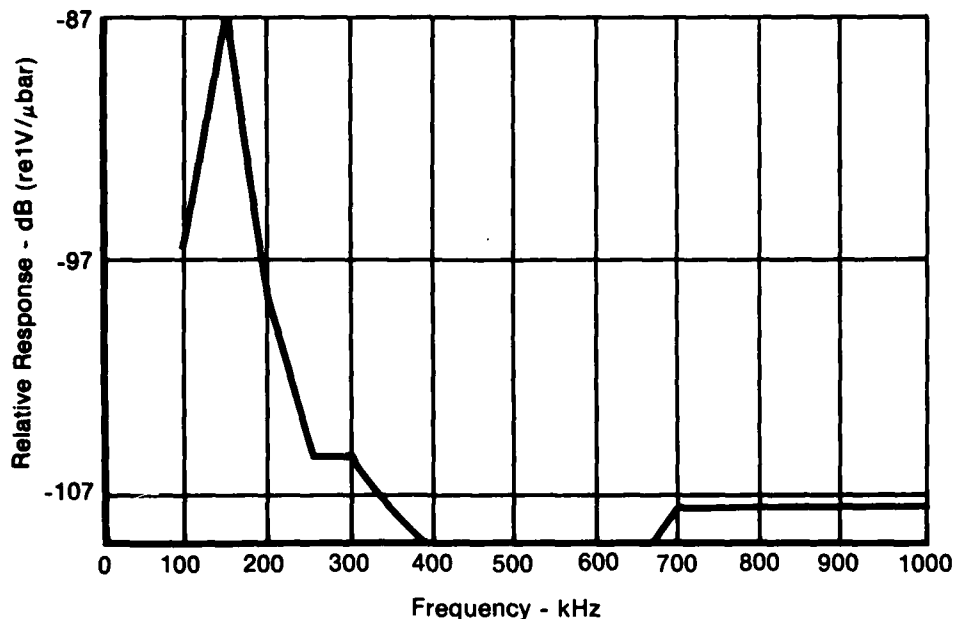


Mag: 50X

a) 0% Applied Load

FD 175113

Figure 24. Fatigue Crack Documentation (Replicas) from Bolthole LCF Specimen



FD 175114

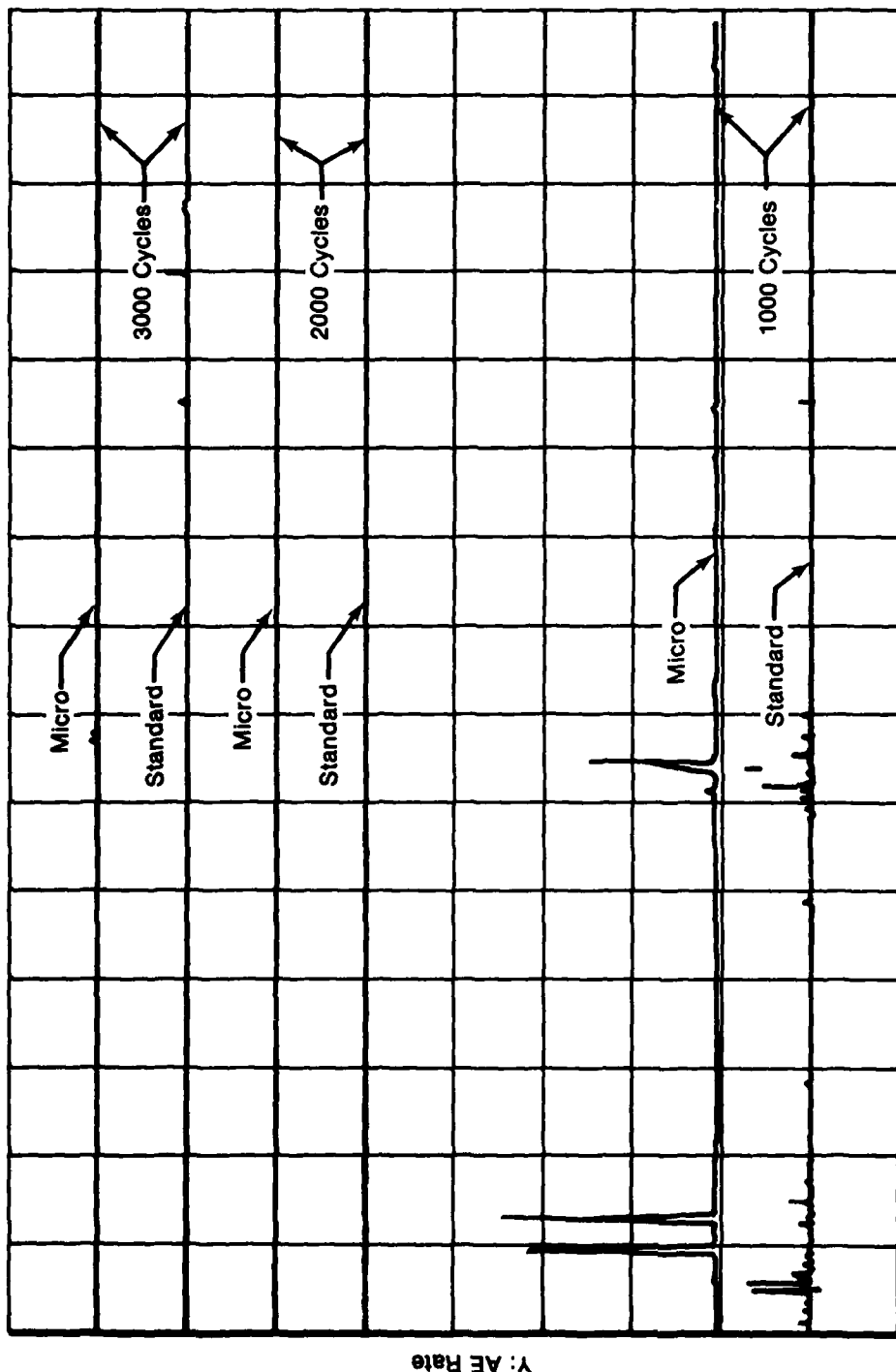
Figure 25. Frequency Response of Microminiature Acoustic Emission Transducer (D/E Model S9222)

The D750 sensor was mounted to a six-in. waveguide and attached to the specimen through a tapped hole (standard monitoring configuration for this program). The microsensor was potted into a silicone rubber (red RTV) button to be pressed into the bolthole. Testing was performed on the bolthole specimen at a net stress of 144 ksi, $\nu = 10$ cpm, $R = 0.05$, at room temperature.

The microsensor was operated at a system gain of 90 dB through a bandpass filter of 100 to 300 kHz. The Model D750 was operated at a total gain of 90 dB through a bandpass filter of 300 kHz to 1.0 MHz. AE rate was monitored on a "per cycle" basis for both transducers. Time-domain peak amplitude distribution analyses were conducted from the microminiature sensor above a threshold of 30 dB, with an envelope (dead time) of 10 milliseconds.

The AE rate record from this test is shown in Figure 26. The multiple traces illustrate that, through cycle 8000, the microsensor appeared to be less sensitive (fewer counts per cycle) to the recorded emission. However, between cycles 8000 and 9000 the situation reversed. The microsensor recorded at least 16 AE bursts of high level activity, while the D750 produced small indications. The comparison of the amplitude distribution for the cycles 7000 to 8000 test increment to the distribution for the cycles 8000 to 9000 test increment appearing in Figure 27 shows no substantial change in the "loudest" recorded peak amplitudes, but the total number of events recorded during the final increment changed drastically (from 873 events to 21,455).

The test was discontinued at cycle 9000 for flaw verification. Stress-enhanced FPI and EC techniques detected a small flaw at a corner of the bolthole. Figure 28 shows an acetate replica confirmed the flaw length at 0.014 in.

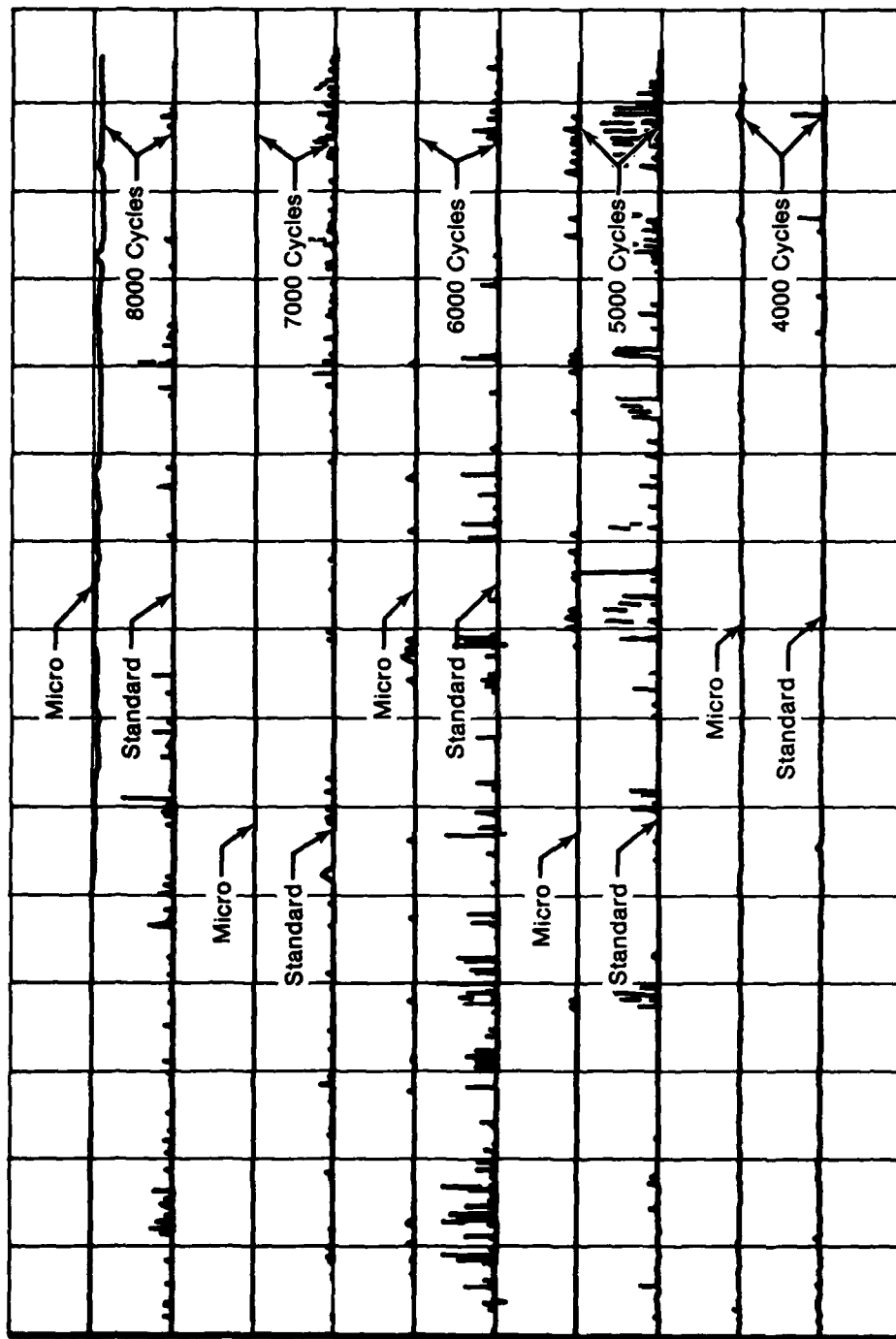


Y: AE Rate

X: Test Cycles

FD 175115

Figure 26a. Acoustic Emission Rate Comparison: Bolthole LCF Test, D750 Sensor (Standard) vs S9222 Sensor (Micro) (Sheet 1 of 3)

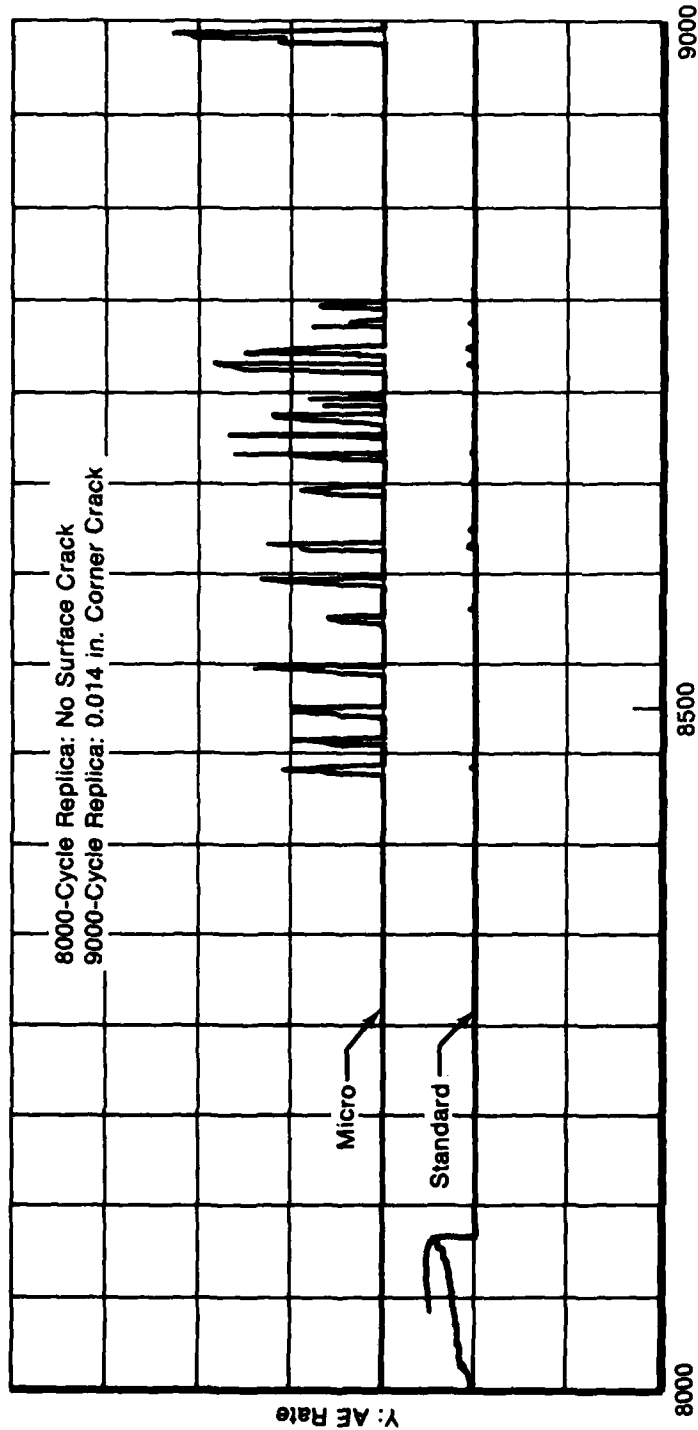


Y: AE Rate

X: Test Cycles

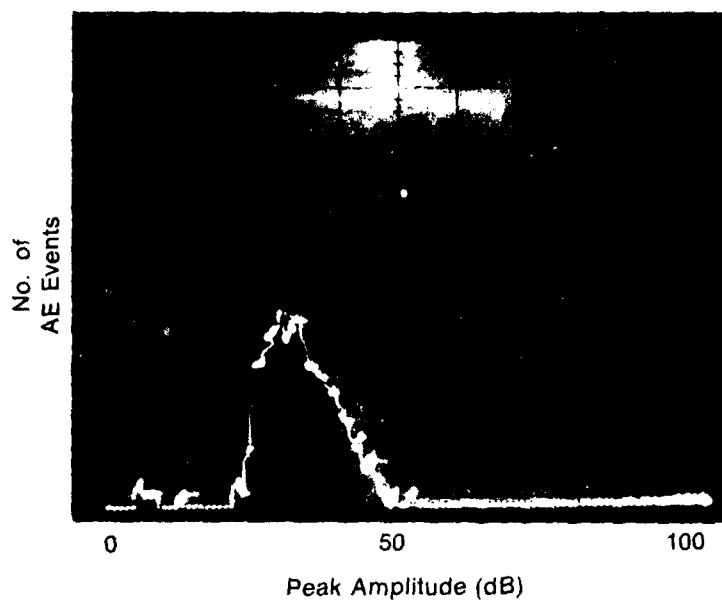
FD 175115

Figure 26b. Acoustic Emission Rate Comparison: Bolthole LCF Test, D750 Sensor (Standard) vs S9222 Sensor (Micro) (Sheet 2 of 3)

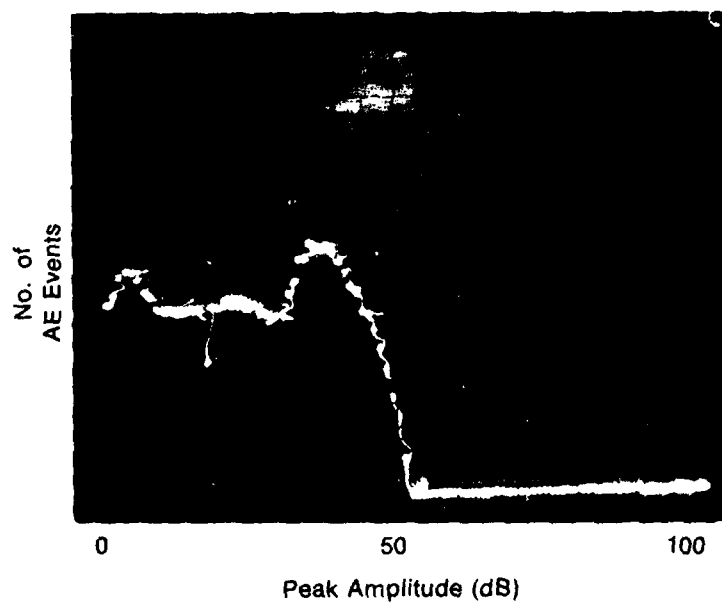


FD 175115

Figure 26c. Acoustic Emission Rate Comparison: Bolthole LCF Test, D750 Sensor (Standard) vs S9222 Sensor (Micro) (Sheet 3 of 3)



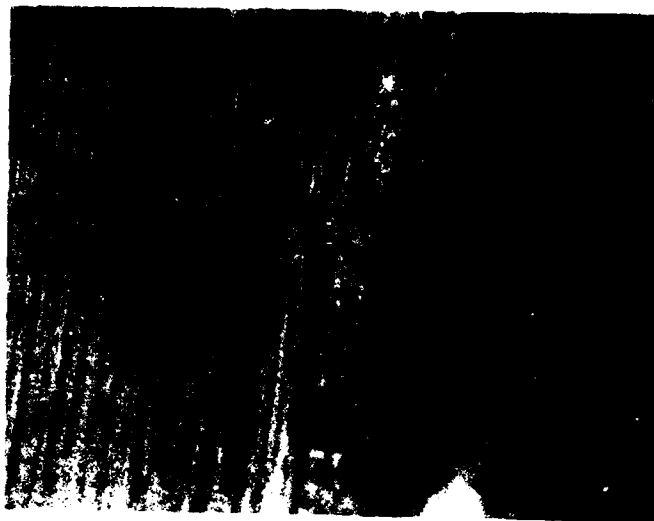
(a) Cycle 7000-To-Cycle 8000 Increment (No Indication)



(b) cycle 8000-To-Cycle 9000 Increment (Crack Indication)

FD 175116

Figure 27. Evaluation of Microminiature AE Sensor Peak Amplitude Distribution Histograms Before Crack Indications and During Crack Indications



Mag: 100X

FD 175117

Figure 28. Fatigue Crack (0.014 in. length) Indicated by Microminiature Acoustic Emission Sensor

While the microsensor was not used to detect fatigue damage in Incoloy 901, the advantage of intimate contact of the sensor with the inspection area of interest (in a material which is an inherently lower level emitter than Incoloy 901) was confirmed through the above demonstration.

FRACTURE MECHANICS (FATIGUE CRACK PROPAGATION)

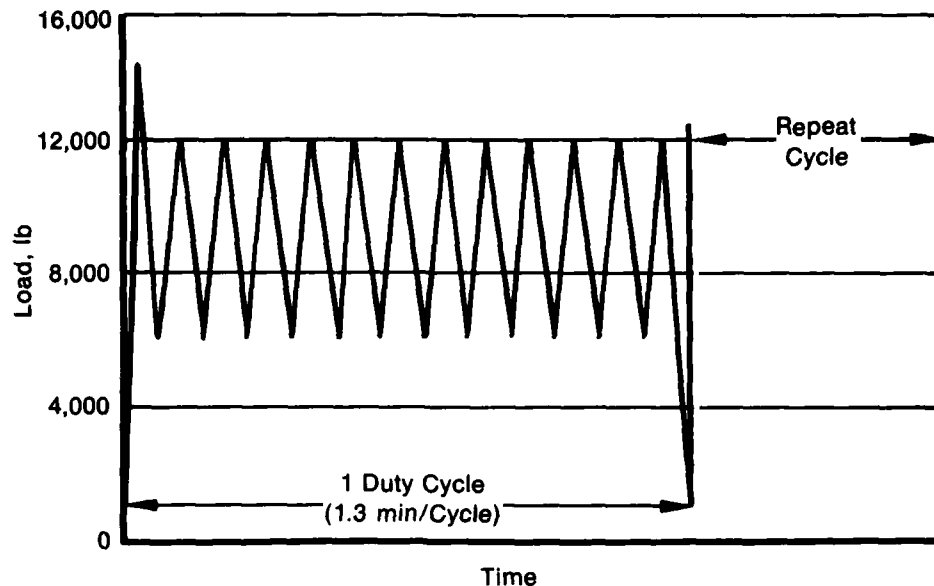
Forgings of Incoloy 901 (PWA 1003), from which the TF30 10th-stage compressor disk is fabricated, were cut and machined into center-flaw fracture mechanics specimens, as shown in Figure 4, for fatigue propagation rate testing. Test conditions are presented in Table 5.

TABLE 5
INCOLOY 901 FRACTURE MECHANICS TESTING

Spec No.	Temp (°F)	Stress Ratio	Initial Net Section Stress (ksi)	Frequency	K_I (max) (ksi $\sqrt{\text{in.}}$)
1189	400	0.05	31.4	10 cpm	15
1408	400	0.05	63.5	10 cpm	25
1413	400	0.05	75.0	10 cpm	32
1188	400	0.05	40.3	10 cpm	20
1434	400	0.05	75.0	10 cpm	34
1572	400	*		*	

*Mission cycle test, details in Figure 29.

Specimens were precracked using procedures set forth by ASTM E-399 (Reference 4). Precracking and propagation testing was performed at room temperature on closed-loop servo-controlled equipment under load control. Cyclic tests were performed using an isosceles triangular load waveform. Specimens were heated using resistance, clamshell furnaces, and the temperature was monitored using thermocouples close to crack planes of the specimens throughout the testing.



FD 175118

Figure 29. Overload Test Profile for Crack Growth Specimen S/N 1572

Crack lengths were measured directly with a traveling microscope with the cyclic load and the furnace removed, holding the specimen at the mean stress level. This procedure held the specimen rigid while opening the crack slightly to make the crack tip more visible. A high-intensity light was used at an oblique angle to the crack to provide illumination and a higher degree of crack tip definition. Attempts were made to measure crack growth in increments no longer than 0.020 in. Crack length measurements were considered to be accurate to within ± 0.001 in.

The raw fatigue crack propagation data (a vs N) were processed and reduced to crack growth rate (da/dN) vs cyclic stress intensity (ΔK) by the Seven Point Incremental Polynomial Technique (Reference 5). A model developed by GPD (see Section II: Experimental Methods) was used to describe the da/dN vs ΔK relationship. The model is based on the hyperbolic sine equation, represented as equation (1), where C_x represents material constants. The hyperbolic sine equation was selected as the model for the following reasons:

1. The equation exhibits the overall shape of typical da/dN vs ΔK plots.
2. All or part of the equation may be used to fit data since the hyperbolic sine has both a concave and a convex half, and a nearly linear portion near inflection. Also, the slope at inflection can vary with the fitting constants. (By comparison, the slope of an X^3 model is always zero at inflection.)
3. The sinh is not periodic (e.g., trigonometric tangent), nor asymptotic (e.g., tangent, or inverse hyperbolic tangent); therefore, when extrapolation becomes necessary, the sinh behaves well at distances removed from the data, quite unlike most polynomial, periodic asymptotic functions.

4. This model requires no information other than a and N data. By comparison, some other models in current use require both K_{th} (threshold stress intensity) and K_{Ic} (critical stress intensity) in addition to a vs N data to model crack propagation behavior. Both K_{th} and K_{Ic} are difficult to obtain experimentally: K_{th} because of the extremely small crack growth measurements necessary, and K_{Ic} because of gross plasticity at the crack tip encountered in fracture toughness testing at elevated temperatures.

The fatigue crack propagation results are presented in Figures 30 through 35. Figure 35 is a duty cycle simulation test result which expresses the crack growth per duty cycle instead of the crack growth per simple sawtooth cycle as appearing in other figures.

AE real time inspection performed during crack propagation tests revealed consistently detectable AE rate levels from each test (Gain = 90 dB). However, as recorded during GATORIZED IN100 propagation tests, there is no monotonic increase of AE rate level with increasing stress intensity. AE distribution analyses also indicated consistently detectable AE levels from crack propagation during the Incoloy 901 tests, but no major trends in parametrical variations were recorded from any test.

COMPRESSOR DISK TESTING

Six (6) TF30 10th-stage compressor disks, shown in Figure 10 and made of Incoloy 901 (PWA 1003), were LCF fatigued to fracture using the GPD ferris wheel fixture shown in Figure 9. Centrifugal loads on engine disks during engine operation were simulated in ferris wheel testing by applying radial loads by means of pressurized hydraulic cylinders operating from a manifold and connected to drawbars simulating the blade/disk attachment configurations.

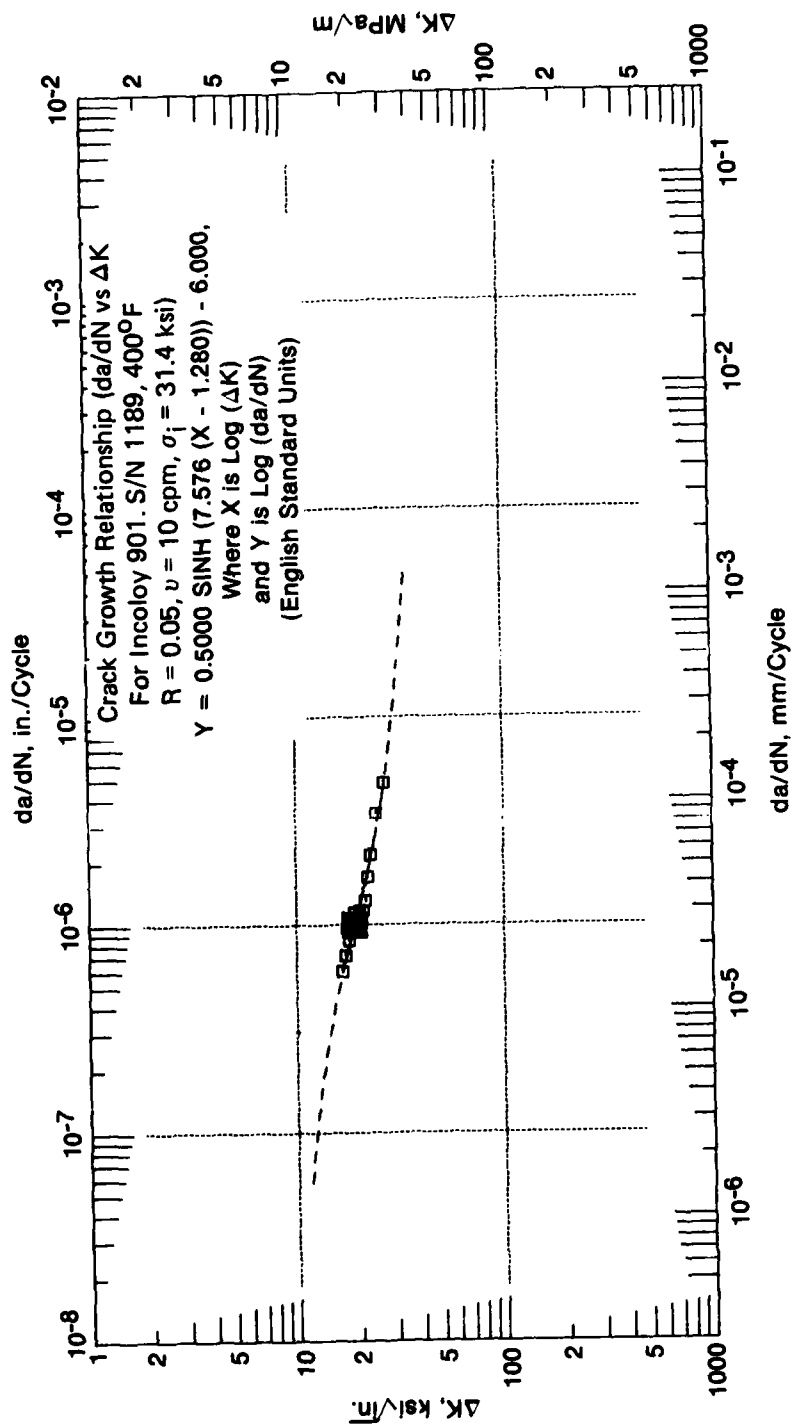
A strain survey was performed on one of the disks at room temperature. The disk was loaded to the maximum cyclic load (4,250 lb) and unloaded. The strain gages were calibrated to zero after the first cycle to eliminate the plastic strain. Strain readings were made during the second and the third cycles.

Tests were performed in both simple sawtooth cycle and mission cycle at 400°F. In simple sawtooth cycle testing, the stress ratio was 0.07 and the frequency was 10 cpm. The temperature was achieved using resistance-heating ovens which sandwiched the test disk faces. Uniform temperature was accomplished by slowing rotating the entire ferris wheel fixture. Figure 36 presents the mission cycle profile.

Three of the disks were tested through initiation-plus-propagation to the simple cyclic condition. The remaining three disks were initiated to a "1/32-in. surface length criteria" using the simply cycle, and propagated to failure using the duty cycle simulation.

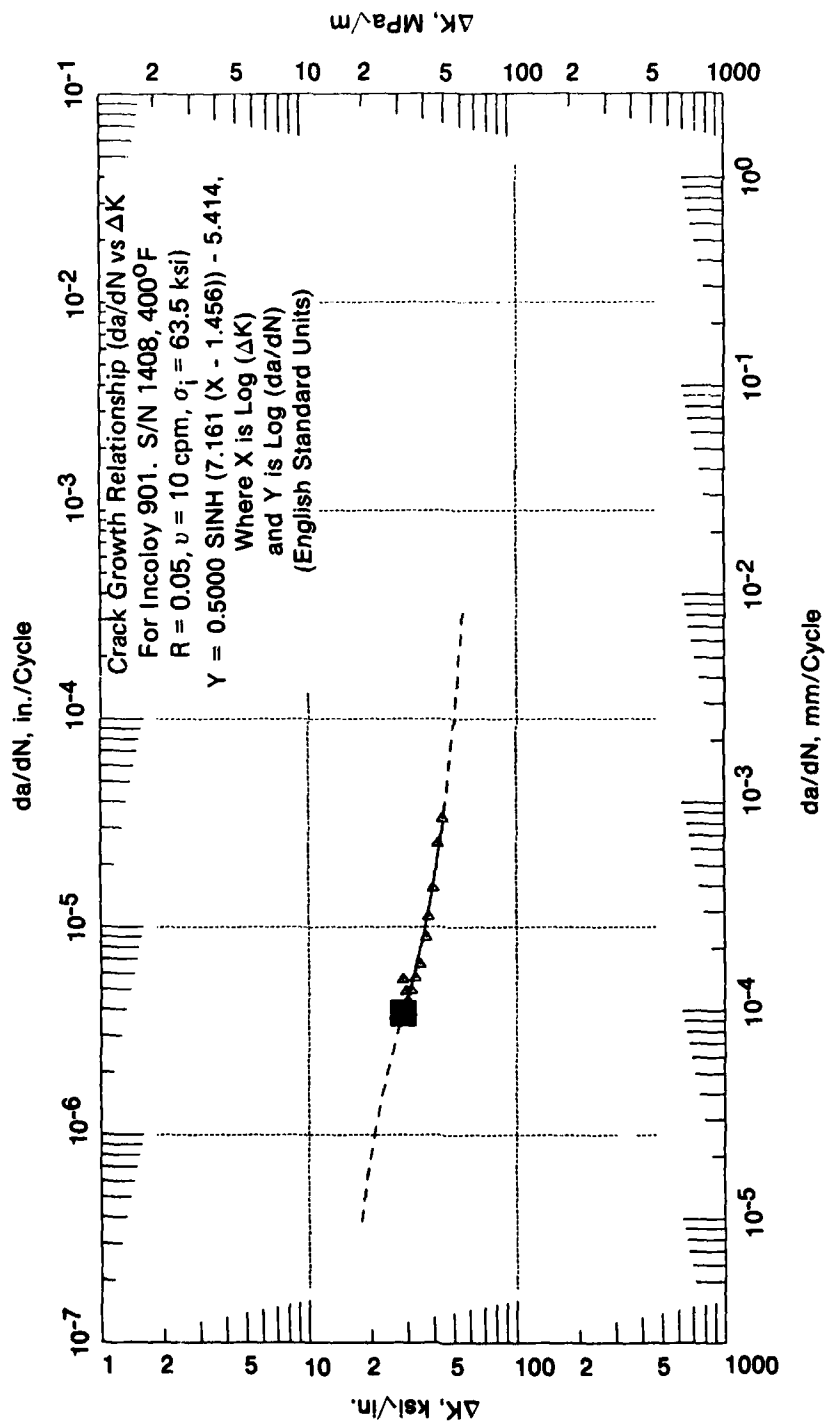
All disk LCF lives quoted in this report have been produced from GPD-MMT experimental data, and are for comparative purposes only. They are not to be construed as official P&WA design field lives.

Fatigue cracks were replicated periodically, usually 100 to 200 cycles, on plastic tapes (acetate acid replication technique) and measured under a microscope. Photographs were made of most crack indications



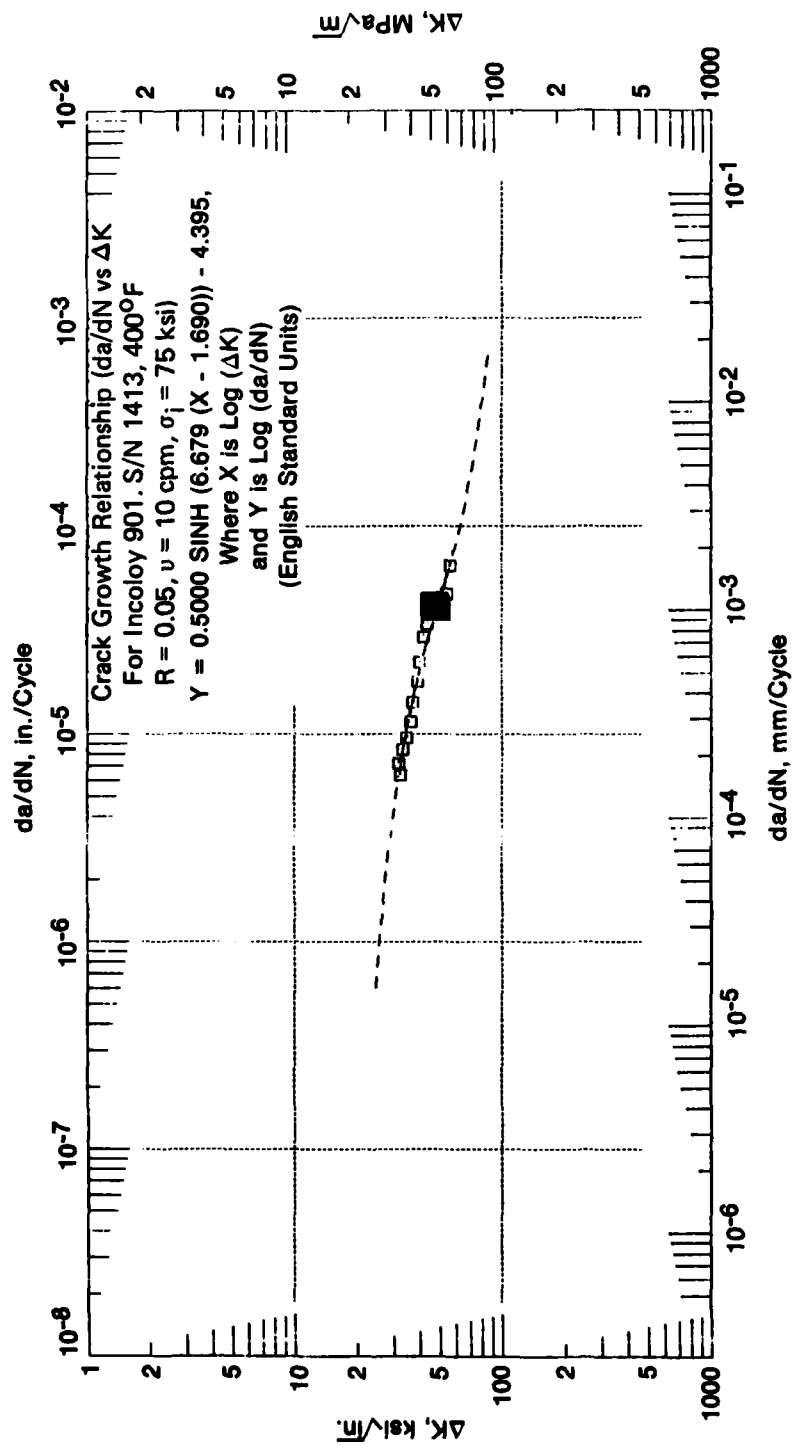
FD 175119

Figure 30. Crack Growth Relationship (da/dN vs ΔK) for Incoloy 901 S/N 1189



FD 175120

Figure 31. Crack Growth Relationship (da/dN vs ΔK) for Incoloy 901 S/N 1408



FD 175121

Figure 32. Crack Growth Relationship (da/dN vs ΔK) for Incoloy 901 S/N 1413

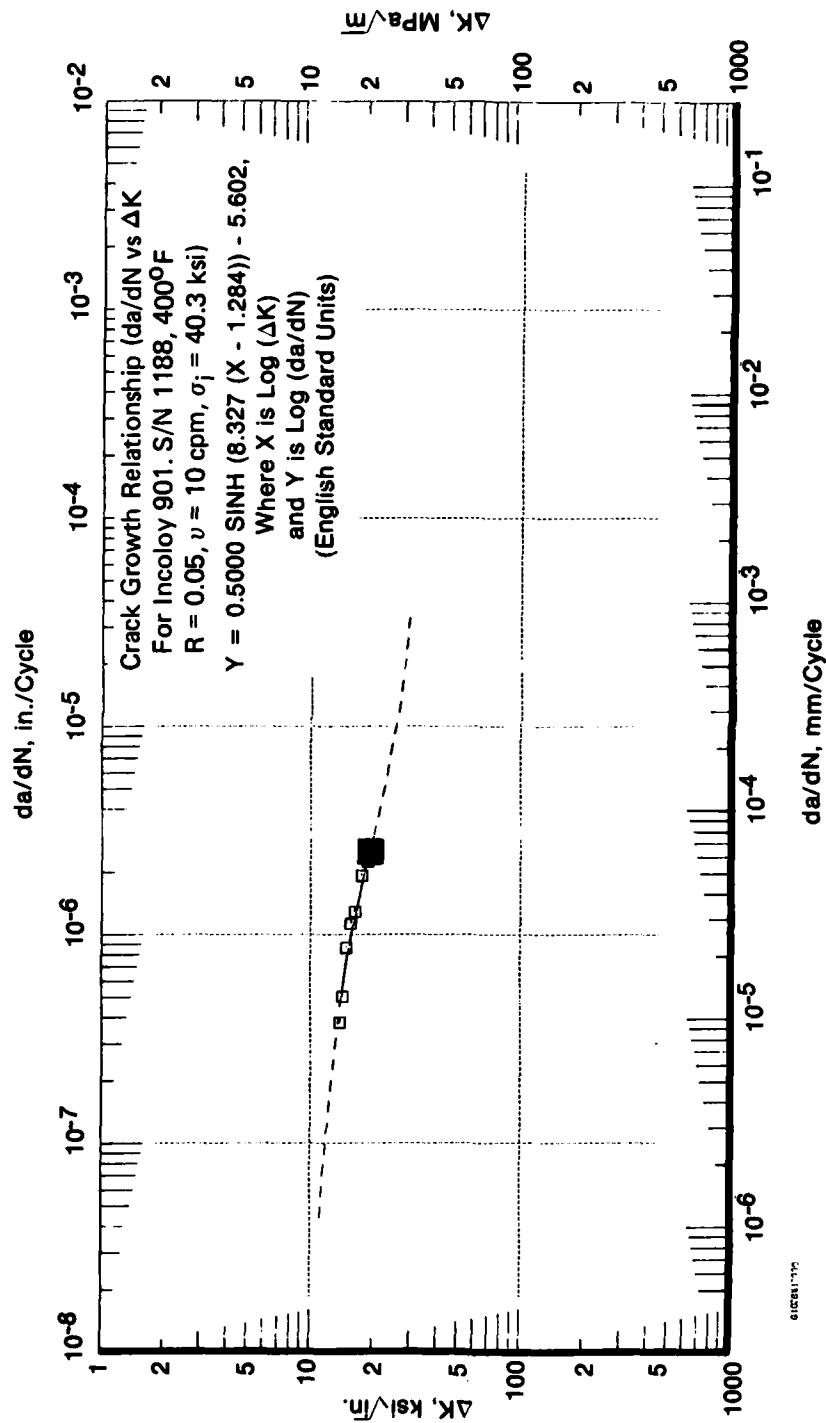
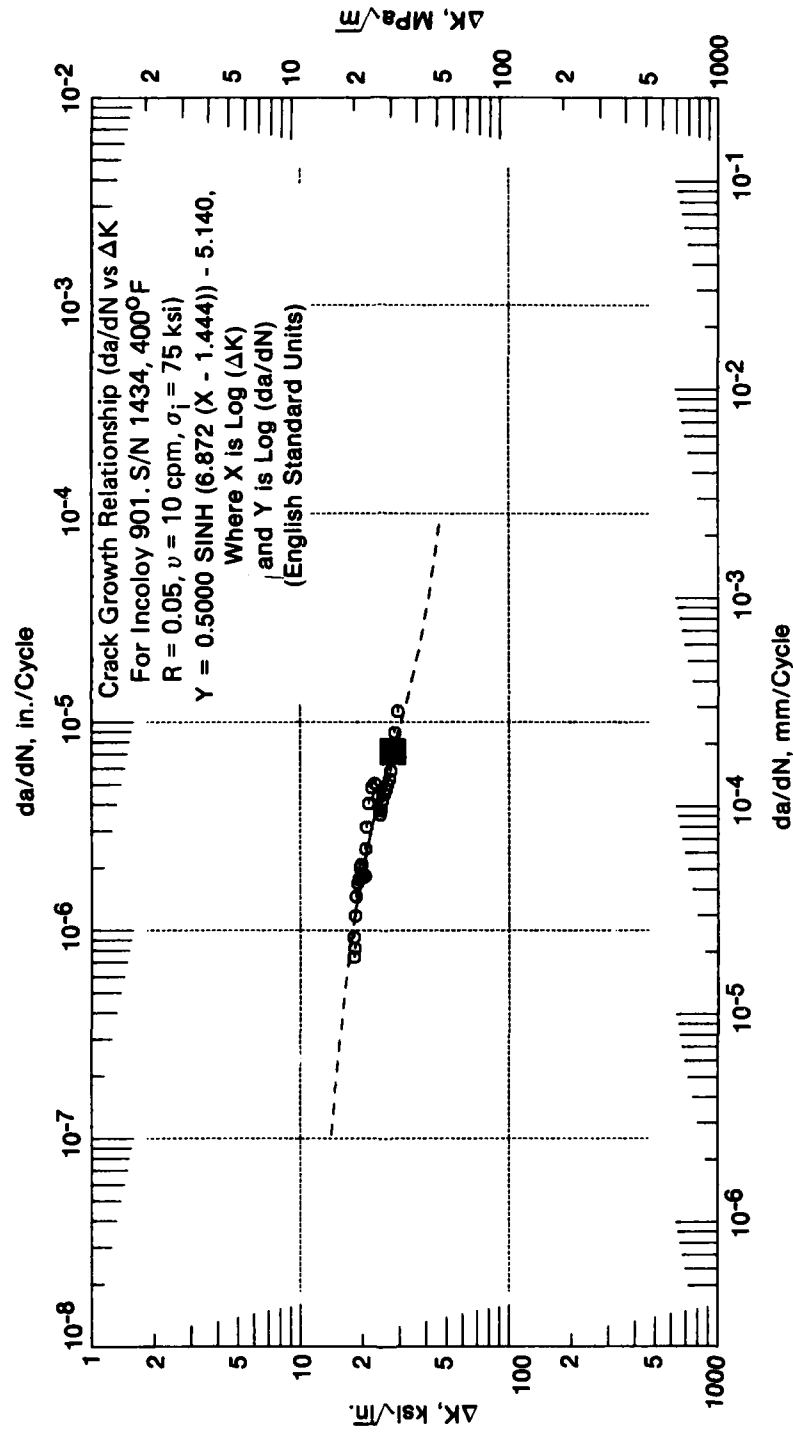


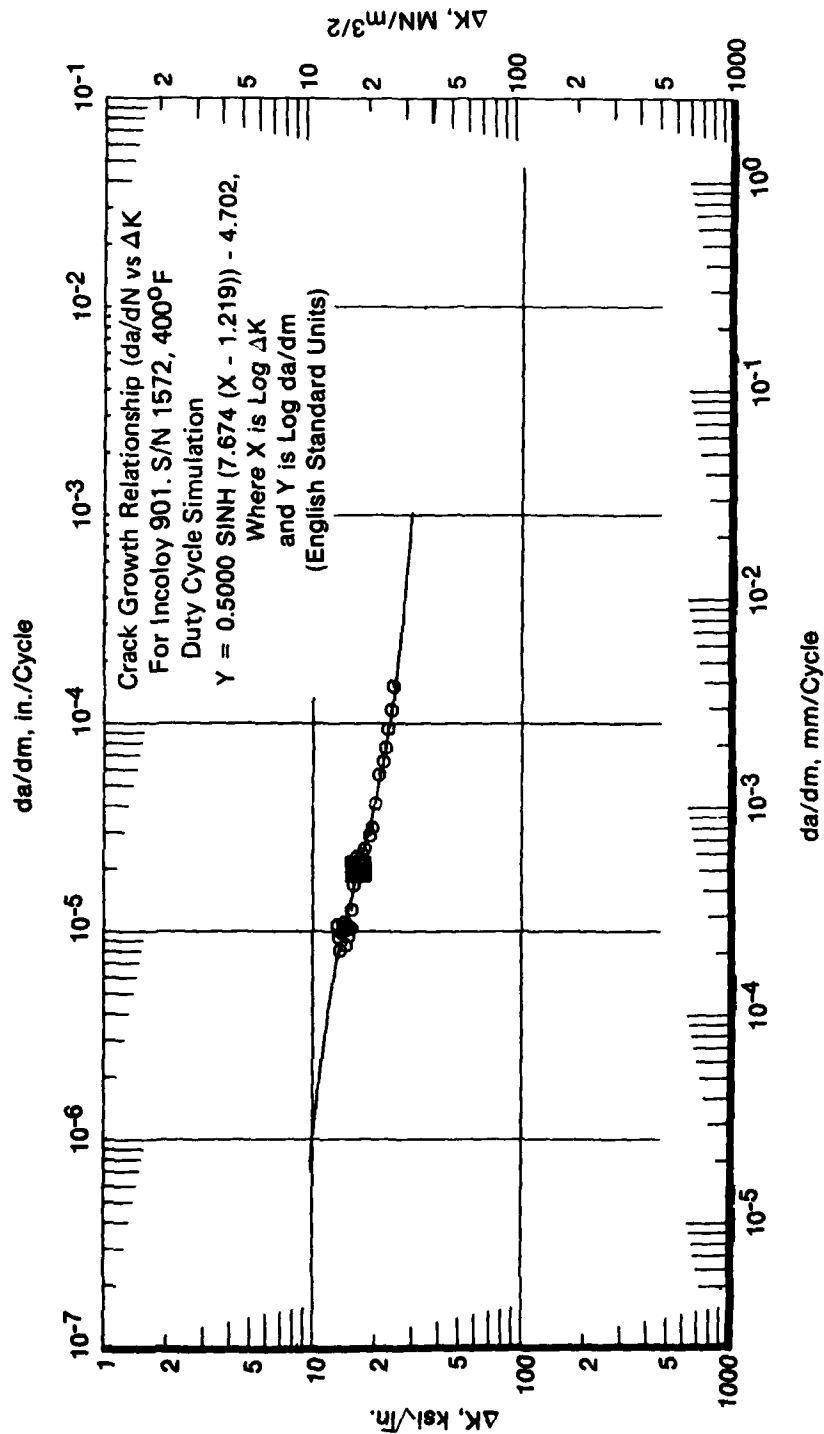
Figure 33. Crack Growth Relationship (da/dN vs ΔK) for Incoloy 901 S/N 1188

FD 175122



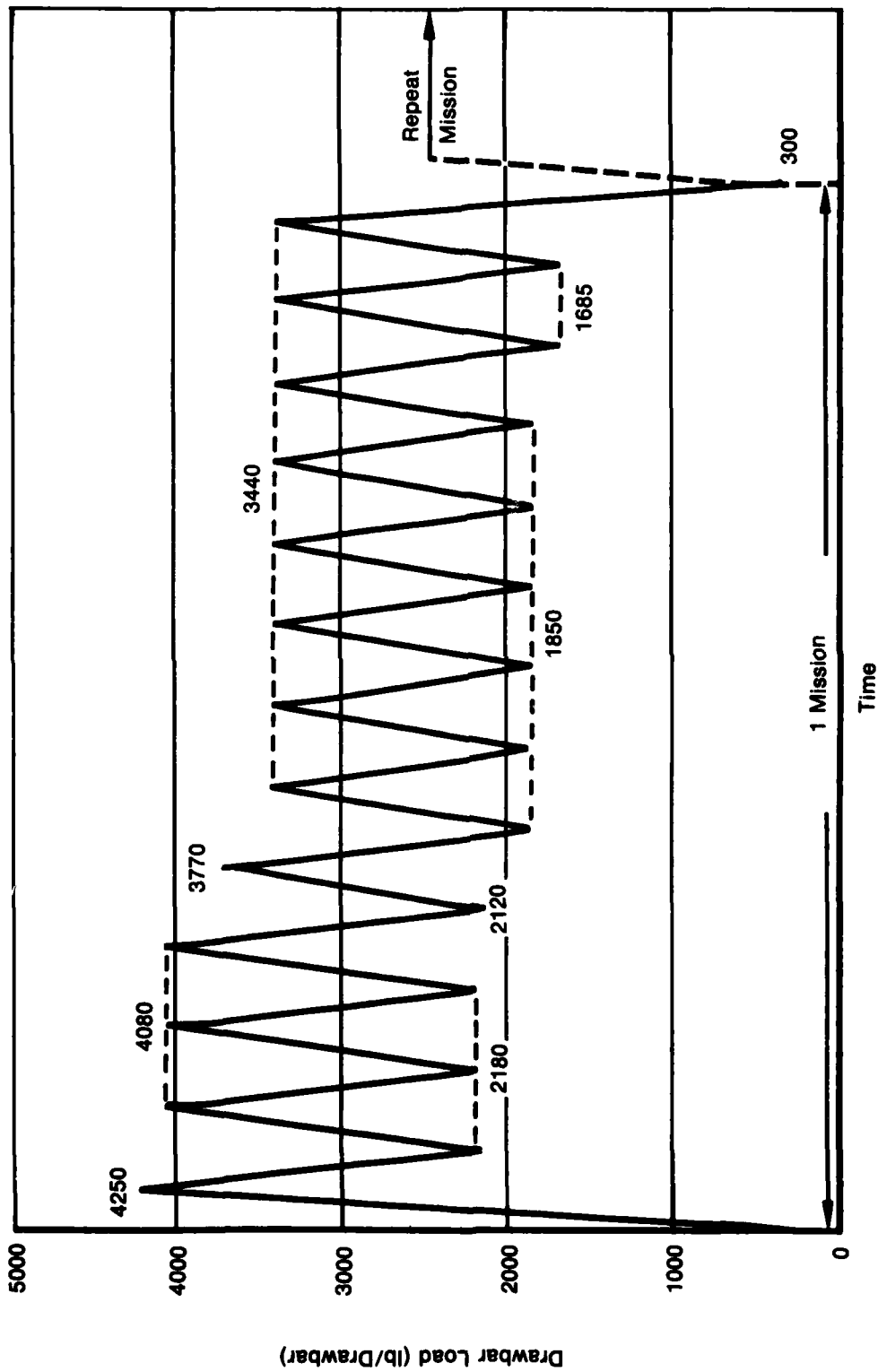
FD 175 123

Figure 34. Crack Growth Relationship (da/dN vs ΔK) for Incoloy 901 S/N 1434



FD 175124

Figure 35. Crack Growth Relationship (da/dN vs ΔK) for Incoloy 901 S/N 1572



FD 175125

Figure 36. TF30 10th-Stage Compressor Disk Ferris Wheel Duty Cycle Simulation

Heat tintings were also made during the ferris wheel testing. Disks were heated to 800°F and held at the temperature for an hour in air. After disks were fractured, fracture surfaces were examined under a stereomicroscope to measure the crack dimensions according to the marks of heat tinting.

The maximum stress distribution of the compressor disk bolthole (inboard side) at maximum load (4,250 lb) during the ferris wheel testing is presented in Figure 37. The figure includes results obtained from the strain gage survey, finite element analysis, and Bowie analysis (Reference 6). The indicated results from different methods were in good agreement, except at distances from the bolthole edge less than about 0.020 in. Stress remote from the bolthole was 68.75 ksi, determined from strain gage measurements.

In the vicinity of the bolthole edge, due to large scale yielding, analyses which did not consider plasticity resulted in unreasonably high stresses. This was the case for the Bowie analysis and elastic finite element analysis. Results of elastic-plastic finite element analysis were more reliable.

The through-thickness crack depths vs fatigue cycles for all disks tested are presented in Figures 38 and 39. Each crack depth presented was an average of crack depths at two faces of the disk and at the center of the crack front.

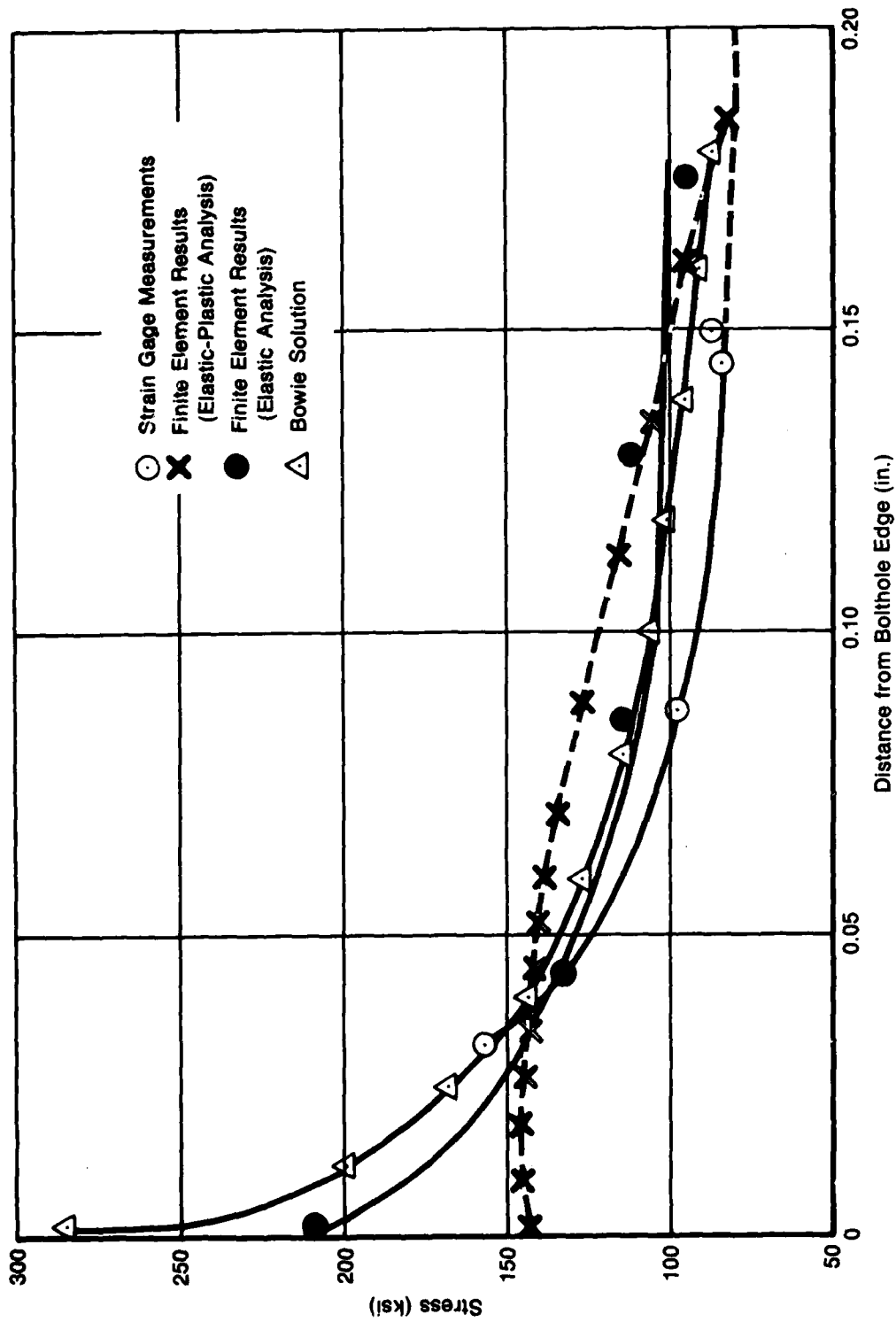
The crack depth at the center of each crack front was estimated using Figure 40. The values of a_{max} in Figure 40 were measured according to the heat tinted marks after disks were fractured. A summary of disk LCF lives is presented in Table 6.

NDE was conducted using the real time computerized AE technique and periodic EC, FP, and replication techniques described in Section II: Experimental Methods.

AE real time inspection was capable of detecting and source-locating relatively large active defects, but laboratory FPI (both stress-enhanced and static) and semi-automatic EC techniques were more sensitive indicators of bolthole fatigue cracks. While Incoloy 901 was shown to be a "good emitter" for AE inspection during specimen tests, two problems prevented optimum application of real time AE technique to the compressor disk program.

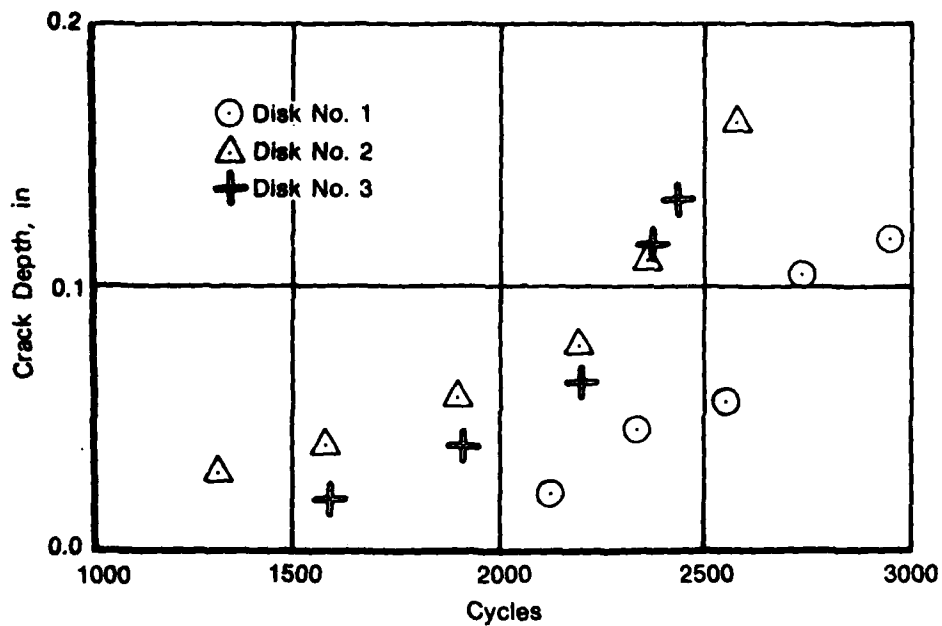
First, adaptation of the planar transducer array to the geometry of a turbine engine disk was difficult. As an interim fix, a "look-up chart" shown in Figure 41 was used to correlate computer X, Y coordinates with disk bolthole locations. A long-term fix, while not included within the scope of this program, is being developed through modification of the computer software to accommodate a turbine disk geometry. However, at least one vendor (Acoustic Emission Technology Corp, Sacramento) claims to now have a marketable, computerized system with a "calibrated array" capability which will allow inspection of complex geometries (such as an engine disk) with no special software modifications. Demonstration of this advanced system is being scheduled for the last half of 1979 at GPD.

Second, ambient mechanical noise during ferris wheel testing of the compressor disks was unusually high due to rub between the disk broach slots and drawbar ends. Various brush-on, anti-gall agents were applied (both Ag and MoS₂ based compounds), with the typical ambient AE record produced during a test increment appearing similar to Figure 42. Ambient AE remained low for a few fatigue cycles, but, as the coating was displaced, ambient AE always became high enough to effectively mask all desirable AE signals. As seen in Figure 42b, the ambient AE level is low only at the extremes of the cyclic loading curve. Therefore, there was a "window" for the first few entire cycles after recoating rub surfaces, and thereafter a "window" remained only at the very peak of each load cycle. Ambient noise encountered during the earlier ferris wheel testing of F100 1st-stage turbine disks was not as severe, but it was apparent from AE levels detected during specimen testing of Incoloy 901 that the smaller bolthole fatigue cracks would not be revealed during real time compressor disk inspection.



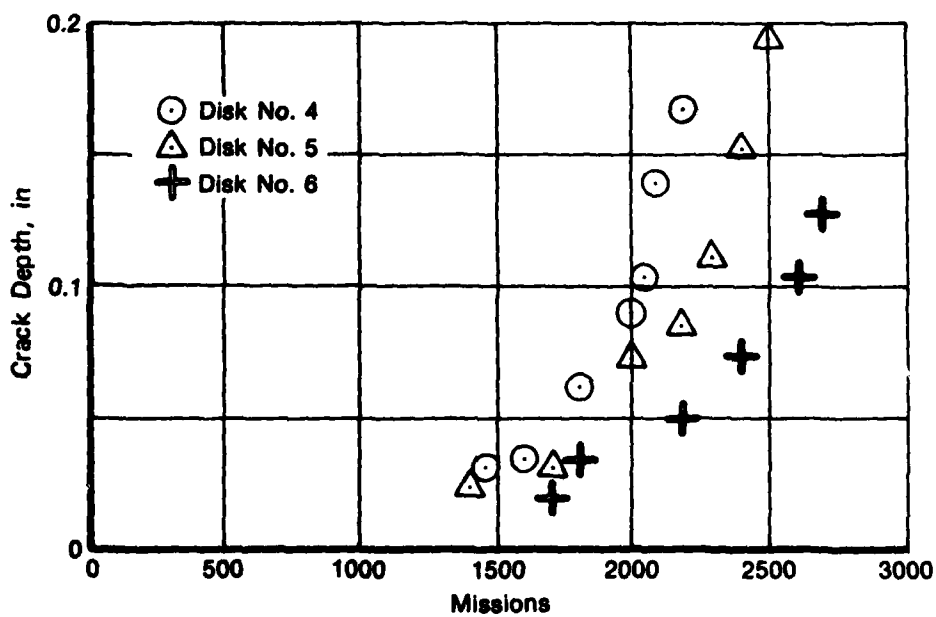
FD 175128

Figure 37. Stress Distribution of TF30 10th-Stage Compressor Disk Bolt Hole (Inboard, rear) at Maximum Load (4250 lb)



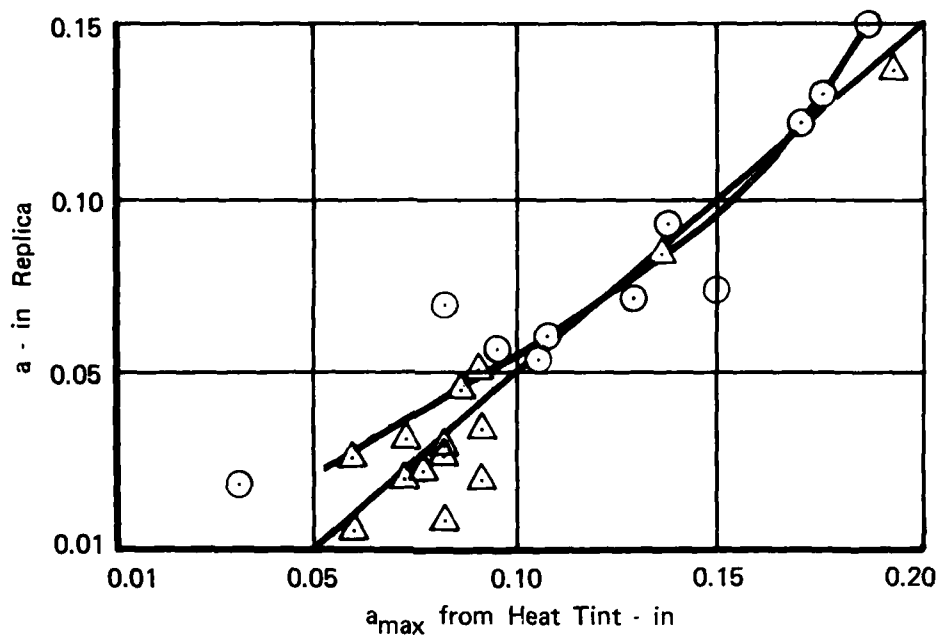
FD 175127

Figure 38. Crack Length vs Fatigue Cycles: Ferris Wheel Simple Sawtooth Cycle Testing



FD 175128

Figure 39. Crack Depth vs Fatigue Cycles: Ferris Wheel Mission Cycle Testing



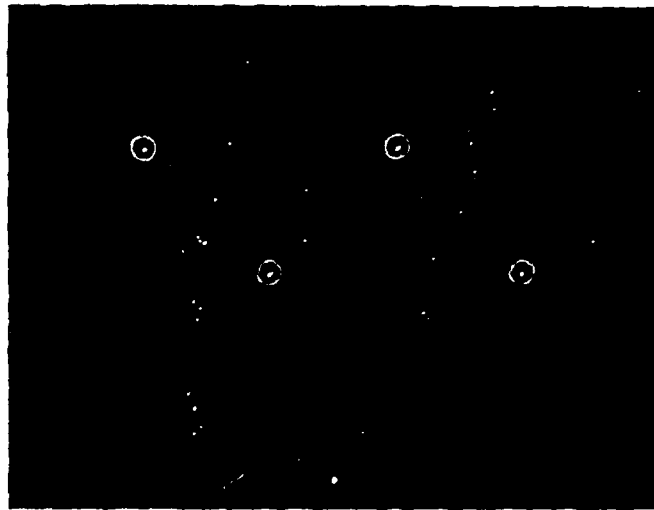
FD 175129

Figure 40. 10th-Stage Compressor Disk Replica Measurements vs Heat Tint

TABLE 6. SUMMARY OF DISK LCF LIVES

Disk S/N	Testing Order	First Indication	*1/32-in. Crack	Cycles to Fracture
G82568	1	1500 cycles	1275 cycles	3169
G24399	2	1000 cycles	1150 cycles	2656
G82564	3	800 cycles	1050 cycles	2492
G82589	4	800 cycles	1300 cycles	1300 sawtooth + 932 missions
G82573	5	800 cycles	900 cycles	1100 sawtooth + 1463 missions
G82577	6	800 cycles	1100 cycles	1300 sawtooth + 1465 missions

*Periodic inspections conducted at 100 to 300 cycle intervals.



CRT Display of Disk Calibration

○ Sensors
Indications

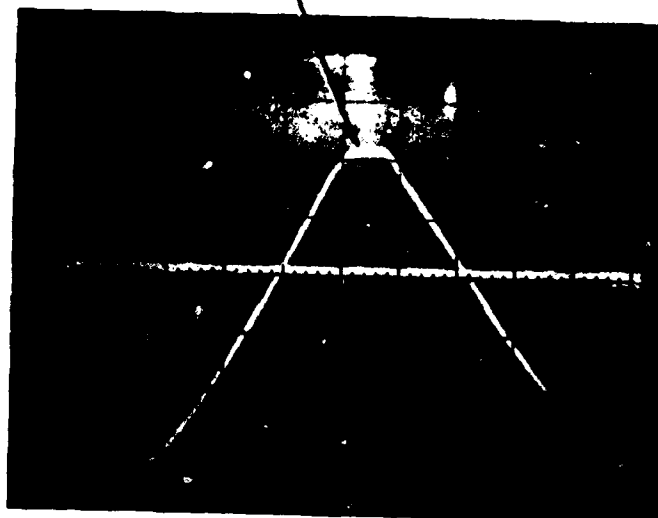
Bolthole No.	Computer Coordinates	
	X	Y
1	-7.1	3.4
2	-6.5	7.4
3	-7.7	20.3
4	7.3	54.2
5	9.9	14.1
6	9.6	6.9
7	9.2	2.2
8	8.5	-0.9
9	7.5	-4.8
10	6.3	-10.6
11	8.1	-31.6
12	-11.9	-22.5
13	-11.1	-8.4
14	-9.7	-4.8
15	-9.9	-2.7
16	-9.0	0.1

FD 175130

Figure 41. Compressor Disk Calibration for Computerized Acoustic Emission Inspection

AE Signal Level

Cyclic Load

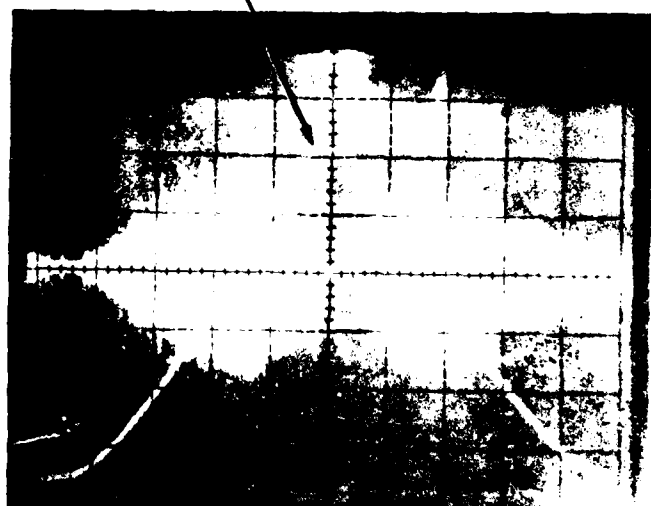


Time

(a) Beginning of Test Interval
(Ambient AE Level Low)

AE Signal Level

Cyclic Load



Time

(b) Beginning of Test Interval, Plus 20 Fatigue Cycles
(Ambient AE Level Masks Desirable Signals)

Figure 42. Ferris Wheel Test of TF30 10th-Stage Compressor Disk: Cyclic Load and Acoustic Emission Signal Level

FD 175131

In addition to the brush-on, anti-gall coatings mentioned above, electroplated Ag was explored as a possible solution. The coating did last longer than the previous brush-on coatings (over a hundred fatigue cycles), but it was eventually displaced. Replating of the drawbars was too expensive and time consuming to consider periodic silver plating as a long term fix.

Communications with Dr. Tali Spalvins at NASA/Lewis resulted in a new approach to the problem late in the disk program. Dr. Spalvins, a recognized expert in tribology, indicated that MoS_2 was probably the optimum coating for our application, but a brush-on, air-cured form would not adhere properly. He suggested that a sputtered MoS_2 coating would provide the required anti-gall characteristics, if applied to a 0.5 micron thickness, and the coating would bond well enough to the INCO 718 drawbars to endure thousands of fatigue cycles. Dr. Spalvins also suggested that if electroplating of Ag to the drawbar ends with partially successful, ionization plating of Ag would endure for many more fatigue cycles.

As a result, several ferris wheel drawbars were sent to a vendor (Hohman Plating, Dayton, Ohio) for application of a sputtered MoS_2 coating to rub surfaces. By the time the plating operation was completed and the drawbars were returned, the disk fatigue testing program was finished. However, a fixture has been designed to evaluate the coating in a standard hydraulic test machine. This evaluation, using real time AE inspection to detect wear of the coating, will be performed later this year.

AE inspection was performed during the elevated temperature disk tests using high temperature sensors (D/E Model 9205M2) coupled directly to the disk. Teflon sheeting was used as a couplant, and the sensors were held in place with clamps. Total system gain was maintained at 90 dB.

Calibration of the array was performed at room temperature by stimulating the disk adjacent to each bolthole with a pulsing transducer (D/E Model S140) and recording the X and Y coordinate values which were produced by the computer to correspond to each bolt hole. A calibration is shown as Figure 41. Using the "look-up chart" it was possible to relate AE indications, as interpreted by the computer, to actual disk locations.

Figure 43 illustrates the AE record for compressor disk S/N G82568, test cycles 1923-2123. The results of a periodic inspection are listed in Table 7. It is apparent, through cross-reference to Figure 41, that the AE indications occurred in the vicinity of bolthole No. 13, the most severely cracked hole. But additional smaller cracks, such as the crack in No. 2, were not indicated. A post-test analysis of the results provided at least a partial explanation. Figure 44 shows a plot of AE events (Y-axis) vs cyclic load (X-axis) for this test period. Most AE indications appear close to the opening of the voltage controlled gate and no indications appear at higher load levels. This is because the AE system became "flooded" with data shortly after it opened and allowed the computer to begin processing data. As a result the most desirable AE signals were not registered and processed.



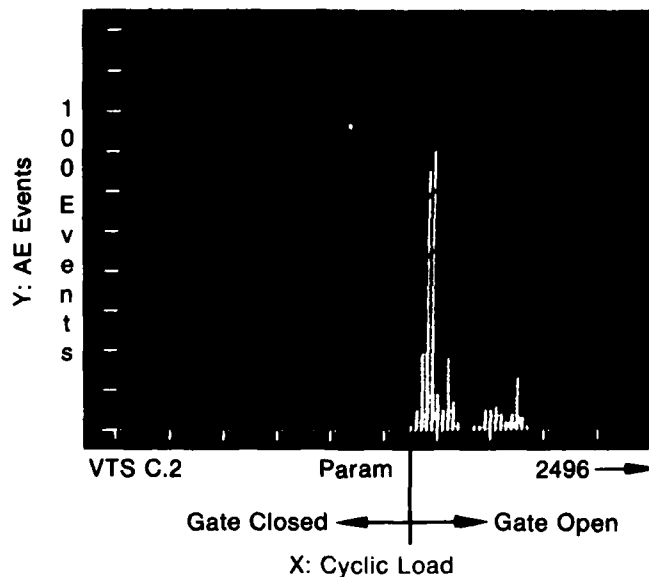
⊙ Sensors
Indications

FD 175132

*Figure 43. AE Source Location Record for Compressor Disk S/N G82568,
Test Cycles 1923-2123*

TABLE 7
COMPRESSOR DISK S/N
G82568 REPLICATION
RESULTS AFTER 1923-CYCLE
INSPECTION

<i>Bolthole No.</i>	<i>Crack Length (in.)</i>
1	—
2	0.090
3	0.040
4	0.120
5	—
6	—
7	—
8	—
9	0.025
10	—
11	0.075
12	0.130
13	0.250 (through-crack)
14	—
15	0.080
16	—



FD 175133

Figure 44. Post-Test Analysis of AE Events vs Cyclic Load

After an initial 800 fatigue cycles were applied to each disk, periodic inspections were performed in intervals of approximately 200 cycles. Periodic NDE included semi-automatic EC, stress-enhanced FPI, laboratory static FPI, and production-type FPI. Flaw indications were documented via replications. Photographs were taken of most replica records.

The large amount of inspection data generated during the compressor disk program made an excellent data base for generation of reliability statistics. Replication under load was used to verify crack indications and to measure crack sizes. Stress-enhanced FPI, EC, and production-type FPI were used as inspection techniques during the crack initiation phase of the program. Laboratory static FPI was used only on a limited basis during the crack initiation phase because static FPI was considered less sensitive and reliable for small (less than 1/32-in. length) flaws. Static FPI and/or stress-enhanced FPI was used as the inspection technique during the crack propagation phase of the testing. The EC and production-type FPI were used only on a limited basis during the propagation phase. These inspections were discontinued during the crack propagation study because of the long time required to take each disk out of the ferris wheel for inspection. Also, EC indications tended to saturate during the propagation stage and did not provide additional information about the flaws. All the inspections were conducted in a random sequence by a random selection of inspectors each time. The critical location of the disk (Tie-rod bolthole) was indicated to the inspectors.

Crack lengths determined by replication were evaluated against the inspection techniques used. For each inspection technique, total number of flaws and number of flaws detected were computed for each of the following flaw size ranges:

1. 0.003 to 0.016 in.
2. 0.017 to 0.032 in.
3. 0.033 to 0.100 in.
4. 0.101 to 0.258 in.

Inspection results and associated reliability figures are presented in Tables 6 through 12 of Section III: Test Results.

TABLE 8
RELIABILITY OF STRESS-ENHANCED FPI
FOR INSPECTION OF TF30 10th-STAGE
COMPRESSOR DISK BOLTHOLES

<i>Flaw Length Ranges Inches (mm)</i>	<i>Number of Flaws</i>	<i>Number of Flaws Detected</i>	% Probability Detection Confidence		
			90%	95%	99%
0.003-0.016 (0.076-0.406)	192	181	92.2	91.5	90.0
0.017-0.032 (0.432-0.813)	65	65	96.5	95.5	93.2
0.033-0.100 (0.838-2.540)	71	71	98.3	97.8	96.7
0.101-0.258 (2.565-6.553)	74	74	98.9	98.6	97.8

TABLE 9
RELIABILITY OF EDDY-CURRENT
FOR INSPECTION OF TF30 10th-STAGE
COMPRESSOR DISK BOLTHOLES

<i>Flaw Length Ranges Inches (mm)</i>	<i>Number of Flaws</i>	<i>Number of Flaws Detected</i>	% Probability Detection Confidence		
			90%	95%	99%
0.003-0.016 (0.076-0.406)	89	86	92.7	91.7	89.5
0.017-0.032 (0.432-0.813)	40	40	94.4	92.8	89.1
0.033-0.100 (0.838-2.540)	36	36	97.0	96.1	94.1
0.101-0.258 (2.565-6.553)	60	60	98.3	97.8	96.7

TABLE 10
RELIABILITY OF LABORATORY STATIC FPI
FOR INSPECTION OF TF30 10th-STAGE
COMPRESSOR DISK BOLTHOLES

<i>Flaw Length Ranges Inches (mm)</i>	<i>Number of Flaws</i>	<i>Number of Flaws Detected</i>	<i>% Probability Detection Confidence</i>		
			90%	95%	99%
0.003-0.016 (0.076-0.406)	175	128	69.0	67.7	65.7
0.017-0.032 (0.432-0.813)	85	84	95.5	94.6	92.5
0.033-0.100 (0.838-2.540)	111	111	98.0	97.3	95.9
0.101-0.258 (2.565-6.553)	150	150	99.1	98.9	98.3

TABLE 11
RELIABILITY OF PRODUCTION-TYPE FPI
FOR INSPECTION OF TF30 10th-STAGE
COMPRESSOR DISK BOLTHOLES

<i>Flaw Length Ranges Inches (mm)</i>	<i>Number of Flaws</i>	<i>Number of Flaws Detected</i>	<i>% Probability Detection Confidence</i>		
			90%	95%	99%
0.003-0.016 (0.076-0.406)	89	0	0	0	0
0.017-0.032 (0.432-0.813)	40	0	0	0	0
0.033-0.100 (0.838-2.540)	36	6	9.0	7.5	5.2
0.101-0.258 (2.565-6.553)	60	45	66.1	63.7	59.1

TABLE 12
SUMMARY OF NDT RELIABILITY FOR TF30 10th-STAGE
COMPRESSOR DISK BOLTHOLES

Flaw Length Ranges Inches (mm)	% Probability of Detection 95% Confidence			
	Eddy-Current	Stress Enhanced FPI	Lab Static FPI	Production Type FPI
0.003-0.016 (0.076-0.406)	91.7	91.5	67.7	0
0.017-0.032 (0.432-0.813)	92.8	95.5	94.6	0
0.033-0.100 (0.838-2.540)	96.1	97.8	97.3	7.5
0.101-0.258 (2.565-6.553)	97.8	98.6	98.9	63.7

For each flaw size range, probability of detection (POD) at confidence levels of 90, 95, and 99% was computed (see Appendix). Exact binomial distribution was used to compute the lower bound POD. If no flaw was missed in one flaw size range, then the flaws in that flaw size range were included for computing POD for the next higher flaw size, and so on. This is justified because it is conservative to estimate POD of a larger flaw size range from a smaller flaw size range and this procedure provides a better estimate of the POD by increasing the sample size (Reference 7 and 8.)

Obviously, the flaws from a smaller flaw size range were not included to estimate POD of a larger flaw size range if any flaws were missed for the small flaw size range. This would have reduced POD of the larger flaw size range because of the lower detectability of the smaller flaw size range. Recently there has been a lot of debate as to what should be the best method of estimating POD. At present there are no clear answers to this complex problem. But the problem has been addressed in some recent work (References 9, 10). A convenient format for POD curve evaluation is either a histogram or curve of POD relative to flaw size (Figure 45, 46). Additionally, performance evaluation can be conducted using tests for significance of variables. The significance test answers the question of whether observed differences in POD among different combinations of variables can be attributed to those variables.

The choice between histograms or analytical curves of POD is usually based on sample size. If only limited data is available or the sample size is small, grouping of data using histograms is usually preferred. The advantage of the histogram method is that it is simple, easy to use and understand. The main disadvantage is that it is difficult to assess variability or scatter in the POD.

Analytical Methods

Analytical expressions to relate mean POD to crack size can be used, and a lower-bound confidence curve can be estimated, e.g.,

$$POD = 1 - 10^{-(\text{crack size}/0.01)^{0.637}}$$

(see figure 46).

The above example reduces to the generic form described in Reference 9:

$$y = a(x)^b$$

The advantages of the analytical methods are that it provides a more usable POD vs flaw size relationship, and permits quantification of variability of data about the mean POD expression.

The disadvantage of this method is that application of calculated variance depends on the assumed type of distribution.

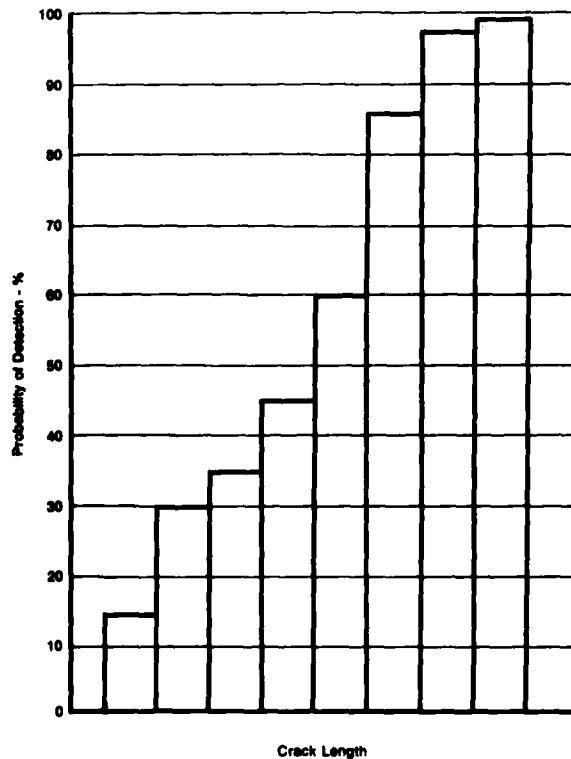
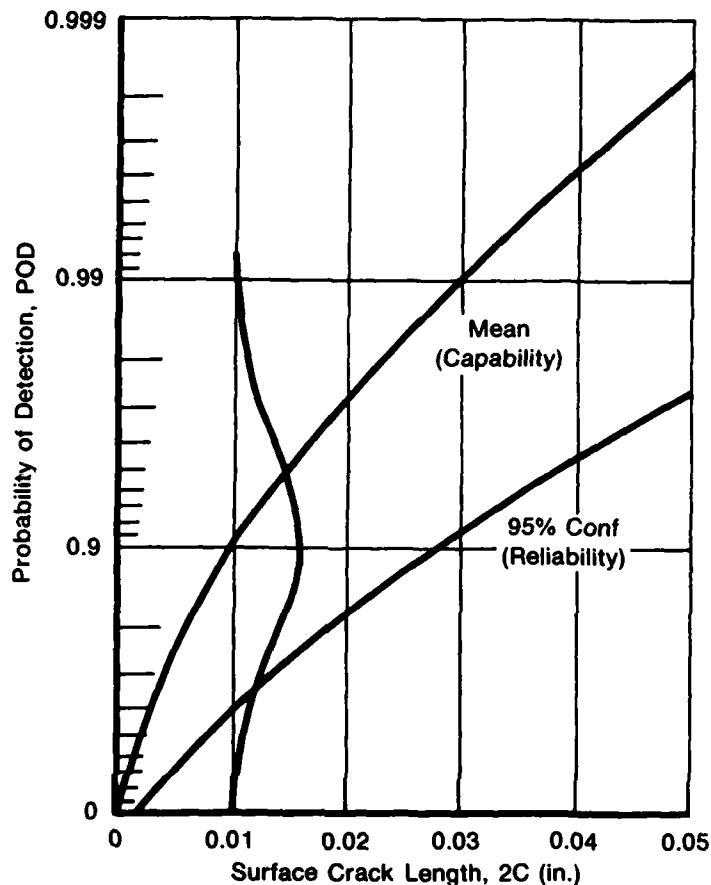


Figure 45. Schematic — Lower Bound Probability of Detection vs Crack Length (Plotted by Equal-Flaw-Size-Interval Method)



FD 102950

Figure 46. Schematic of POD Curve Based on an Analytical Expression of the Form $y = a(x)^b$

Reference 9 (SAALC/MME 76-6-38-1) assumes Gaussian (normal) distribution. The resulting POD computations are straightforward, but the assumption of symmetrical distribution is not realistic, particularly when POD approaches zero or unity.

P&WA is currently developing other analytical methods for the retirement-for-cause (RFC) methodology development. These methods include lognormal distribution and Beta-distribution (Reference 10). For the purpose of 10th compressor NDE-reliability statistics a simple histogram procedure was chosen.

It is apparent from a cursory look at Tables 7 through 12 that a large number of cracked boltholes were inspected using each technique. Replication under load was an effective documentary tool for each of the inspections.

Table 12 compares reliability of each of the periodic inspection techniques at 95% confidence. The most obvious conclusion which may be made from Table 12 is that laboratory NDE is much more effective for detection of fatigue cracks less than 0.100 in. length than standard production-type FPI. Table 12 also indicates that stress-enhanced laboratory FPI was noticeably more effective than static laboratory FPI only for the smallest flaw size range (0.003 in. to 0.016 in. length). That is probably because larger flaws were not as tightly closed and the Z1 35 ultra-high sensitivity penetrant required relatively low penetration into the fatigue cracks to make them visible to laboratory technicians.

The implication of the NDE reliability results is that RFC NDE could be performed for many engine components using techniques, but standard production-type FPI would suffice for only a limited number of components.

The primary purpose for development of these reliability statistics was to demonstrate that obtainment of the NDE reliability levels necessary to implement RFC inspections is obtainable using the basic existing NDE tools. In other words, the generic capabilities of eddy current and specialized FPI are sufficient to produce sensitive, reliable results. However, in order to produce high-reliability inspections for small fatigue cracks in an overhaul environment, a great deal of technology development will be required (as demonstrated by results from production-type inspections.)

COMPRESSOR DISK LIFE ANALYSIS

The stress intensity factor near the bolthole was estimated using three different approaches:

Bowie analysis

The Bowie analysis states:

$$K = \sigma \sqrt{\pi a} f(a/D) \quad (4)$$

where:

- σ = applied normal stress
- a = distance from the edge of the circular hole
- D = diameter of the circular hole
- $f(a/D)$ = a function of a/D

Deep Through-Thickness Crack Approach

For a deep through-thickness crack, the stress concentration due to the hole diminishes and the hole and crack combination may be assumed to be the effective crack length. Stress intensity under this assumption is estimated to be

$$K = \sigma \sqrt{\pi(D+a/2)} \quad (5)$$

Experimental "Effective K" Approach

Based on experimental results, such as Figure 38, estimations of K vs a could be obtained. Using the sinh equation in Figure 30 and the data in Figure 38, a series of K_{max} vs a data were obtained. These K_{max} vs a data were least square fitted and the equation was

$$K_{max} = 73.054(a) + 50.738 \quad (6)$$

Plots of equations 4, 5, and 6 are presented in Figure 47. The results of equation 5, were nearly parallel to those of equation 6 with about 10% difference. Bowie analysis (equation 4) gives conservative K values with respect to equation 6 at a less than 0.040 in. However, at a larger than 0.040 in., K values obtained from Bowie analysis were anti-conservative.

Disk residual life analyses were accomplished using fracture mechanics concepts. Analyses were performed for both simple sawtooth cycles and duty cycles. The disk life was separated into two stages: initiation and propagation.

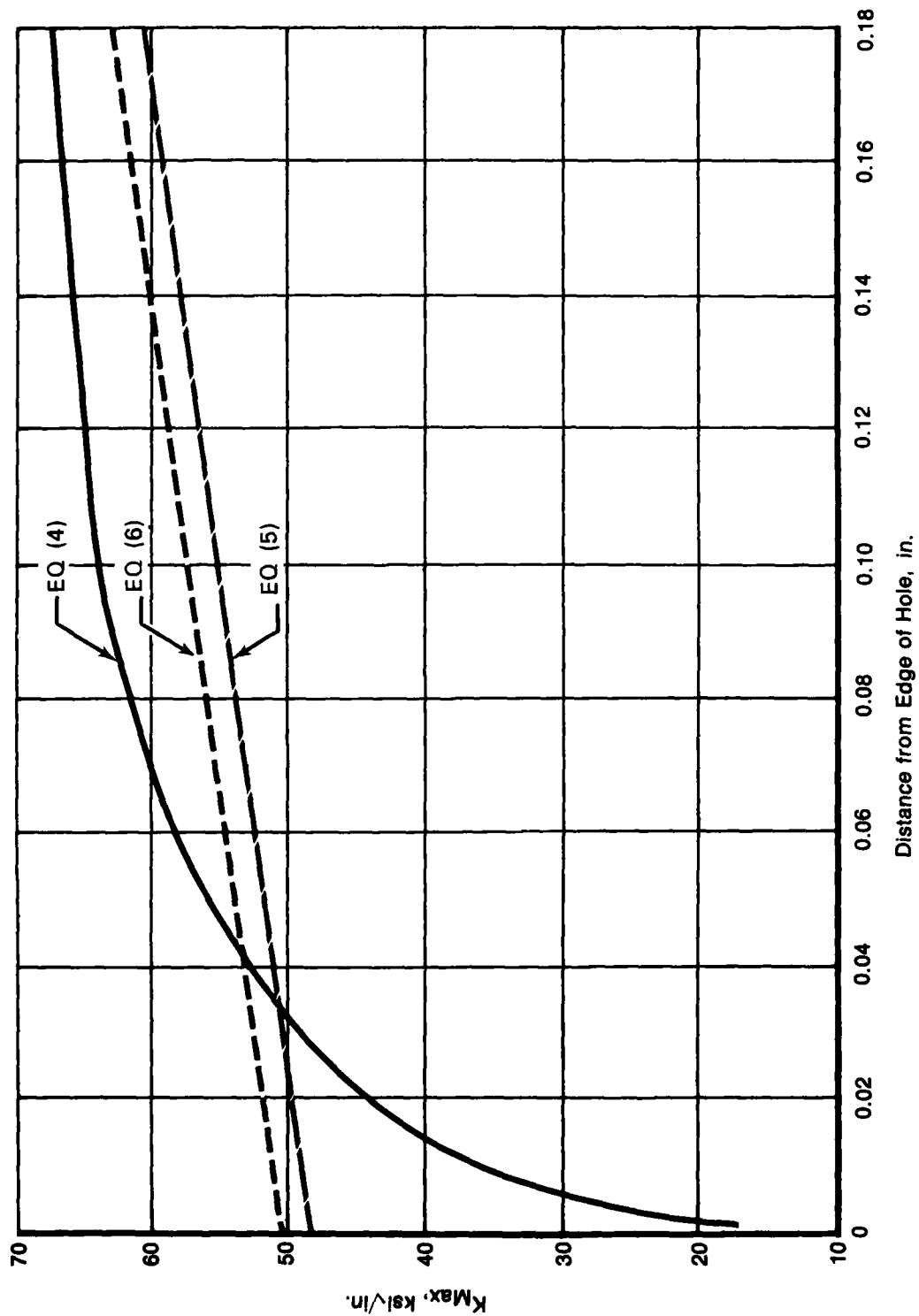


Figure 47. K_{max} vs a for Compressor Disk Bolt Holes

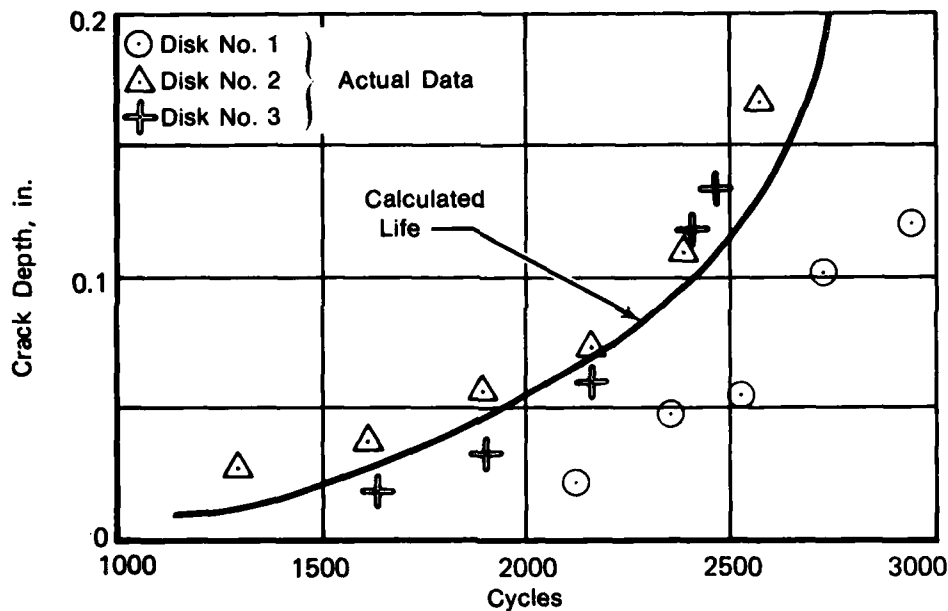
FD 175134

The fatigue initiation life was considered to be fatigue life up to a 1/32-in. surface crack in any bolthole. The average initiation life was 1129 cycles under simple sawtooth cycle testing, which was the only type of testing conducted during the initiation period.

Fatigue life from a 1/32-in. crack to fracture was considered to be propagation life. This is the prime interest of the present study, and the following presentations are the results of this study.

Suitable K solution and da/dN vs ΔK information are necessary for fatigue fracture mechanics analysis. All the K -solutions presented in the previous section were studied for purposes of comparison. Various suitable da/dN vs ΔK relationships were used.

The da/dN vs ΔK relationship in Figure 30 was used for the simple sawtooth cycle analyses. Figure 48 is a plot of the results using equation 6 (Effective K Approach). Actual data are also presented in the figure.



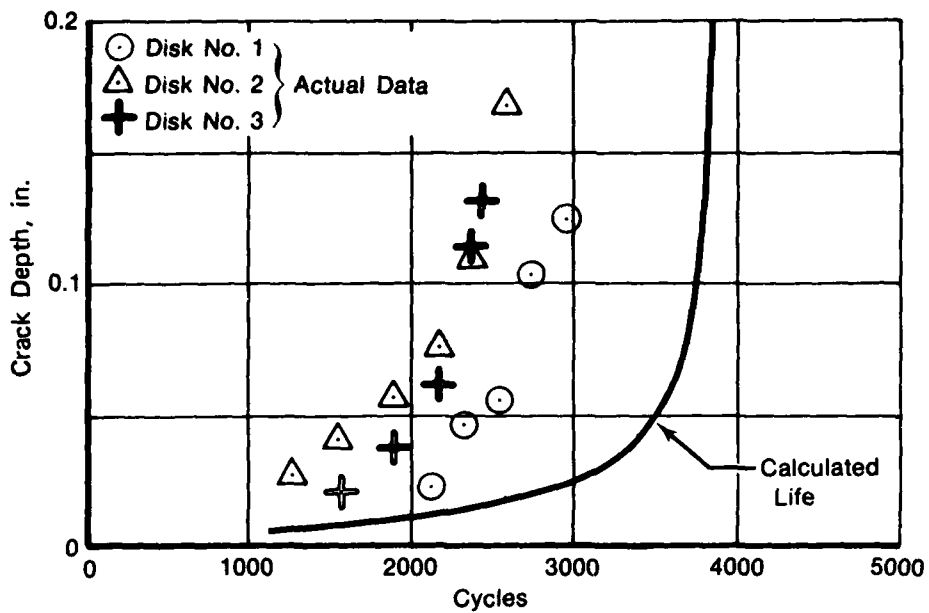
FD 175135

Figure 48. Bolthole Crack Depth vs Cycles: Life Analysis of Simple Sawtooth Cycle, Effective K Approach

The life calculated was in good agreement with the actual data. This should be the case because the K -solution was obtained from the actual data during disk ferris wheel testing.

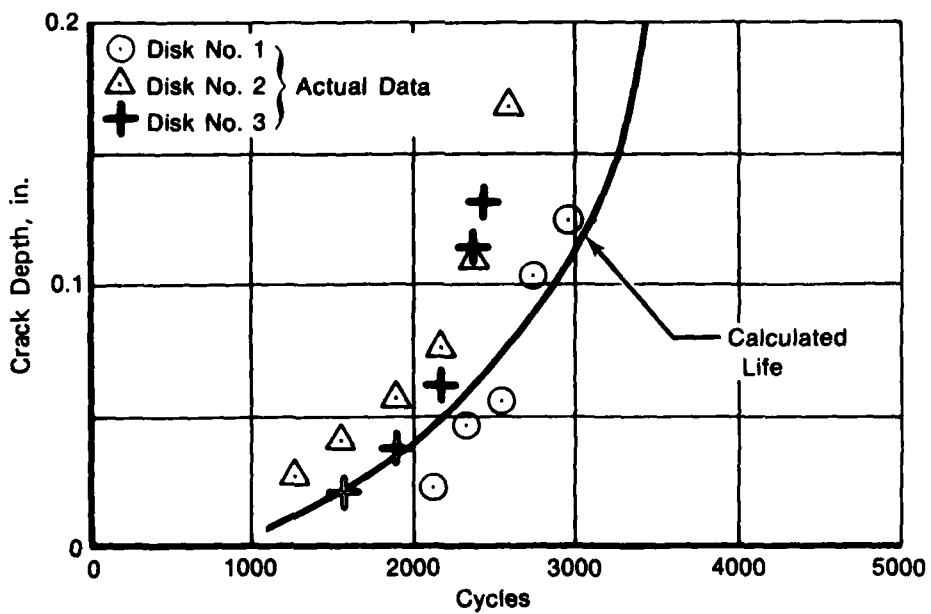
Fatigue life calculated from equation 4 (Bowie analysis) was anti-conservative, as shown in Figure 49. At distances less than 0.040 in., the K values were much lower than those of the experimental approach. Lower values of K gave a longer life, as indicated in the figure.

Figure 50 shows the results of using equation 5 (deep through-thickness crack) against the actual data. The model slightly overestimated the fatigue life.



FD 175136

Figure 49. Bolthole Crack Depth vs Cycles: Life Analysis of Simple Sawtooth Cycle, Bowie Analysis



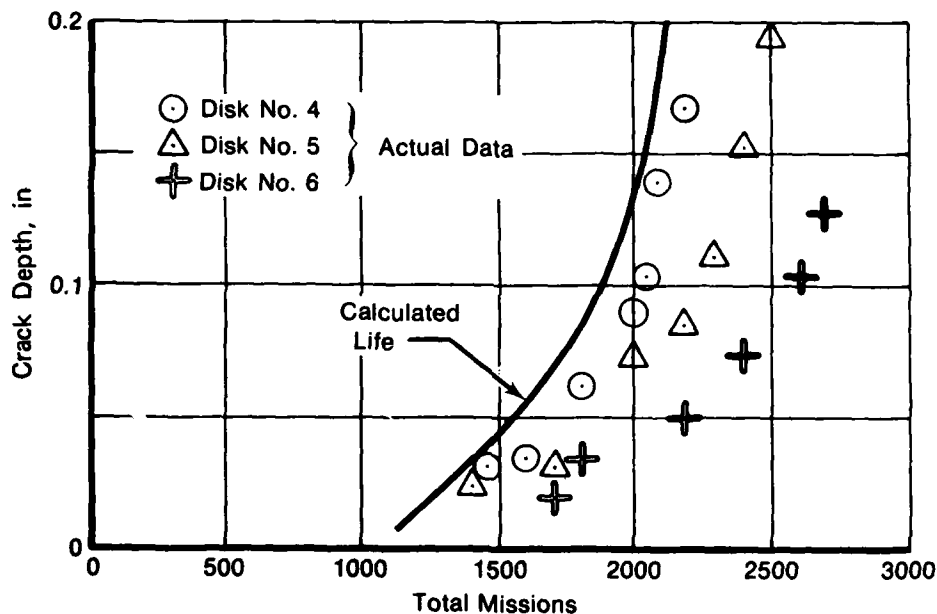
FD 175137

Figure 50. Bolthole Crack Depth vs Cycles: Life Analysis of Simple Sawtooth Cycle, Deep Through-Thickness Crack Approach

Two analyses were performed for the duty cycle modeling: modeling without synergistic effects and modeling with synergistic effects. The assumptions for the non-synergistic effects modeling were as follows:

- The first sub-cycle (Figure 36) was modeled with $R = 0.05$. The sinh coefficients used were in Figure 30.
- The rest of the sub-cycles were modeled with $R = 0.5$. The sinh coefficients used were in Figure 33.
- No interactions among sub-cycles took place.

Results of using the experimental effective K approach shown in Figure 51 indicated that the model underestimated the fatigue life. Because of the lack of agreement between the experimental effective K approach and the actual data, the analyses using the Bowie solution and the deep through-thickness crack approach were not pursued.

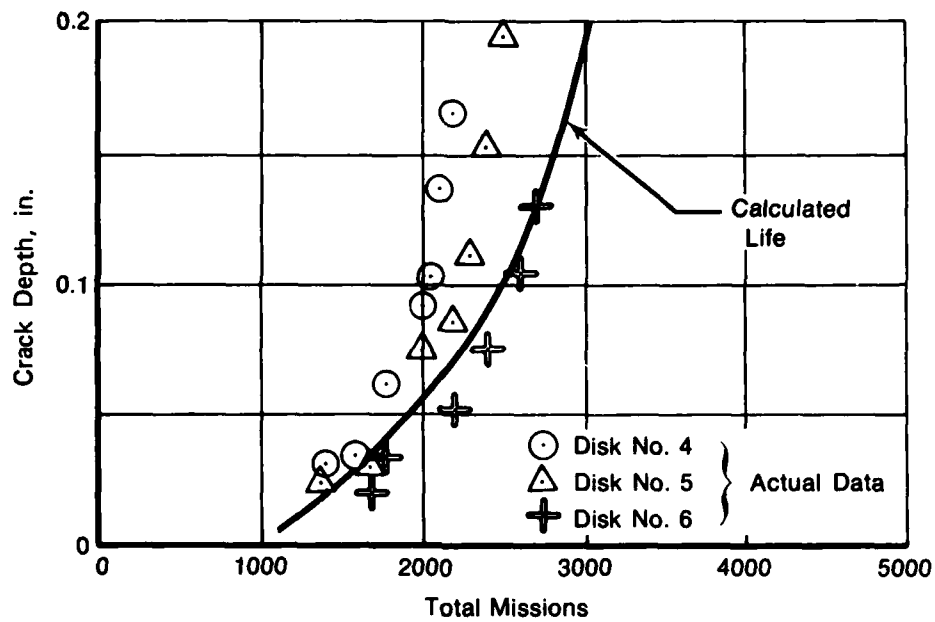


FD 175138

Figure 51. Bolthole Crack Depth vs Missions: Life Analysis of Duty Cycle, Experimental Effective K Approach with Non-Synergistic Effects

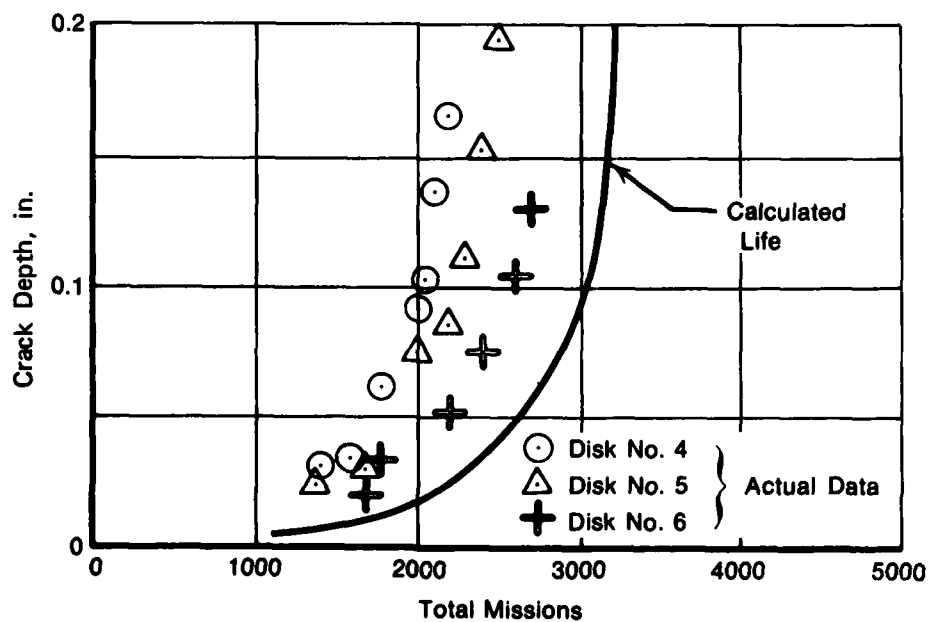
The relationship of da/dN vs ΔK in Figure 35 was used in synergistic effects modeling. Results using the experimental effective K approach shown in Figure 52 indicated that the calculated life is in good agreement with the actual data.

Figures 53 and 54 show the results of using the Bowie analysis and the deep through-thickness crack approach, respectively. Both approaches overestimated disk life.



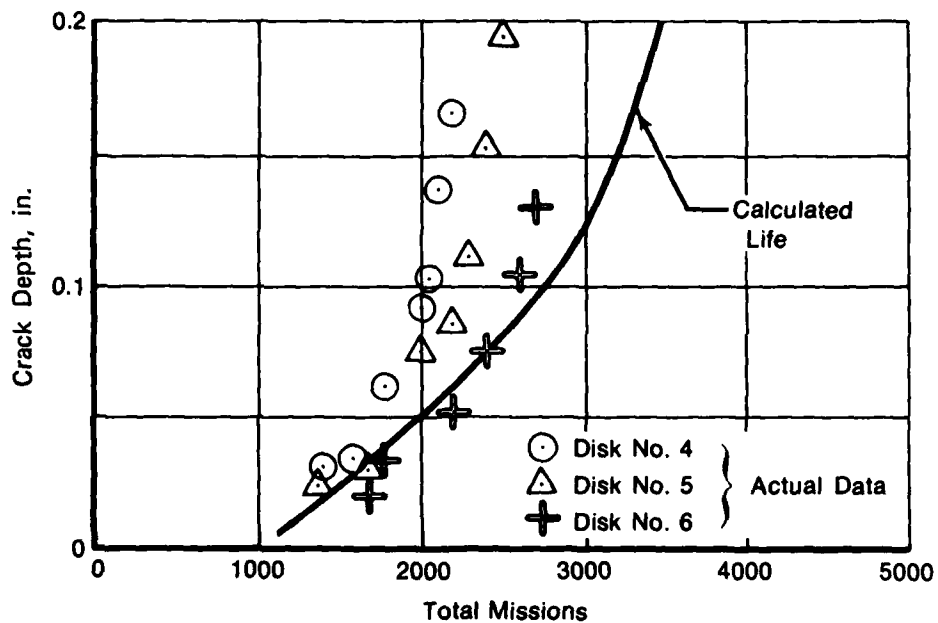
FD 175139

Figure 52. Bolthole Crack Depth vs Missions: Life Analysis of Duty Cycle, Experimental Effective K Approach Accounting for Synergistic Effects



FD 175140

Figure 53. Bolthole Crack Depth vs Missions: Life Analysis of Duty Cycle, Bowie Solution Accounting for Synergistic Effects



FD 175141

Figure 54. Bolthole Crack Depth vs Missions: Life Analysis of Duty Cycle, Deep Through-Thickness Crack Approach Accounting for Synergistic Effects

SECTION IV DISCUSSION

All disk low-cycle fatigue (LCF) lives quoted in this report have been produced from GPD MMT experimental data, and are for comparative purposes only. They are not to be construed as official P&WA design field lives.

Results of this program indicate that the capability does exist to perform Retirement-for-Cause of TF30 10th-stage compressor disks. Fracture mechanics residual life analyses and laboratory nondestructive evaluation (NDE) capabilities both display excellent accuracy and combine to produce reliable characterization of disk propagation lives. Consider Figure 55 which presents a rough estimation of average disk propagation life (as determined from simple cycle ferris wheel testing): If the NDE rejection criterion is set at a 0.010-in. deep through-crack (reliability figures of Tables 8 through 12 are for surface crack length) there would be approximately 1250 "equivalent" flight hours (EFH) of LCF life remaining in a rejected disk which contains this defect. While the laboratory NDE reliability figures presented in the previous section would indicate confident detection of any rejectable flaw, structuring of periodic Retirement-for-Cause inspections can be envisioned to allow for two consecutive inspections of a rejectable disk before it would fail (in case the rejectable defect is missed during the first inspection).

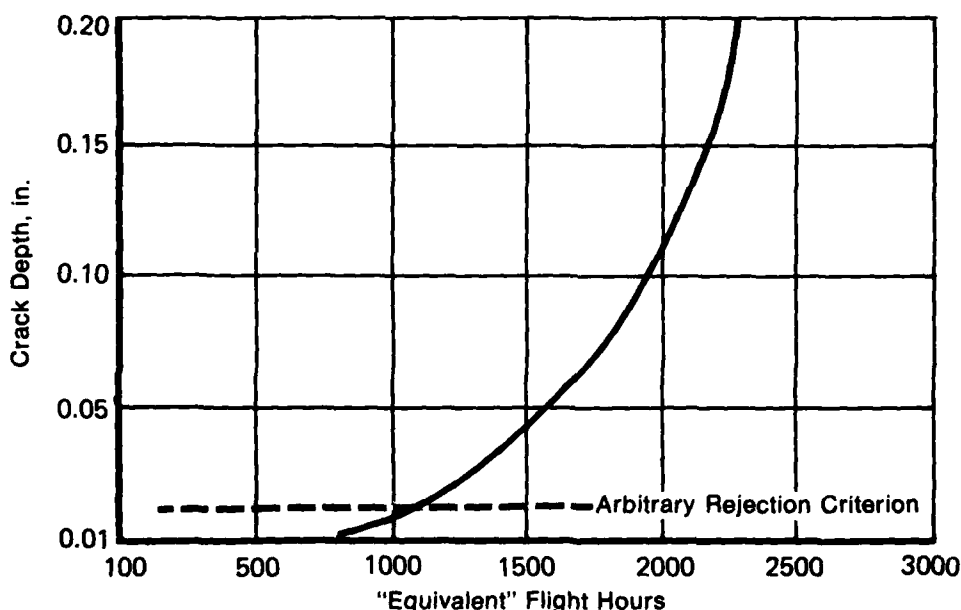


Figure 55. Estimation of Average Disk Bolthole Propagation Life, as Determined from Simple Cycle Ferris Wheel Testing

FD 175142

The relatively simplistic approach to fracture mechanics disk residual life analyses is also encouraging. Correlating a simple cycle component fatigue test with data obtained from standard crack growth specimens produced an effective K determination from which duty cycle life calculations could be made. Furthermore, a handbook stress intensity solution was shown to produce a reasonable approximation of disk propagation behavior. In other words, a complex finite element analysis of the disk bolthole would not be required to produce an accurate stress intensity solution.

The cost effectiveness and feasibility of component management associated with Retirement-for-Cause of turbine engine components has not been determined. The focus of the next phase of this contract will be on these factors and others, as applied to each disk in the F100 engine. Further assessment of the economics, etc., associated with Retirement-for-Cause of any TF30 components has not currently been scheduled for this contract.

STRAIN-CONTROLLED LCF

It is apparent from the acoustic emission (AE) rate record of Figure 21 that Incoloy 901 is a good "acoustic emitter." AE rate levels were consistently higher during strain-controlled LCF tests of Incoloy 901 than during similar tests of GATORIZED[®] IN100, the subject material of the earlier phase of this program.

Time-domain distribution analyses conducted during strain-controlled LCF testing indicated that there may be information in frequency-domain analysis of Incoloy 901 fatigue data. As shown in Figure 22, the "counts per event" distribution displayed a more radical change during the course of an LCF test than either the pulse-width or peak-amplitude distribution. Considering the latter two distributions to be held relatively unchanged, a change in the "counts per events" distribution would connote a change in frequency content of some of the recorded AE events.

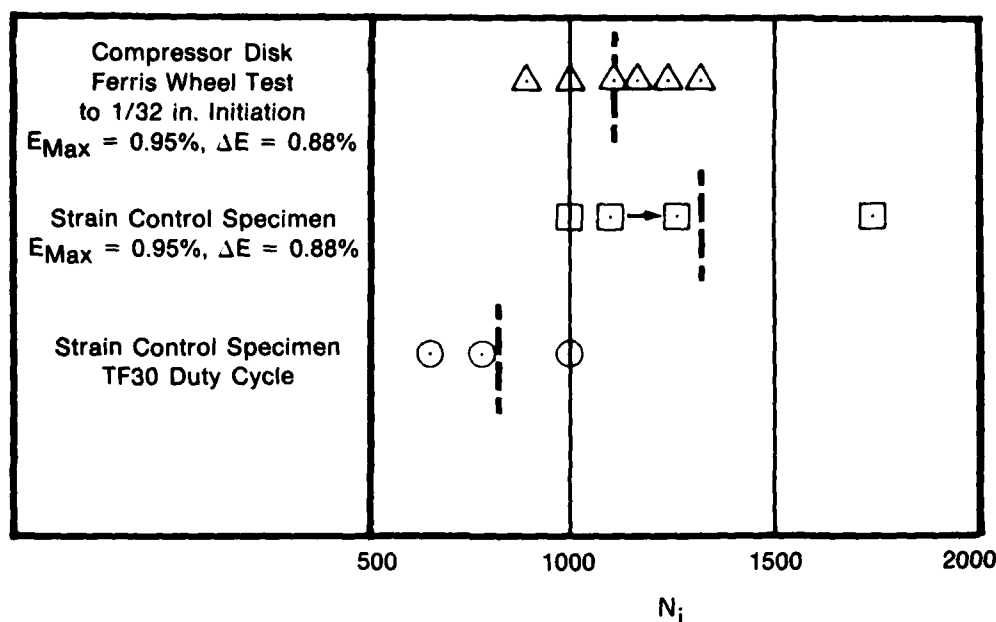
As illustrated in Figure 23, a twinning mechanism in Incoloy 901 was related to the changing time-domain distribution analyses. This fatigue mechanism was substantially different than the fatigue mechanism detected in a similar study of GATORIZED IN100, and was reflected in a different AE response. Therefore, one might envision being able to estimate fatigue mechanisms in an aerospace alloy by monitoring AE activity during a fatigue test.

Figure 56 shows a comparison of strain-controlled LCF test results vs compressor disk initiation lives (to 1/32-in. crack length). It may be concluded that strain-controlled LCF testing at comparable strain levels to disk critical locations produced comparable initiation life results. The logarithmic average of the strain-controlled LCF specimen lives was 1304 cycles (including one test which was discontinued prior to failure). The logarithmic average of the disk initiation lives was 1100 cycles. It is also apparent from Figure 56 that specimen initiation lives were degraded when comparing duty cycle life to simple cycle life.

BOLTHOLE SIMULATION LCF

Bolthole specimen lives to first crack indication were slightly longer than corresponding disk initiation lives. There are two probable reasons for this: first, the bolthole machining procedure for the specimens was not identical to the production disk procedure, resulting in varying bolthole surface conditions. Second, with all other factors held equal, there was a higher probability of one of the sixteen disk boltholes initiating before the single bolthole in each specimen. The first factor probably had a greater effect.

Figure 24 demonstrates the utility of a stress-enhanced inspection. Programs conducted at GPD have demonstrated that stress enhancement is effective for low frequency eddy-current (EC) and radiographic inspections, as well as fluorescent penetrant inspections (FPI). However, it has also been concluded that stress above 50% of operating cyclic stress produces little additional enhancement. Therefore, damage to a component need not be risked to properly stress-enhance an inspection.



FD 175143

Figure 56. Initiation Life Comparison: Compressor Disks vs Incoloy 901 Strain Controlled LCF

The microminiature probe experiment, detailed in Section III: Test Results, was encouraging from both the standpoint of transducer sensitivity and noise discrimination. Using the microminiature probe coupled intimately to the region of interest (bolthole), AE activity from a small fatigue crack (0.014 in. length) was significantly higher than from a sensor in the standard monitoring configuration, as shown in Figure 26. In fact, the standard sensor could be used as a noise reference because higher AE levels occurring at the reference sensor than at the primary (microsensor) must be extraneous noise. Microminiaturization of AE probes should open new applications for component real time AE analysis.

FRACTURE MECHANICS TESTING

Specimens tested at relatively high net section stress produced crack growth rates at higher ΔK values noticeably lower than crack growth rates for low net section stress specimens. While additional testing will be required to quantify the phenomenon, it appears that production of fracture mechanics data to model highly stressed components may require consideration of specimen net section stress.

COMPRESSOR DISK TESTING

The opportunity to "piggy-back" the Navy's M-32 component LCF life verification task for the TF30 10th-stage compressor disk allowed GPD personnel to demonstrate the fracture mechanics/NDE residual life prediction concept on a second type of engine disk for the "Disk Residual Life Studies" program, and amass a large amount of inspection data.

In fatigue crack propagation life analysis, using fracture mechanics techniques, two parameters are of prime importance: the stress intensity factor solution and the fatigue crack propagation rate for the particular structure or geometry and material at the testing conditions of interest.

Due to the complexities of the real structure, the accurate stress intensity factor solution is difficult to obtain. In most cases, the values of the stress intensity factor have to be estimated and solutions obtained from handbooks have to be modified.

In the present study, an experimental effective K solution was obtained from the actual a vs N data. It should be an accurate effective K solution. However, the solution will vary with structural configurations and will not be available until the testing is done. Analytical closed-form solutions are more desirable.

Bowie offered a solution for an infinite plate containing a circular hole. As indicated in Figure 47, results of the Bowie analysis predicted lower values of K in the vicinity of the bolt-hole and higher values at areas remote from the bolthole. This can be explained as follows:

For short cracks, the fatigue crack propagation rate was shown to be faster than would be predicted from the longer cracks (Reference 11). This, coupled with the multiple crack initiation (as seen in the present study), resulted in a much faster fatigue crack propagation rate. At a given value of da/dN , effective ΔK (and K_{max}), calculated from the fatigue crack propagation model (such as SINH), would be higher than the actual values. This was the case in the present study.

For the region away from the bolthole, it was shown at CPD that for equal-length cracks growing from each hole in a column aligned parallel to the loading axis, ΔK (and K_{max}) was lower than that obtained from $(\Delta\sigma \times K_t) (\pi a)^{1/2}$ (Reference 12).

Due to lack of agreement with the experimental data, the Bowie analysis was not considered to be a good estimation of stress intensity factor in the TF30 10th-stage compressor disk configuration.

The deep through-thickness crack approach was considered to be a good estimation of stress intensity factor at areas where stress concentration effects diminished. With the scattering nature of fatigue data in mind, however, results of this approach shown in Figure 47 were considered to be in good agreement with the experimental data within the whole range tested. Although there is no rational explanation for the "coincidence" for the time being, this approach is considered to be a good solution in the unique case of TF30 10th-stage compressor disk.

It is well documented that a crack subjected to constant load amplitude fatigue and interrupted by periodic overloading displays a decrease in fatigue crack propagation rate (Reference 13). This effect was observed in the compressor disk study. Fatigue propagation life analysis, ignoring the overload effects, resulted in conservative prediction, as indicated in Figure 51. Figure 52 shows that more accurate results were obtained when overload effect was considered.

The TF30 10th-compressor disk ferris wheel testing program provided an excellent opportunity to conduct a detailed NDT reliability study. Nondestructive inspection techniques evaluated were:

1. Stress-enhanced FPI, using Magnaflux ZL-35 post-emulsifiable penetrant
2. Laboratory FPI using ZL-35
3. Production-type FPI
4. EC, using a rotating-probe Circograph.

The compressor disk reliability study was the first large-scale NDE reliability study conducted at GPD.

It is apparent from a cursory look at Tables 8 through 12 that a large number of cracked boltholes were inspected using each technique. Replication under load was an effective documentary tool for each of the inspections.

Table 12 compares reliability of each of the periodic inspection techniques at 95% confidence. The most obvious conclusion which may be made from Table 12 is that laboratory NDE is much more effective for detection of fatigue cracks less than 0.100 in. length than standard production-type FPI. Table 12 also indicates that stress-enhanced laboratory FPI was noticeably more effective than static laboratory FPI only for the smallest flaw size range (0.003 in. to 0.016 in length). That is probably because larger flaws were not as tightly closed at the Z1 35 ultra-high sensitivity penetrant required relatively low penetration into the fatigue cracks to make them visible to laboratory technicians.

The implication of the NDE reliability results is that retirement-for-cause (RFC) NDE could be performed for many engine components using *laboratory* techniques, but standard *production-type* FPI would suffice for only a limited number of components.

The primary purpose for development of these reliability statistics was to demonstrate that obtainment of the NDE reliability levels necessary to implement RFC inspections is obtainable using the basic existing NDE tools. In other words, the generic capabilities of eddy current and specialized FPI are sufficient to produce sensitive, reliable results. However, in order to produce high-reliability inspections for small fatigue cracks in an overhaul environment, a great deal of technology development will be required (as demonstrated by results from production-type inspections).

SECTION V CONCLUSIONS

Results of this program indicate that the capability to perform Retirement-for-Cause of TF30 10th-stage compressor disk does exist. Fracture mechanics residual life analyses and laboratory NDE capability both display excellent accuracy and combine to produce reliable characterization of disk propagation lives.

The cost effectiveness and component management associated with Retirement-for-Cause of engine disks was not considered in this program, but will be studied in the next phase: "Concept Definition: Retirement-for-Cause of F100 Rotor Disks."

The primary implication of the NDE reliability figures developed during this program is that Retirement-for-Cause NDE could be performed for many engine components using laboratory techniques, but standard production-type FPI would suffice for only a limited number of components.

Fracture mechanics residual life models developed for the compressor disk from an experimental "effective" stress intensity solution, as opposed to a detailed finite element analysis, were accurate enough for a Retirement-for-Cause disk characterization, even when the K solution (developed from simple cycle testing) was applied to a TF30 duty cycle simulation disk LCF program.

Fracture mechanics testing at various stress levels revealed that application of fracture mechanics data to model highly stressed components made of Incoloy 901 may require consideration of specimen net section stress. It appears that the da/dN vs ΔK relationship is not unique over a wide stress range.

Stress-enhanced laboratory FPI was noticeably more effective than static laboratory FPI using ultra-high sensitivity PE penetrant for only the smallest size fatigue crack range evaluated (0.003 to 0.016 in. length.)

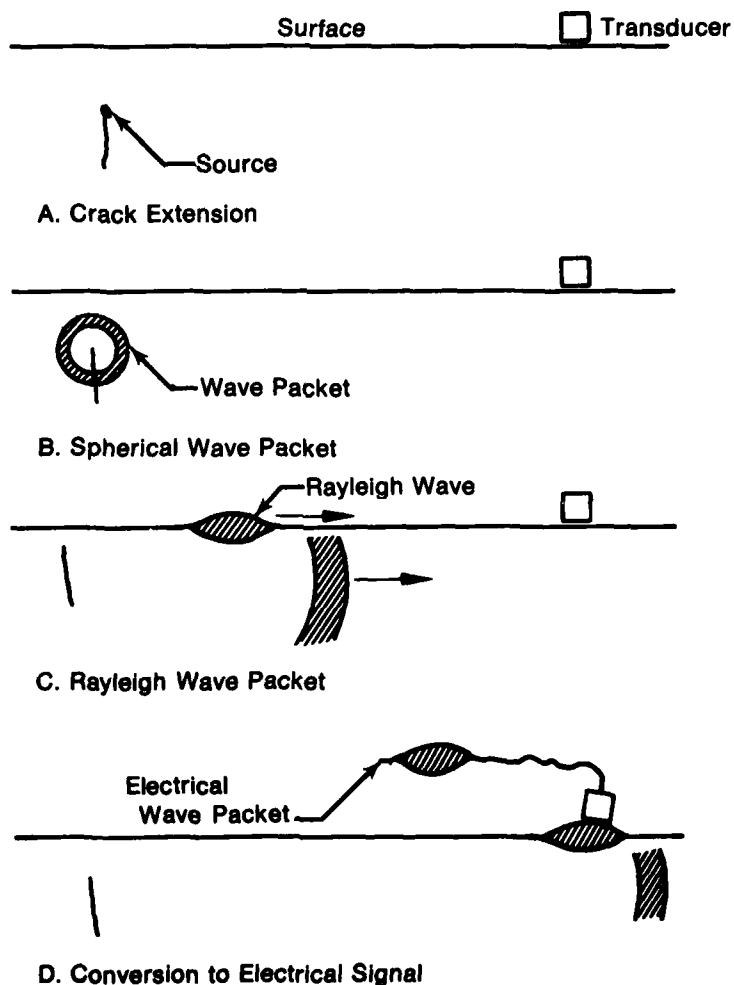
It is apparent that Incoloy 901 is a good "acoustic emitter" when subjected to LCF. Time-domain AE distribution analyses were used to detect and quantify fatigue *initiation* damage (due to microcracking and twinning) in strain-controlled LCF specimens. AE computerized source location inspection could be used as an engine disk inspection tool (to detect and locate both surface and internal defects) with minor improvements to stressing fixtures and signal analysis (including source location software).

APPENDIX A ACOUSTIC EMISSION ANALYSIS

NATURE OF AN ACOUSTIC EMISSION EVENT

Acoustic emissions (AE) are low intensity waves that can occur when a material is stressed. The mechanisms for AE range from basic dislocation motion to macroscopic crack growth (References 14 through 17.)

Figure A1 illustrates a simple AE event. Assume a material imperfection such as a crack in a deformable solid. When the material is stressed, it is possible that the crack advances a small amount. The energy input to create new crack surfaces is balanced in part by elastic energy dissipated in the form of a complex spherical wave. It is important to understand that this is a transient event. If this wave continued to propagate in an infinite body, it would lose energy at a rate proportional to R^2 , where R is the distance from the source.



FD 175144

Figure A1. A Simple Picture of an Acoustic Emission Event

In a real engineering structure, however, this complex wave packet soon confronts a boundary. When monitoring AE, a piezoelectric transducer is mounted on this boundary. Depending on the thickness of the structure, Rayleigh or Lamb surface waves are created. These surface waves are stronger than internal waves in that they decay as R^{-1} . In reality, these surface waves are generally composed of both longitudinal and shear components, and the transducer response to these components is a function of its design. The ideal transducer has good, flat response over a relatively broad frequency range.

ANALYSIS OF AE SIGNALS: TIME DOMAIN

An underlying motivation in AE research is to correlate the electric signal output of the transducer to the integrity of the component being monitored. The characterization of the AE signals therefore requires a thorough understanding of AE signal analysis techniques, stress wave transmission properties of the material and component, the transducer response, and of course the deformation and fracture processes in the material.

Cumulative Counts and Count Rate

The most common and simplest measure of AE is the threshold-crossing counts technique. Here, as the transducer resonates due to some input energy, the number of events that exceed a set threshold voltage value are counted, as shown in Figure A2. Total counts or count rates are usually obtained as a function of some secondary test parameter(s), e.g., load or time. This method is best suited for burst-type AE and is, of course, sensitive to amplitude. The "count" is only indirectly related to the damage event as experienced at the transducer.

Ringdown Counts Per Event

The number of ringdown counts per event (η) is related to the amplitude and pulse width of the signal. For burst-type emission, it has been assumed (Reference 18) that the signal is a damped sine wave of the form:

$$V_t = V_o e^{-t/\tau} \sin 2\pi ft \quad (A1)$$

where,

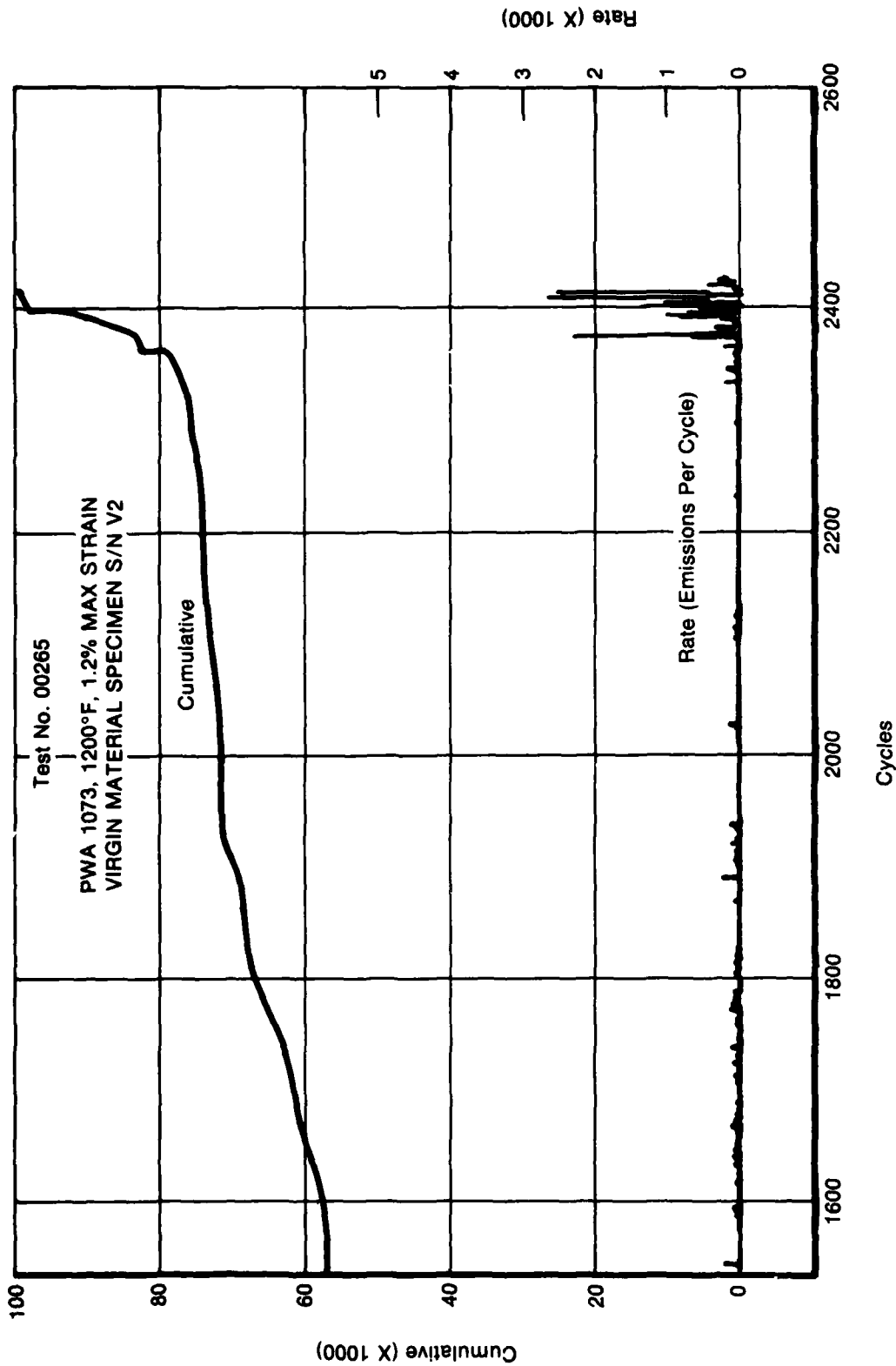
- V_t = AE signal at the transducer
- V_o = peak voltage
- f = transducer resonant frequency
- τ = damping factor
- t = time

If the ringdown time is large compared to the period of oscillation, then:

$$\begin{aligned} \eta &= f\tau \ln \frac{V_o}{V_t} \\ &= f\tau \ln \frac{CG}{V_t} \end{aligned} \quad (A2)$$

where,

- η = ringdown counts per event
- G = total gain
- C = proportionality constant



FD 175145

Figure A2. Test No. 00265: Cumulative Emissions and Emission Rate vs Cycles

The values of f and τ depend upon the geometry and acoustic transmission properties of the structure, the loading system, the resonant properties, and mounting of the transducer.

There are serious drawbacks to using counting techniques alone. Among these are sensitivity to the threshold voltage and unsuitability for monitoring continuous type emission.

RMS Voltage

For the case of continuous emission, it can be assumed that if the signal is of constant amplitude V_0 and frequency f , the signal can be represented by:

$$V_t = V_0 \sin 2\pi ft \quad (A3)$$

The rms voltage, V_{rms} , is measured as a mean value over some averaging time. It is comparable to the count rate measurement and is ideally suited for measuring continuous emission. A problem arises if the background noise is more than half the intensity of the real signal. The true signal can then be corrected by the approximate expression (Reference 19):

$$V_{rms}(\text{corrected}) = [V_{rms}^2(\text{measured}) - V_{rms}^2(\text{noise})]^{1/2} \quad (A4)$$

The energy rate, or power, of the AE signals can be approximated by the square of V_{rms} (Reference 21):

$$U = \int_0^1 V_t^2 dt = V_0^2 \int_0^1 \sin^2 2\pi ftdt \approx V_0^2 \approx V_{rms}^2 \quad (A5)$$

The integration of V_{rms} is comparable to the total count measurement.

Energy

The energy in an AE signal is proportional to the square of the voltage. Figure A3 presents a schematic of the logic in the D/E Energy Processor. One advantage to this type of signal conditioning is the ability to differentiate an event. Using the damped sine AE signal model, Reference 12 develops a relationship between the energy for the event and counts:

$$u \sim \frac{\tau V_{tn}^2}{4} \left(\frac{G_u}{G_n} \right)^2 e^{2\eta/\tau} \quad (A6)$$

where,

$$\begin{aligned} V_{tn} &= \text{counter threshold} \\ G_u, G_n &= \text{processor and counter gains, respectively} \\ \eta &= \text{counts per event} \end{aligned}$$

There are several ways to evaluate $f\tau$ for use in the above models. If η for a given event is known at two different gain settings, then $f\tau$ can be calculated. From equation A2:

$$\eta_1 - \eta_2 = f\tau \left[\ln \left(\frac{CG_1}{V_{tn}} \right) - \ln \left(\frac{CG_2}{V_{tn}} \right) \right] = f\tau \ln \left(\frac{G_1}{G_2} \right) \quad (A7)$$

However, it is not possible to determine a single value of $f\tau$ for all techniques used. Therefore, the general use of relationships such as equation A6 have limited value at this time.

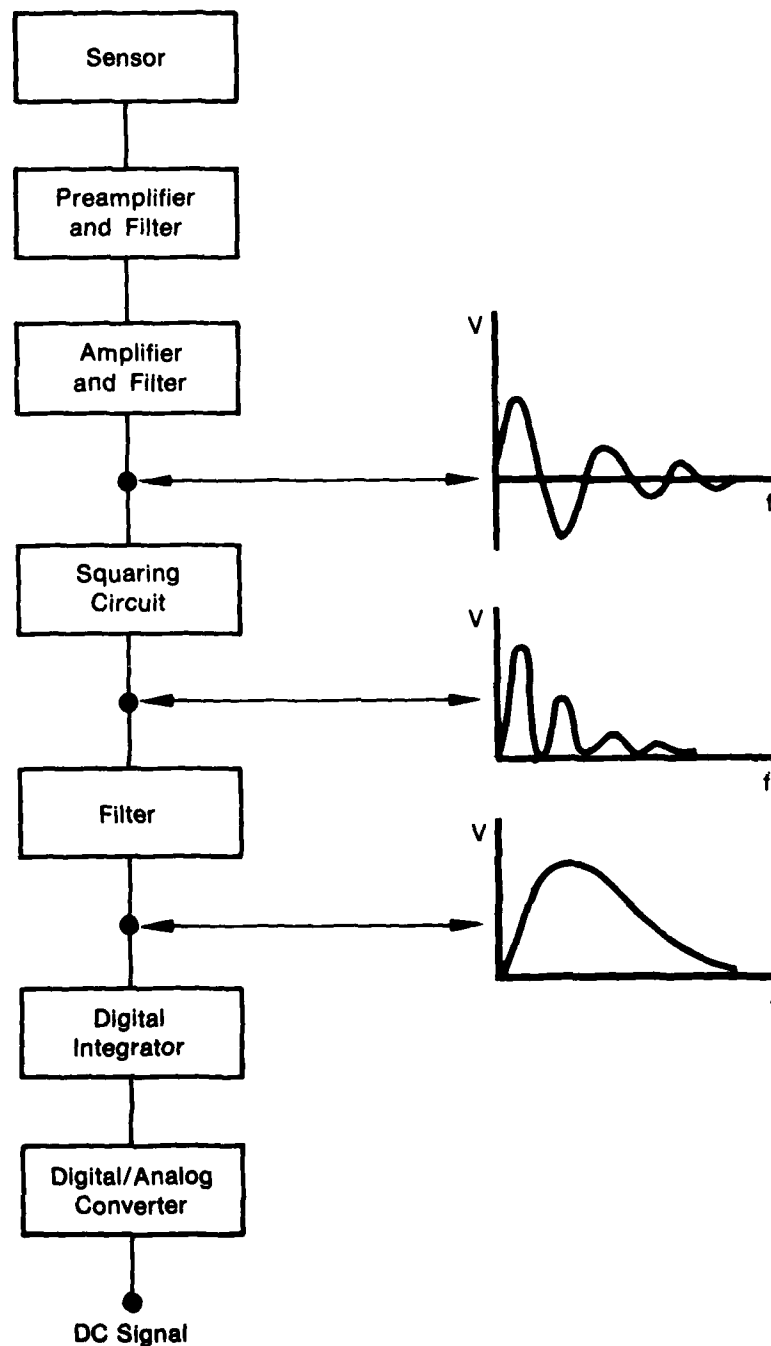


Figure A3. Schematic Representation of Components in Energy Measuring Device

FD 175148

Amplitude Distribution Analysis

The amplitude distribution analysis is an important mode of AE signal processing. The Dunegan/Endevco 920/921 Distribution Analyzer characterizes the transduced signal according to the peak amplitude of the signal. The linear AE signal is converted to a logarithmic signal, thereby creating a wide dynamic range. The log amplification characteristics of the system are given in Figure A4. The log amp output is peak-detected to derive a dc voltage proportional to the log of the peak amplitude of the signal. An analog to digital converter then outputs to the 920 Distribution Analyzer a series of 0 to 100 pulses that represents the peak amplitude in dB, with 1 dB resolution.

The peak amplitude distribution function $E(V_o)$ is the number of events with amplitudes exceeding a given voltage value V_o . It is of the form:

$$E(V_o) = kV_o^b \quad (A8)$$

The terms k and b are constants for a given increment of loading on a structure. A decrease in b indicates higher amplitude events and, therefore, impending failure. The term b might also be independent of the distance between source and transducer (Reference 20).

The logic of the Dunegan/Endevco 921 Amplitude Detector is that each pulse (count) represents the ratio of the input signal, in dB, referenced to 100 μV . The input signal and output count are related by:

$$\text{count} = 20 \log \left(\frac{V_{in}}{100 \mu V} \right) \quad (A9)$$

The conversion time in this system is 1 msec plus 20 μsec per dB.

Pulse Width

The pulse-width distribution analyzer counts the time that the envelope processor is energized, i.e., pulse width per event. The pulse width on the D/E 920 is defined as

$$PW_{AE} = (\text{Slot Number}) \times \text{Multiplier} \times 10 \mu\text{sec} \quad (A10)$$

An event is defined as follows: the processor is energized at the first pulse of a burst. It remains energized during the burst and stays energized for the envelope time period selected after the last pulse of the burst above threshold. The end of the envelope time is defined as the end of an event. The total time that the processor is energized is the burst pulse width (see Figure A5). Four envelope times are available: 50 μsec , 100 μsec , 1 msec, and 10 msec.

INSTRUMENTATION AND SIGNAL PROCESSING

The instrumentation used to monitor AE in Phase I of this contract is schematically illustrated in Figure A6.

Acoustic Emission Sensor and Preamplifier

The primary transducer being used at the Materials Engineering and Technology Laboratory is the Dunegan/Endevco Model D750, with a 750 kHz peak resonant frequency. This transducer has been found to provide optimum sensitivity to fracture events in IN100.

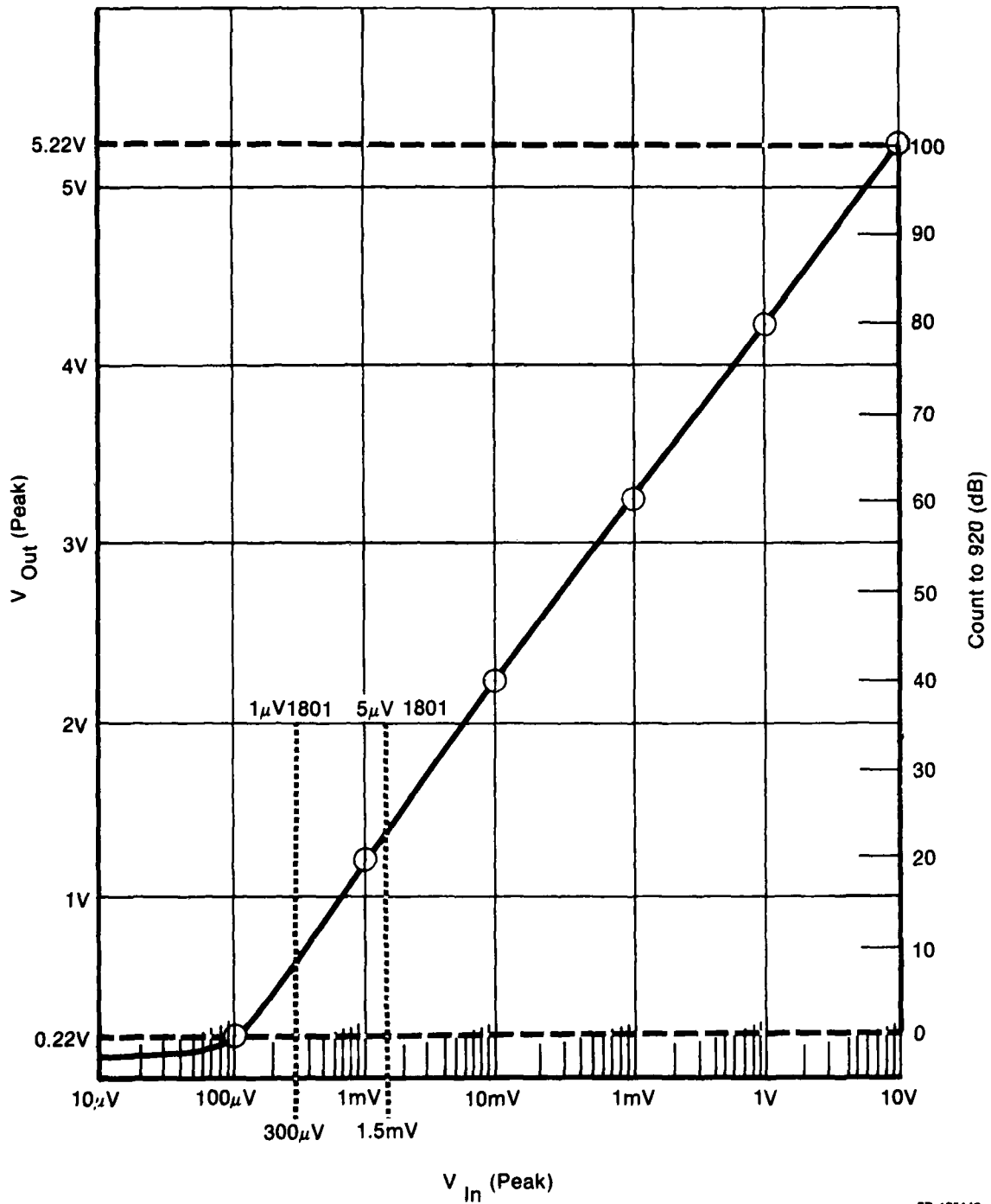
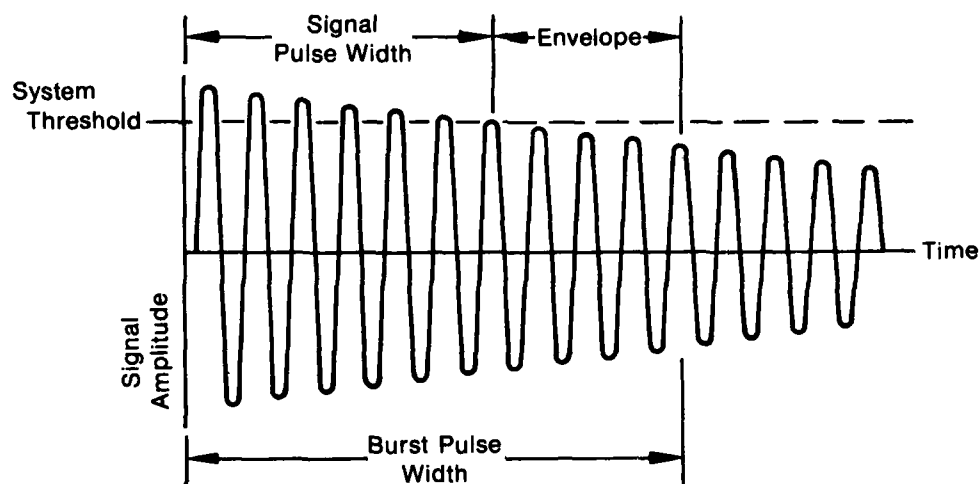


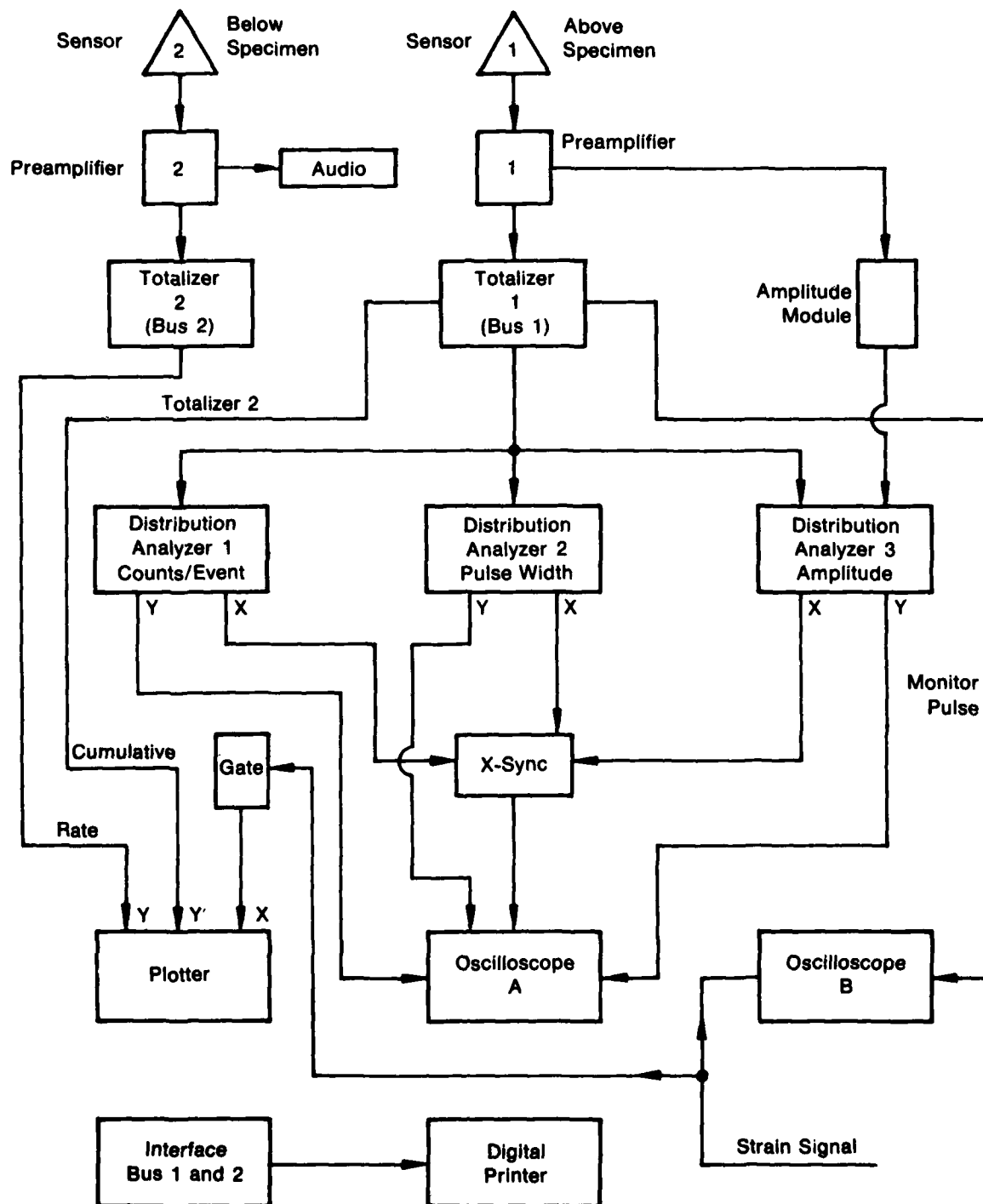
Figure A4. Log Amplification Characteristics of Dunegan/Endevco 920/921 Amplitude Distribution Analyzer

FD 175147



FD 175148

Figure A5. Burst Time Pulse Width Composed of Signal Pulse Width Plus Envelope Time (Manually Selected as 50 μ sec, 100 μ sec, 1 msec, or 10 msec)



Power Supplies 1, 2 and 3 and Interconnect Cables Not Shown

FD 175140

Figure A6. Acoustic Emission Configuration to Monitor Strain Control Tests.
Phase I: Acoustic Emission Characterization of Fatigue Damage

The D750 converts mechanical stress waves to electrical signals through a piezoelectric crystal. Frequency response is shown in Figure A7. Dunegan/Endevco's patented differential design, incorporated into the D750, helps isolate the sensor signal from electrical noise.

The sensor and a Dunegan/Endevco Model 801-P Preamplifier are connected with a short length (2 ft) of shielded cable. When used with a differential transducer, the 801-P provides 40 dB rejection of common-mode noise while supplying 40 dB gain to the processed signal. Internal noise is less than 6 μ volts.

Totalizer

An AE signal is further processed in the Totalizer (Dunegan/Endevco Model 301) through amplifications up to 60 dB and bandpass filtering.

The Totalizer digitally displays the amount of processed AE in a cumulative or rate form (when the signal is gated). A dc output is also provided to drive an x-y-y' recorder.

Distribution Analyzer Operation and Output

The FMDL has three Dunegan/Endevco Model 920 Distribution Analyzers, each capable of sorting AE events according to the number of ringdown counts, time duration, or peak amplitude of the event. The analyzers are also able to perform one-dimensional source location between two sensors by sorting the difference of arrival times of conditioned AE events.

Analyzer output is divided into 101 slots, with each of the slots 1 to 99 representing 1% of the full scale output and slot absolute values being additive from left to right as shown in Figure A8. Slots 0 and 100 are "catch-all" slots for event values which are less than 1% of full scale and greater than or equal to full scale, respectively. Slot values 0 to 100 are always presented along the x-axis of an output.

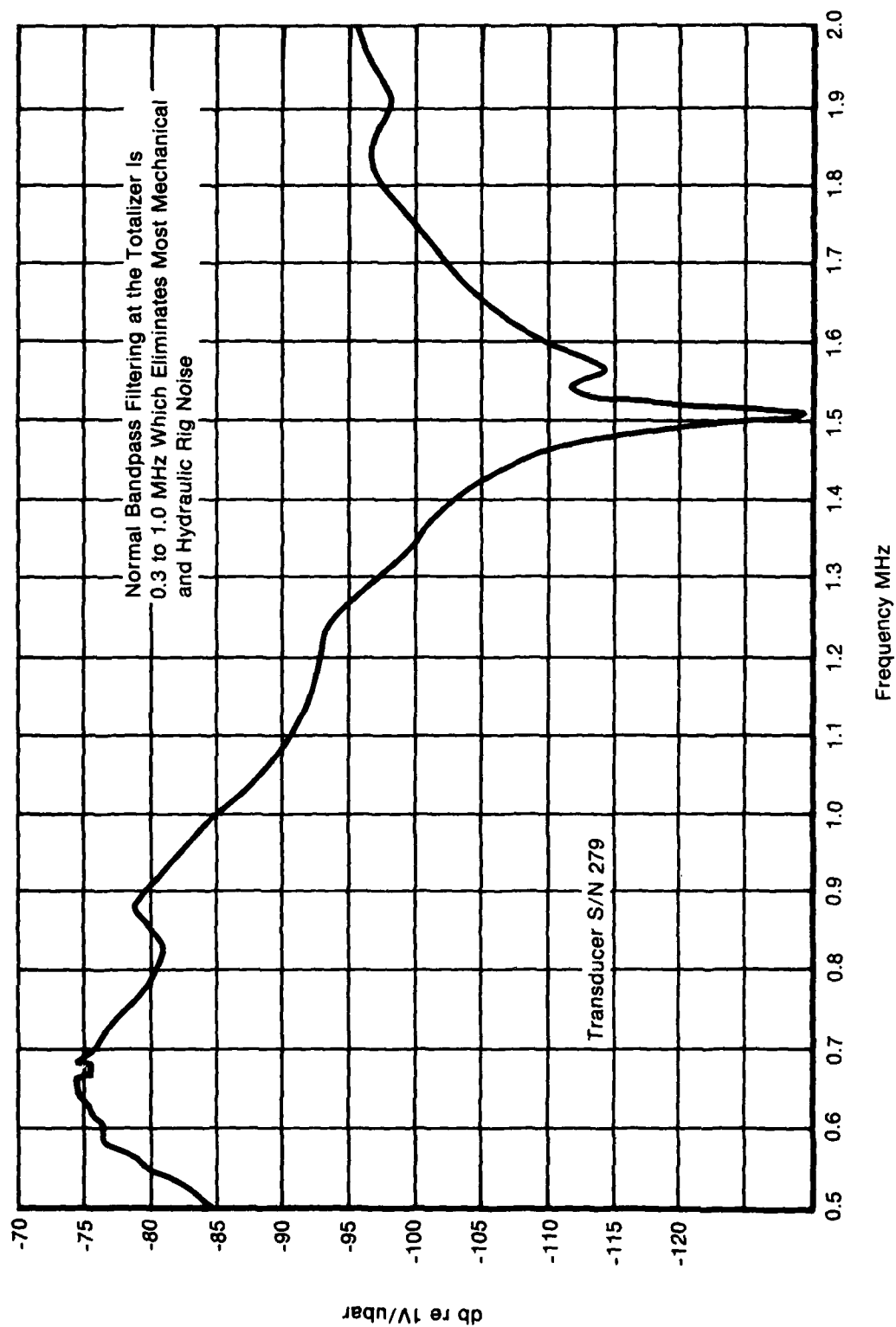
The number of events at each slot location are registered along the y-axis of the analyzer output, with a linear and logarithmic output capability. In addition, summation of events from right to left is also possible in the output.

Analyzer operation is optimized through use of a multiplier and variable signal envelope. The multiplier is capable of expanding the full X-range by three orders of magnitude. Signal envelope is the time duration after ringdown of a processed AE event before the system resets to receive another signal. Envelope times from 50 μ sec to 10 msec may be selected.

Figure A8 illustrates a typical registry for ringdown counts (top), pulse width (middle), and peak amplitude (bottom). Two events are registered in the ringdown counts number 0 slot (multiplier is 10). Therefore, the ringdown counts in each of these events were less than 10.

Pulse-width registry output incorporates emission pulse width plus envelope time to yield the total burst pulse width shown in Figure A5. Two events are registered in the burst pulse width 1.1 msec slot (multiplier is 10) in Figure A8. The envelope time was selected as one msec so the AE pulse width-to-ringdown below a predetermined amplitude threshold is between 0.1 and 0.2 msec.

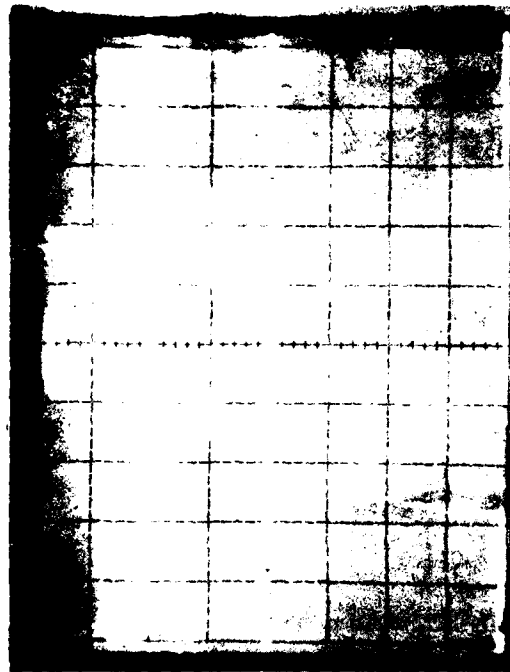
Amplitude registry covers the range 0 to 100 dB peak amplitude (multiplier not applicable). Amplitude levels in Figure A8 span 22 to 43 dB. An amplitude threshold of 22 dB was chosen for this test.



FD 175150

Figure A7. Typical Frequency Response of a Dunegan/Endevco Model D750 Transducer

Y: Number of Events at Each Slot Location



Counts Registry Is $0 \leq C < 10$ Counts/Event
(Full-Scale Is 1000 Counts/Event)

Burst Pulse Width Registry Is 1.1 msec
 \leq PW < 1.2 msec (Full-Scale Is 10 msec)

Amplitude Registry Is Between 22 dB
and 43 dB (Full-Scale Is 100 dB)

X_C : Ringdown Counts/Events
(Multiplier: x 10)

X_{PW} : Pulse Width
(Multiplier: x 10)

X_A : Peak Amplitude
(Threshold: 26 dB)

Slot 100

Slot 0

Cumulative Slot Values →

Distribution Analyzer Output May Display Ringdown Counts/Event, Pulse Width, Peak Amplitude
or One-Dimensional Source Location in the Above Manner

FD 175201

Figure A8. Distribution Analyzer Output Example

1

The Model 920 Distribution Analyzer is also capable of spatial filtering within the slot locations 0 to 100. This function is especially important when a particular amplitude range, pulse width, etc., is characteristic of a phenomenon which the test engineer wants to observe.

The analyzer output may be displayed on an oscilloscope, as in Figure A8, or on an x-y plotter. The output may also be input to a computer for further processing.

APPENDIX B

STATISTICAL TREATMENT OF INSPECTION RELIABILITY

The need for quantitative assessment of nondestructive inspection (NDI) capabilities for the detection of flaws and for improvement of these capabilities has arisen from the application of fracture mechanics principles to the design of critical components. The fracture mechanics concept of design not only recognizes that flaws can exist in a part, but also quantitatively describes the effects of any flaws that exist. When fracture mechanics is used to describe the capacity of a structure, the most critical structural member is characterized in terms of applied stress intensity factor corresponding to both the design load and the largest flaw that can be tolerated in the member. It is necessary to allow for subcritical crack growth due to fatigue loading and service environment, so that the part can achieve a specified minimum service life before the largest crack present grows to the point of fracture instability. This concept of fracture mechanics design, allowing for subcritical crack growth in service, also makes it possible to predict service life of components by detecting cracks through periodic inservice/maintenance NDI.

At the completion of inspection, it cannot be said that a particular part is entirely free of flaws simply on the basis of the inspection result; it can only be asserted that there is certain probability that the part is free of flaws having a specific type and size. The higher the inspection reliability, the higher the probability that the part is free of flaws, and the higher the overall reliability of the assembly of which the inspected part is a component. The reliability of an NDI procedure is a quantitative measure of the efficiency of that procedure in finding flaws of a specific type and size. The sensitivity of an NDI procedure is a measure of the flaw size which can be reliably detected by that procedure.

The purpose of a statistical treatment of NDI data is to develop generalizations based on sample data, and to be able to predict the outcome of future inspections. Such statistical generalizations could go beyond analysis of inspection data. Thus, extreme caution must be used in developing generalizations, and it must be carefully evaluated whether they are reasonable, justifiable, and applicable, or whether it would be wise to acquire further data.

In the routine inspection of parts, there are four possible results:

1. A flaw is indicated where there is a flaw.
2. No flaw is indicated where there is a flaw.
3. A flaw is indicated where there is no flaw.
4. No flaw is indicated where there is no flaw.

The first result is the successful detection of a flawed part, and leads to correct rejection. The second result is known as a miss, and leads to the acceptance of a nonconforming part (*false acceptance*, or a Type-I inspection error). The third result is known as a false indication or false detection, and leads to the rejection of a flaw-free part (*false rejection*, or a Type-II inspection error). The fourth result is the successful detection of a flaw-free part, and leads to correct acceptance.

For any method of NDI, the frequency of Type-I inspection errors (acceptance of flawed parts) can be reduced by lowering the specified value for the maximum acceptable response. Unfortunately, this often increases the frequency of Type-II inspection errors (rejection of sound parts). A reasonable balance between Type-I and Type-II inspection errors must be achieved for most practical inspection procedures.

PROBABILITY OF FLAW DETECTION

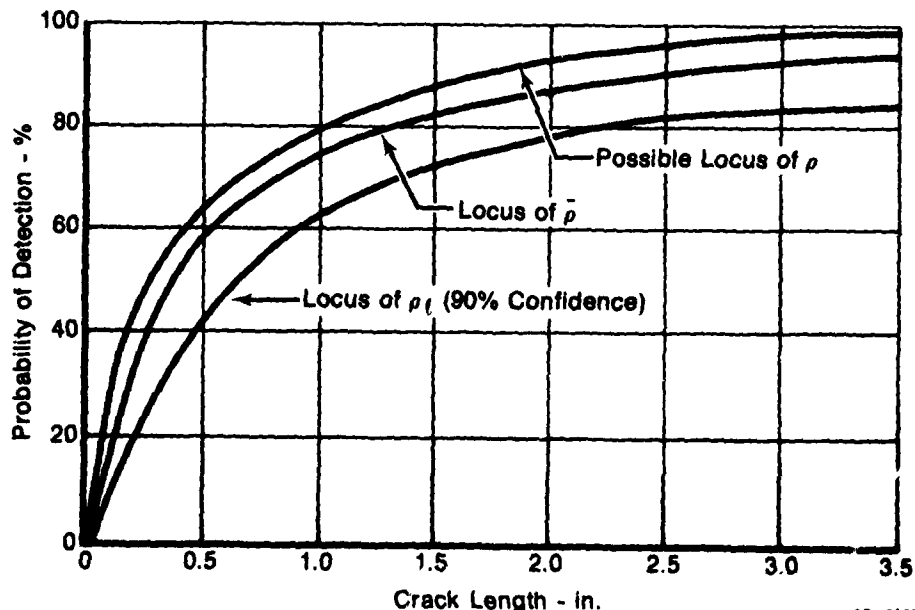
The *probability of flaw detection* is defined as the probability that, using a given inspection procedure, a trained inspector will detect a flaw if it exists. A probability of detection can be determined by experimentally observed the number of times an NDI procedure can reveal flaws in a sample of parts known to contain flaws. A probability of detection of 95% implies that for every 100 flawed parts that are inspected, at least 95 of them would be identified as containing flaws and that not more than five parts containing flaws would be identified as being free of flaws.

CONFIDENCE LEVEL

The *degree of confidence* in the probability of detection which refers to the ability to estimate from a limited sample the probability of detection representative of large-scale inspection. Thus, 95% detection probability with 90% confidence means that there is a 10% probability that 95% is an overestimate of the true (unknown) detection probability. In another sense, 95% probability with 90% confidence means that if a series of lots of parts taken from the same population were inspected, the true probability of flaw detection would be greater than 95% for nine lots out of ten.

ESTIMATES OF PROBABILITY

The *true probability of detection*, p , is an unknown quantity that cannot be determined without making an infinite number of inspections. The main objective of statistical evaluation of the reliability of NDI is to estimate p with as few trial inspections as possible. This is done by defining a lower limit (lower bound) for the range of values that is expected to contain the true probability of detection. Figure B1 presents three curves that illustrate the statistical procedure without entering into the mathematical aspects. The top curve is a possible locus for values of \bar{p} , the true probability. The middle curve represents the locus for the values of p , the point estimate of true probability. The point estimate is independent of sample size and is simply the experimentally determined ratio of the number of flaws detected to the number of existing flaws. The bottom curve is the locus of p_l , the values known to a specified lower-bound (one-sided) confidence limit.



FD 157804

Figure B1. Typical Effect of Crack Length on the Probability of Detection by Nondestructive Inspection

Each value of p_i is intended to be a conservative estimate of true probability, in that it is expected to lie on a curve that falls on or below the curve for p . The expectation that $p_i < p$ is also probabilistic, because the value of p_i depends on the confidence level, G .

THE BINOMIAL DISTRIBUTION

Because inspection of a flawed part is defined as the detection or nondetection of an existing flaw, it can best be described by the binomial distribution.

Suppose, for example, that an inspection experiment is performed wherein N specimens, all with identical flaws induced in them, are routed through an inspection system. Let S be the number of times a flawed specimen is identified during the inspection experiment. A natural estimate for the probability of detection is the ratio of the number of verifications of flaws to the number of flaws present:

$$\bar{p} = S/N \quad (B1)$$

This ratio is the sample proportion (point estimate), and is an unbiased estimate of the true probability of detection.

Because there are only two possible results of the inspection of the flawed specimens in such an experiment (either a flaw is indicated or a flaw is not indicated), S has a binomial distribution.

The number of verifications of the presence of flaws, S , has possible values of 0, 1, 2, . . . N . The probability that S equals any integer n , where $0 < n < N$, is described by the following equation, which is the standard form of a probability function for binomial distribution:

$$P(S = n) = \binom{N}{n} p^n q^{N-n}$$

where,

$$\binom{N}{n} = \frac{N!}{n! (N-n)!} \quad (B2)$$

p = true probability of detection
 q = true probability of a miss.

The probability of detecting n or more flaws can be found by summing equation 2 over all the values of S for which $S > n$. Thus,

$$P(S > N) = \sum_{i=n}^N \binom{N}{i} p^i q^{N-i} \quad (B3)$$

For a given set of values for S , N , and G , the value of p_i (or $1 - p_i$) can be found from a standard table of cumulative binomials calculated from the expression:

$$1 - G = \sum_{i=S}^N \binom{N}{i} p_i^i (1 - p_i)^{N-i} \quad (B4)$$

1

It is virtually impossible to determine the probability of detection at a given confidence level for a single flaw size, because the statistical procedures require that samples be very large to obtain a high level of confidence. Also, known flaws, whether natural or artificially induced, are very difficult to reproduce with precision. The problem then becomes one of subdividing the inspection data so that values of detection probability can be determined for smaller flaw-size intervals, and then be plotted to produce a reliability curve.

REFERENCES

1. Annis, C. G., R. M. Wallace, and D. L. Sims, "An Interpolative Model for Elevated Temperature Fatigue Crack Propagation," AFML-TR-76-176, Part I, November 1976.
2. Annis, C. G., R. M. Wallace, and D. L. Sims, "Application of Fracture Mechanics at Elevated Temperatures," AFML-TR-76-176, Part II, November 1976.
3. Sims, D. L., C. G. Annis, and R. M. Wallace, "Cumulative Damage Fracture Mechanics at Elevated Temperature," AFML-TR-76-176, Part III, November 1976.
4. *ASTM Standards*, Pt. 31, Designation E-339-70T
5. Hudak, S. J., A. Saxena, B. J. Bucci and R. C. Malcolm, "Development of Standard Methods of Testing and Analyzing Fatigue Crack Growth Rate Data," AFML-TR-78-40, May 1978.
6. Bowie, O. L., "Analysis of an Infinite Plate Containing Radial Cracks Originating at the Boundary of an Internal Circular Hole," *Journal of Math and Physics*, Vol. 35 pp. 60-71, 1956.
7. Packman, P. F., S. J. Klima, R. L. Davies, Jugal Malpani, Joseph Moyzis, William Walker, B. G. W. Yee and D. P. Johnson, "Reliability of Flaw Detection by Non-destructive Inspection", *Metals Handbook*, Vol. 11, pp. 414-424.
8. Yee, B. G. W., et al., "Assessment of NDE Reliability Data," NASA CR-134991, October 1976.
9. "Reliability of NDI on Aircraft Structures," Lockheed-Georgia/Air Force Program AFLC/SAALC/MME/76-6-38-1.
10. "Concept Definition: Retirement-for-Cause of F-100 Rotor Disks" P&WA/DARPA-AFWAL Program, June through December 1979.
11. El Haddad, M. H., K. N. Smith and T. H. Topper. "Fatigue Crack Propagation of Short Cracks" presented at the ASME/CSME Joint Pressure Vessel and Piping Conference of the American Society of Mechanical Engineers, Montreal, Canada, June 25-30, 1978.
12. Burck, L. H. and C. A. Rau, Jr., "Fatigue Crack Propagation from Small Holes in Linear Arrays," *Int. Journal of Fracture*. Vol. 9, No. 1 March, 1973.
13. Larsen, J. M. and C. G. Annis, Jr., "Observation of Crack Retardation Resulting from Load Sequencing Characteristic of Military Gas Turbine Operation", presented at ASTM Symposium on Effect of Load Spectrum, San Francisco, CA, 21 May 1979.
14. Tetelman, A. S., "Acoustic Emission and Fracture Mechanics Testing of Metals and Composites," Contract DAH-04-68-C-0008, TR No. 7, July 1972.
15. Bell, R. L., "Acoustic Emission Transducer Calibration — Transient Pulse Method," Dunegan/Endevco Corp. TR DE-73-3.
16. Ono, K., "Acoustic Emission and Microscopic Deformation and Fracture Processes," Contract N00014-69-A-0200-4031, UCLA-ENG-7465, September 1974.

REFERENCES (Continued)

17. Wallace, R., "Acoustic Emission Technology Status Report — 1972," Pratt & Whitney Aircraft FMDL 17432, 29 January 1973.
18. Harris, D. O., and R. L. Bell, "The Measurement and Significance of Energy in Acoustic Emission Testing," Dunegan/Endevco Corporation, TR DE-74-3A, September 1974.
19. Copper, G. R., and C. D. McGillen, "Methods of Signal and System Analysis," Holt, New York, 1967, pp. 131, 362.
20. Harris, D. O., "Analytical Techniques Relating Acoustic Emission to Fracture," *Science Applications Incorporated*, SAI/SR-119-PA.

111111